Van Oord
Marine ingenuity

CoMEM

Numerical modelling of wave agitation in ports and access channels

A comparison study between SWASH and MIKE 21bw

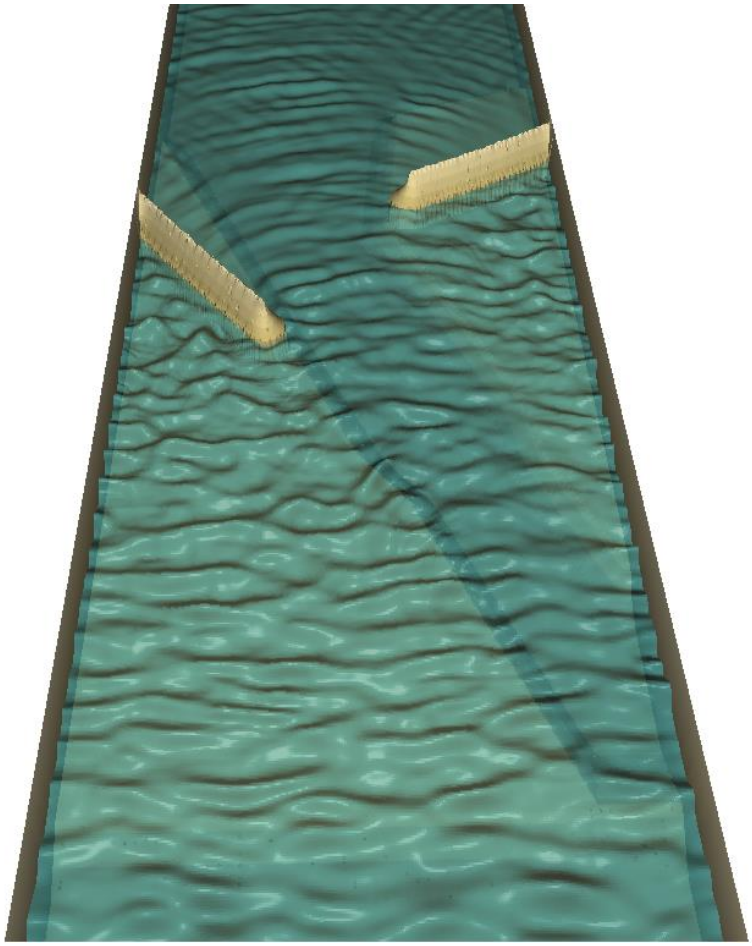

MSc Thesis

Dennis Monteban

June 2016

TU Delft Delft University of Technology

NTNU Norwegian University of Science and Technology

University of Southampton

Figure cover page: screenshot of the surface elevation of the approach channel (Case 1), computed by MIKE 21bw. The screenshot is taken at the end of the simulation.

Numerical modelling of wave agitation in ports and access channels

A comparison study between SWASH and MIKE 21bw

By
Dennis Monteban

Master of Science thesis
Delft, June 2016

Graduation Committee:

Prof.dr.ir. A.J.H.M. Reniers	Delft University of Technology
Dr.ir. M. Zijlema	Delft University of Technology
Ir. B. Wijdeven	Delft University of Technology
Dr.ir. G.P. van Vledder	Van Vledder Consulting
Ir. A. Lioutas	Van Oord Dredging and Marine Contractors
Ir. A. Haghgoo	Van Oord Dredging and Marine Contractors
Ir. D.W. Dusseljee	Witteveen+Bos

Preface

This master thesis is part of the Master of Science program Coastal and Marine Engineering and Management (CoMEM), specialisation coastal engineering. This specialisation within the CoMEM program is an integrated master program between the Norwegian University of Science and Technology, the Technical University of Delft and the University of Southampton. The thesis work was carried out at TU Delft in cooperation with Van Oord Dredging and Marine Contractors. Furthermore, this master project was performed from February 2016 till June 2016.

Firstly, I would like to acknowledge all the members of my graduation committee, which include: prof.dr.ir. Ad Reniers, dr.ir. Marcel Zijlema, ir. Bas Wijdeven, dr.ir. Gerbrant van Vledder, Ir. Anestis Lioutas, ir. Amir Haghgoo and ir. Daniel Dusseljee.

I owe a special thanks to dr.ir. Gerbrant van Vledder for his constructive criticism and feedback on my report. Also a special thanks to dr.ir. Marcel Zijlema for his help regarding SWASH.

Furthermore, I am grateful to ir. Anestis Lioutas and ir. Amir Haghgoo from Van Oord for their suggestions for the setup of the MIKE 21bw simulations. Moreover, they arranged a trip to DHI in Denmark which greatly contributed to my progress.

Finally, I would like to thank my family and friends for their unconditional support. Without them this project would not have been possible.

Dennis Monteban

Delft, June 2016

Abstract

The determination of wave penetration in ports is of great importance for the design of coastal structures and for the efficiency of port operations. Nowadays, coastal engineers can make use of numerical models for the assessment of wave climates in ports. Various numerical models exist, including the phase resolving models SWASH (TU Delft) and MIKE 21bw (DHI).

Van Oord Dredging and Marine Contractors are currently using the numerical model MIKE 21bw. To get a bit more familiar with SWASH and to see how the two numerical models relate to one another, they initiated this master project together with TU Delft. Therefore, the main aim of this thesis is to compare the numerical models SWASH and MIKE 21bw in terms of their accuracy, computational requirements and numerical stability for waves encountering approach channels and waves propagating into ports.

A theoretical analysis between the two numerical models is presented first which shows that they are fundamentally different, i.e. based on different equations and assumptions. The main difference is that SWASH uses the non-hydrostatic non-linear shallow water equations, including the vertical coordinate, while MIKE 21bw uses the (enhanced) Boussinesq equations which exclude the vertical coordinate. Another difference is that SWASH may use multiple vertical layers, improving its dispersion characteristics. Therefore, the application range of SWASH is larger in terms of the maximum water depth to deep water wave length. Furthermore, SWASH can include more physical phenomena and does not require a minimum water depth as MIKE 21bw does.

Beside the theoretical analysis, a comparison study was performed making use of a physical experiment of an approach channel (Case 1) and of a harbour basin (Case 2).

From the comparison of the measurements with the numerical simulation of the approach channel (Case 1), it was found that both numerical models are capable of resolving wave-channel interaction for long waves ($f < 0.13$ Hz) and the accuracy in both models is comparable, although the significant wave height based on the total wave spectra is under-estimated in both numerical models. Numerical damping cannot (fully) explain the under-prediction of the significant wave height. Further, it is believed that inaccuracies/uncertainties in the physical experiment regarding the measurements and the setup were quite severe. This may explain the observed differences between the numerical models and physical model results.

A comparison of the numerical simulations of the harbour (Case 2) with the physical experiment shows that both numerical models can accurately model wave penetration of primary waves into ports when simulating on prototype scale. However, the simulations performed on physical model scale (same scale as the physical experiments) resulted in critical numerical instabilities in both numerical models, especially in MIKE 21bw. The accuracy in predicting the significant wave height and energy period is comparable for both numerical models. Furthermore, SWASH turned out to be numerically more stable while the computational requirements are less in MIKE 21bw when two vertical layers are used in SWASH.

Finally, a general guideline is presented for the selection of SWASH or MIKE 21bw for wave modelling purposes.

Table of Contents

1 Introduction

Wave agitation in ports influences the manoeuvring and mooring of vessels. It determines to a great extend how efficient the loading and unloading of ships can be. Too high wave conditions will have a negative effect on the workability and causes unacceptable vessel movements which may lead to the breaking of mooring lines, piles, fenders and damage of vessels. Therefore, wave penetration into harbour basins is an essential parameter in the design of ports.

The amount of wave energy entering the harbour depends amongst others on the layout of the basin, the structures present (breakwaters, berths, piles etc.) and the approach channel. Waves generated offshore and propagating towards the port will encounter the approach channel. The sudden depth change which the waves experience can significantly alter the amount of wave energy penetrating the harbour and may change the design wave conditions for adjacent coastal defence structures and coastal morphology.

Waves in the harbour basin do not only originate offshore due to wind, but can also be generated locally by ship movements and wind. These locally generated waves are usually less severe than waves generated offshore and penetrating the harbour. In particular, low frequency waves (long waves) are known to cause most hindrance in ports due to harbour oscillations and possible resonance.

1.1 Problem description

To minimize the motion of ships (heave, sway and surge) for downtime at berths and quay operations, it is vital to predict wave climates in ports and properly design accordingly. These predictions can be made by physical or numerical models. Physical models have the advantage of including almost all physical processes and do not use simplifying assumptions as numerical models do. However, physical experiments are rather costly if multiple layouts need to be investigated. For that reason, engineers make use of numerical models. The main advantage of numerical models is that multiple layouts and conditions can be investigated relatively cheap compared to physical models. Though, numerical models use assumptions and approximations because it is not feasible (yet) to model all relevant physical processes due to computational demand. As a result of the simplifications, numerical models need to be validated in order to see if they perform as expected and if they are a reliable numerical tool.

Many different numerical models which are based on different equations and assumptions have been proposed. Each of these models has its own strengths and weaknesses and are appropriate for different applications, i.e. have different boundaries of applicability. It is not always known a priori which numerical model can be used best in a specific situation and how they relate to one another. Which model to choose depends on the computational efficiency. An important criterion for determining the computational efficiency is the accuracy in predicting for example wave heights, wave periods, low frequency energy, long period oscillations and how well they compute waves encountering an approach channel under certain angles. Moreover, the stability and computational requirements have to be considered in order to determine the computational efficiency.

1.2 Motivation of study

This thesis is done in corporation with van Oord Dredging and Marine Contractors which is a world leading contractor operating in more than fifty countries worldwide and is specialised in dredging, offshore wind and offshore oil and gas. For more information about the company, see www.vanoord.com.

Van Oord is currently using the numerical model MIKE 21bw and expressed their interest in the numerical model SWASH (see Chapter 3 for more information about the models). To get more familiar with SWASH and to see how both models relate to one another, they initiated this project in cooperation with TU Delft.

1.3 Objective and research questions

The two numerical phase-resolving models SWASH and MIKE 21bw are the focus of this project. The main aim of this thesis is to compare the numerical models in terms of their computational efficiency for waves encountering an approach channel and waves propagating into harbours. The computational efficiency is determined by making use of two physical experiments. The computational efficiency includes accuracy, computational requirements and numerical stability or robustness of the numerical models. Moreover, the aim is to explain and minimize possible differences in the numerical model results.

The research questions are as follows:

Main question

What is the computational efficiency, given certain accuracy limits, of the phase-resolving models MIKE 21bw and SWASH in modelling the phenomena involved in waves penetrating ports and encountering approach channels and what are their boundaries of applicability?

Sub questions

- What are the theoretical differences between Mike 21bw and SWASH?
- What is the computational efficiency of SWASH and MIKE 21bw and what are their boundaries of applicability based on the simulation results of two physical experiments?
- What causes the differences between the numerical and physical model results and how can they be minimized?

1.4 Approach

The approach followed in order to answer the research questions is summarized in Figure 1.1. It consists of three main steps which are all described in more detail in the following paragraphs.

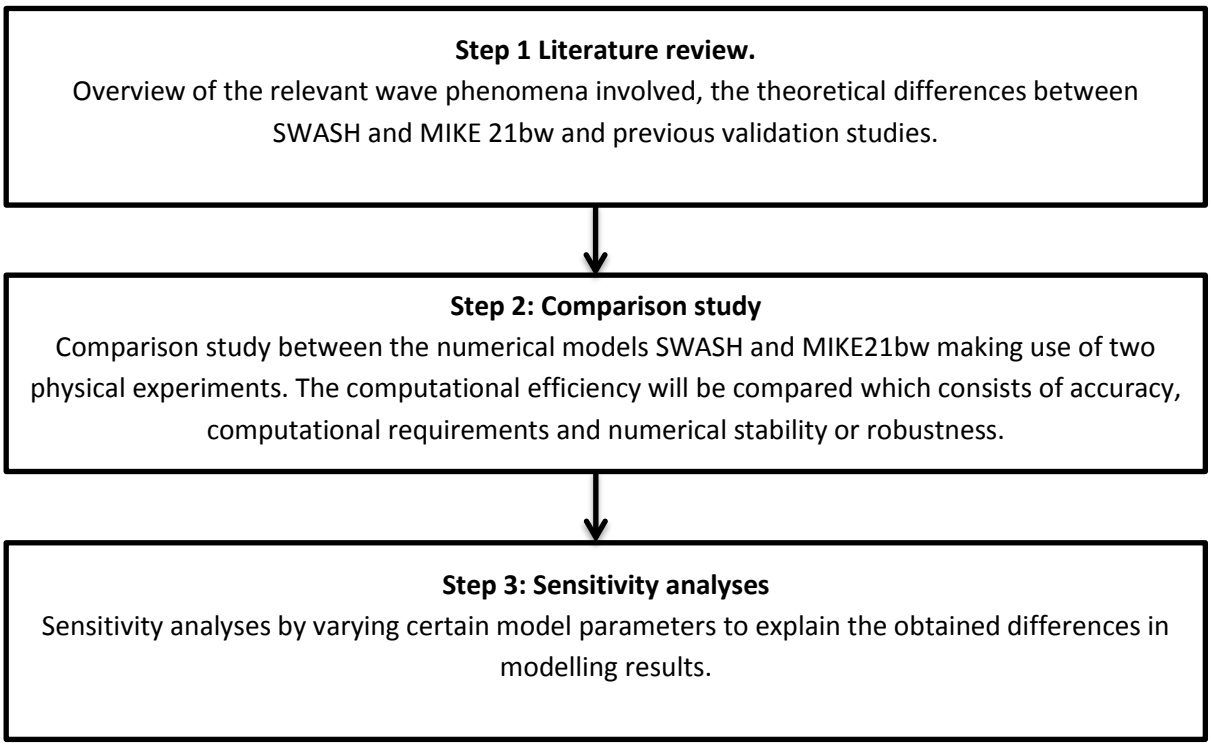

Figure 1.1. Flow chart of the main steps followed in this thesis.

Step 1: literature review
The first step of this thesis consists of a literature review. The relevant wave phenomena involved in the dredged entrance channel and in waves penetrating ports, e.g. diffraction, refraction, shoaling, reflection, transmission, long period oscillations, dispersion, wave breaking and wave-wave interactions are studied and presented in Chapter 2. Furthermore, the relevant numerical model classes are presented in this chapter.

In Chapter 3, the two numerical models (SWASH and MIKE 21bw) are compared based on their underlying equations, assumptions, limitations, boundary schematisations and what kind of numerical schemes they use. Further, previous validation studies regarding SWASH and MIKE 21bw are presented.

The aim of this first step is to give a clear overview of the relevant wave processes and theoretical differences between the two numerical models and consequently answer the first research question; what are the theoretical differences between Mike 21bw and SWASH?

Step 2: comparison study
The second step is a comparison study between the two numerical models in order to determine their computational efficiency. In Chapter 4 the methodology followed is described together with the used boundaries of applicability for this thesis. The results of the comparison are expressed as a relative bias/error at each wave gauge and as a mean averaged percentage error over all the wave gauges, both errors are defined in Section 4.1. Moreover, in this section the required accuracy limits considered for this thesis are explained.

Furthermore, the comparison study makes use of two physical experiments which were available for this thesis and are introduced in Chapter 5. The first physical experiment is for an approach channel and the second experiment is for a harbour basin.

These physical experiments were simulated in both SWASH and MIKE 21bw and the computational efficiency is determined which includes accuracy, computational requirements and stability.

In Chapter 6, the comparison based on the physical experiment of the approach channel is presented. In order to see how accurate the numerical models are in terms of boundary schematisations, type of grid, local refinements etc., multiple wave parameters are compared with the measurements. For this case, the considered wave parameters are the significant wave height and energy period based on the total frequency spectra and a cut-off frequency spectra ($f < 0.13$ Hz).

The comparison based on the physical experiment of the harbour case is presented in Chapter 7. The compared wave parameters are the significant wave height and energy period based on the low frequency energy and primary wave energy. In addition, two different long period oscillations are computed and compared.

Beside the accuracy, more practical issues which determine the computational efficiency are the computational requirements and numerical stability. The computational requirements include parallelisation aspects and computation time. The numerical stability gives insight into questions as: which numerical model is more robust, easier to use and needs less numerical 'tricks' in order to be stable. The goal of the second step is to gain insight in the performance of the two numerical models and hence, answer the second research question; what is the computational efficiency of SWASH and MIKE 21bw and what are their boundaries of applicability based on the simulation results of the physical experiments?

Step 3: sensitivity analyses
This is the final step of the thesis and focuses on the differences in results obtained by both numerical models compared with the physical experiments. Sensitivity analyses are performed by varying certain model parameters to see whether the differences in results can be explained.

The aim of this last step is to find explanations for the obtained differences and consequently answer the third research question; what causes the differences between the numerical and physical model results and how can they be minimized?

2 Wave processes in ports and access channels

The behaviour of waves in shallow regions and complex harbour layouts is driven by a numerous variety of physical processes. Sections 2.1 and 2.2 give a brief description of several wave phenomena involved in the shallow area, the dredged entrance channel and the port, e.g. shoaling, refraction, diffraction, wave transmission/reflection, dispersion, low frequency waves, harbour oscillations, non-linear wave-wave interactions and wave breaking. In addition, scaling laws are shortly introduced. For more information on the physical processes see Bosboom and Stive (2015), Holthuisen (2007) and Mei et al. (2006). Furthermore, in Section 2.3, two numerical model classes are introduced which are relevant for this thesis.

2.1 Relevant wave processes

Refraction

Refraction is the phenomenon of waves turning towards shallower water due to predominantly depth-induced changes but also because of current-induced changes. This can be explained as follows: when waves approach the shore under an angle, there is a depth variation along the wave crest which corresponds to a phase speed difference in lateral direction (along the wave crest). Waves in deeper water travel faster than in shallow water, so waves in deeper water travel further than waves in shallow water for a given time interval. From this it can be understood that waves turn towards shallower water.

Refraction occurs at different spatial scales, i.e. large and small scale refraction. The small scale refraction is important for harbours with a varying depth in the harbour basin. Moreover, small scale bathymetry changes and thus small scale refraction, may lead to energy focussing on a particular part of a coastal defence structures such as a breakwater.

Shoaling

Shoaling is also caused by depth changes, but in contrast to refraction, shoaling is the change of waves due to depth variations in the direction of propagation and not due to depth variations in lateral direction. The shoaling effect causes initially a reduction in wave amplitude, but then due to energy compaction (energy bunching) the wave amplitude increases. Because of the increase in wave amplitude, linear wave theory becomes less applicable and non-linear effects become more important.

Diffraction

The phenomenon diffraction is the bending of waves around a sharp corner such as a headland or breakwater with associated shadow zones. Due to sharp corners, an abrupt change in wave amplitude occurs along the wave crest. The wave will turn towards the region with lower wave amplitudes, allowing waves to enter the shadow zone. The result is a change in wave direction and wave height.

The diffraction effect is stronger for long waves than for short waves. Consequently, the decrease in wave height is greater for short waves (high frequency waves) than for long waves (low frequency waves). This leads to a shift of the diffracted energy density spectrum towards the lower frequencies due to the filtering of high frequency waves. Therefore, the mean wave period in the shadow zone behind for instance a breakwater is lower than the mean period of the incoming waves.

Reflection and transmission

When waves hit a permeable structure, part of their energy will be absorbed, reflected and possible transmitted passed the structure. The amount of wave energy that is transmitted, reflected or absorbed depends on the incoming wave characteristics, the geometry and permeability of the structure.

Transmission of wave energy can be through or over a structure. This is an important phenomenon during extreme storm conditions where breakwaters are being overtopped. The transmitted wave height is less than the wave height of the incident waves. Moreover, the mean wave period usually changes compared to the incident wave period.

The amount of reflected wave energy lies between two extremes; waves may be 100% reflected or 100% dissipated. A vertical cliff or wall reflects almost all the incoming wave energy while a gentle beach barely reflects any energy. The amount of energy reflected in reality will lie between the two limits and depends mainly on the wave characteristics such as the wave height, wave length, the angle of approach and on the structure geometry, permeability and roughness.

Vertical quays in ports generally reflect much of the incoming wave energy which leads to standing waves. These standing waves can become close to twice the height of the incoming waves if almost all wave energy is reflected. This can cause severe damages to ships lying at their berth. Therefore, it is important to dissipate as much wave energy in a harbour to maximize port operations.

Thompsen et al. (1996) provides a table with different reflection coefficients for different type of structures. Moreover, the coefficients are given as a range of values. For example, for a vertical wall they give a reflection coefficient of 0.7-1, indicating that the uncertainty is quite large.

Low frequency waves are reflected more from a vertical wall or slope compared to high frequency waves. Therefore, for a given geometry and (fixed) porosity, the reflection coefficient is larger for long waves compared to short waves. This is illustrated in Figure 2.1.

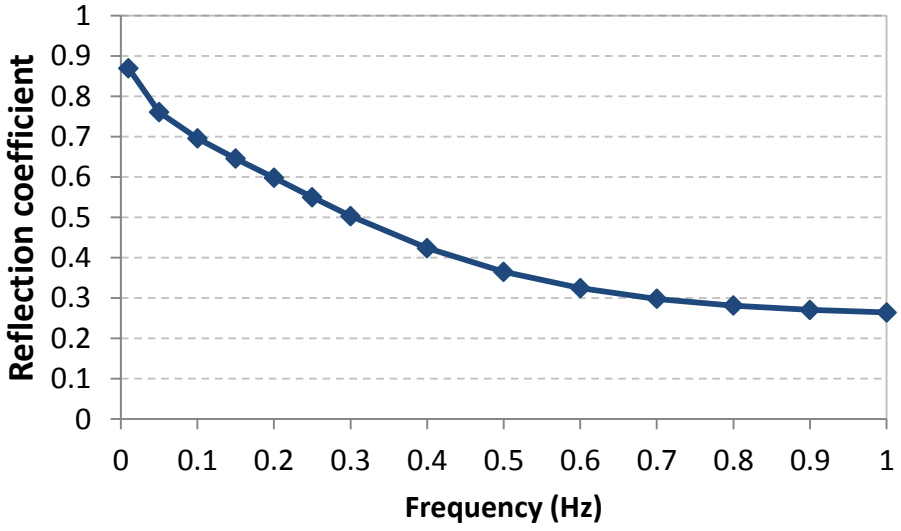

Figure 2.1. Graph showing the relation between frequency and reflection coefficient given a geometry and (fixed) porosity. This graph is computed with the MIKE 21bw toolbox to calculate reflection coefficients and based on a porosity value of 0.6, a wave height of 0.106 m and a width of the porosity layer of 2.03 m.

Dispersion

From linear wave theory it follows that the wave celerity of waves travelling in deep water is dependent on their wave period and thus on their frequency. These waves are referred to as dispersive waves. Consequently, wave groups, which consist of individual waves with different frequencies, travel with a group celerity which is different than the individual phase celerity. On the other hand, if waves travel in shallow water, then their phase celerity does not depend on the wave period (frequency) and they are referred to as non-dispersive waves. The group celerity is then equal to the individual phase celerity.

Frequency dispersion is a linear effect which indicates that waves are being dependent on their frequency in deep water. It causes low-frequency wave energy to travel faster than the energy of high-frequency waves. This results in a so called filtering effect. Waves generated offshore during a storm are highly random and consist of a large range of frequencies. The lower frequency waves travel faster and reach for instance a harbour earlier than the high frequency waves.

This filtering effect is further enhanced by directional dispersion. Because waves are spread over many different directions, only part of the wave energy will propagate towards the area of interest. Therefore, waves generated offshore become more and more long-crested than short-crested with increasing distance from the storm.

A nonlinear effect which waves experience when the water depth is relatively small compared to the wave length and wave amplitude is amplitude dispersion. It causes large amplitude waves to travel faster than low amplitude waves. This is because the wave celerity is dependent on the water depth, which can be significantly larger for large amplitude waves when the water depth is small compared to the wave amplitude. Moreover, it can also occur for steep waves.

Low frequency waves

Waves generated offshore have a wide spread of frequencies and directions. These wind generated short waves generally travel in groups. The groups travel with a speed which is (in deep water) different from the phase speed of individual waves. Because these groups consist of waves with different wave heights, their corresponding radiation stresses vary, resulting in a set-down in the shoaling zone which varies with time. Due to this set down, a long wave motion exists, commonly called a bound long wave. These bound long waves travel with the speed of the group and have the same length and are therefore forced.

The low frequency waves (bound long waves) are of major importance for the design of a harbour layout. Resonance may occur when the frequency of the wave corresponds with the eigenfrequency of the harbour, see also the next paragraph.

Seiches and harbour oscillations

Seiches may occur in enclosed basins and can be explained as a water body swaying back and forth. Enclosed basins possess resonant eigenmodes which are determined by their geometry and depth. When the eigenmodes of the external forcing (e.g. wind, atmospheric pressures etc.) are similar to the resonant modes of the basin, standing oscillations occur.

Harbour oscillations are a specific type of seiches, with the main differences rising from the fact that a harbour is not fully closed, but partially. Therefore, energy loss in a harbour is mainly due to

energy radiating out of the mouth, while for an enclosed basin dissipation of energy is dominant. Furthermore, harbour oscillations are predominantly generated by low frequency waves entering through the mouth, on the contrary to enclosed basins.

Another main difference is that harbour oscillations have a specific fundamental mode which is not present in enclosed basins, the so called Helmholtz mode (Rabinovich, 2009). This is the most important mode with the lowest frequency. For an idealized open-ended rectangular basin it has a node at the basin entrance and an anti-node at the closed side of the basin. Moreover, the wave length is roughly four times the length of the harbour. Higher resonant eigenmodes are present as well and correspond to frequency waves which are higher than the frequency corresponding to the Helmholtz mode.

The main problem with harbour oscillations is that a relative small amplitude long wave is able to cause a large vertical variation in water level inside the harbour basin. The large variations in water level inside the basin are accompanied by strong horizontal currents which can hinder port operations.

Wave breaking

Most dissipation of wave energy approaching the shore is due to depth induced wave breaking. Waves grow in amplitude while propagating towards the shore due to (amongst others) shoaling. When the height of the waves becomes too large compared to the water depth, breaking occurs. In general, three different types of depth induced wave breaking were observed: spilling, plunging and surging breakers. For the design of coastal structures, it is of vital importance to know which breaker type occurs in front of a structure because the wave induced loadings differ per breaker type. Moreover, the plunging breaker corresponds to the highest loads and should be avoided as much as possible.

Waves do not only break close to the shore because of the limited water depth, but also break offshore due to a wave steepness which is too large. This deep water breaking, also called white-capping, is a complex nonlinear phenomenon which causes most of the wave energy dissipation offshore.

Wave-wave interactions

In harbour basins, refraction, diffraction and reflection cause diamond wave patterns to be a common observed phenomenon. When these diamond patterns interact with a third freely propagating wave, energy transfer amongst waves due to (near) resonance can occur when the resonance conditions are met, i.e. matching of the wave speed, length and direction. This is referred to as triad wave-wave interactions (Holthuisen, 2007). Moreover, the nonlinear wave-wave interaction transfers energy through super-harmonic interactions to higher frequencies (its frequency is the sum of the frequencies) and through sub-harmonic interactions to lower frequencies (its frequency is the difference between the frequencies); see Figure 2.2 for the energy flows through a spectrum. Also, the waves created by sub-harmonic interactions appear to have a broader directional range of the energy density spectra (Toledo, 2013). Further, this energy transfer to sub-harmonics and super-harmonics gets stronger when waves become more nonlinear.

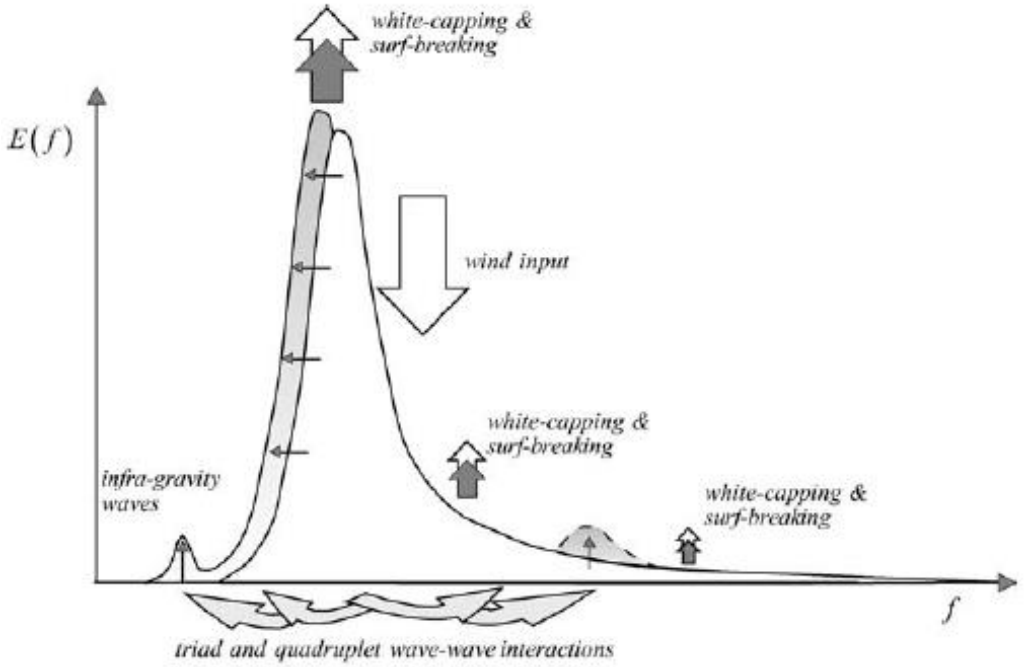

Figure 2.2. Energy flows through a wave spectrum in shallow water. Note the energy flow due to the triad and quadruplet wave-wave interactions to sub-harmonics and super-harmonics (Holthuisen, 2007).

In deep water triad wave-wave interactions do not occur because the matching of the wave speed, length and direction with the third freely propagating wave is not possible. However, quadruplet wave-wave interactions do occur which transfers energy between four, instead of three, wave components. Moreover, the quadruplet wave-wave interactions can stabilize the shape of a spectrum.

Scaling laws

Physical experiments are sometimes used for design studies of for instance breakwaters. Because physical model scales are small, scaling laws need to be applied to get to full scale or prototype scale. One of the crucial aspects in up-scaling is to determine which forces are governing and consequently, choose a similitude law which makes sure that the most important forces are scaled correctly.

The two most common similitude laws for water phenomenon are Froude and Reynolds similarity. Froude similarity makes sure that gravity and inertia forces are scaled properly while Reynolds scaling makes sure inertia and viscous forces are scaled properly. For more information about similitude laws and scaling, the reader is referred to (Frostick et al., 2011). In Table 2.1, a selection of scaling factors for Froude scaling, which are relevant for this thesis are presented.

Table 2.1. Froude scaling. Note that α is the scaling factor when a scale 1:α is used, ρ_m the density on model scale and ρ_f the density on full scale or prototype scale.

Physical parameter	Unit	Multiplication factor
Length	[m]	α
Volume	[m3]	α^3
Structural mass	[Kg]	$\alpha^3 * \rho_f / \rho_m$
Time	[s]	$\sqrt{\alpha}$
Frequency	[Hz]	$1/\sqrt{\alpha}$

2.2 Wave processes involved in navigation channels

The entrance of a harbour needs to be wide and deep enough to allow large ships to enter. In order to reach the required water depth, approach channels are dredged which can be several kilometres long. These long and deep channels have a large impact on waves propagating towards a harbour. The water depth inside the channel is larger than the water depth outside, which causes the waves inside the channel to travel faster than the waves outside. When waves travel parallel to the channels axis, waves will refract due to the channel slopes and diffract due to the celerity difference out of the approach channel, leading to less wave penetration into the port (wave defocussing), see Figure 2.3 (a). Waves that leave the channel interact with the undisturbed incoming waves leading to a local increase in wave height just outside the channel; this is also referred to as wave focussing.

Refraction theory

According to linear refraction theory, there is a critical angle which determines if waves can or cannot cross the channel, i.e. are transmitted or reflected. This critical angle is dependent on the wave celerity inside and outside the channel and can be found with Snell's law. The maximum angle of the propagating waves inside the channel for which no reflection occurs is 90° (for the definition of the angle, see Figure 2.3). Using this angle together with Snell's law gives the critical angle, presented in Eq. (2.1). For transitional water depths the phase celerity is given in Eq. (2.2). Waves, outside the channel and with an angle smaller than the critical wave angle ($\theta < \theta_{cr}$), can cross the channel, see Figure 2.3 (b).

$$\theta_{cr} = \arccos\left(\frac{c_{out}}{c_{in}}\right) \tag{2.1}$$

$$c = \frac{gT}{2\pi}\tanh(kd) \tag{2.2}$$

With:

	θ_{cr}	Critical angle (°)
	c_{out}	Wave celerity outside the channel (m/s)
	c_{in}	Wave celerity inside the channel (m/s)
	c	Wave celerity in transitional water (m/s)
	T	Wave period (s)
	g	Gravitational acceleration (m^2/s)
	d	Water depth (m)
	k	Wave number (rad/m)

Figure 2.3 (c) illustrates the effect of incoming waves with different frequencies (wave periods) and consequently different phase celerity's, with an angle of approach close to the critical angle. Lower frequency waves have a lower critical angle, so are more likely to be reflected. This is because for high frequency waves, the kd value becomes large and $\tanh(kd)$ approaches one, resulting in less depth dependency, see Eq. (2.2). Therefore, high frequency waves are less affected by the sudden drop in depth and have a higher critical angle accordingly.

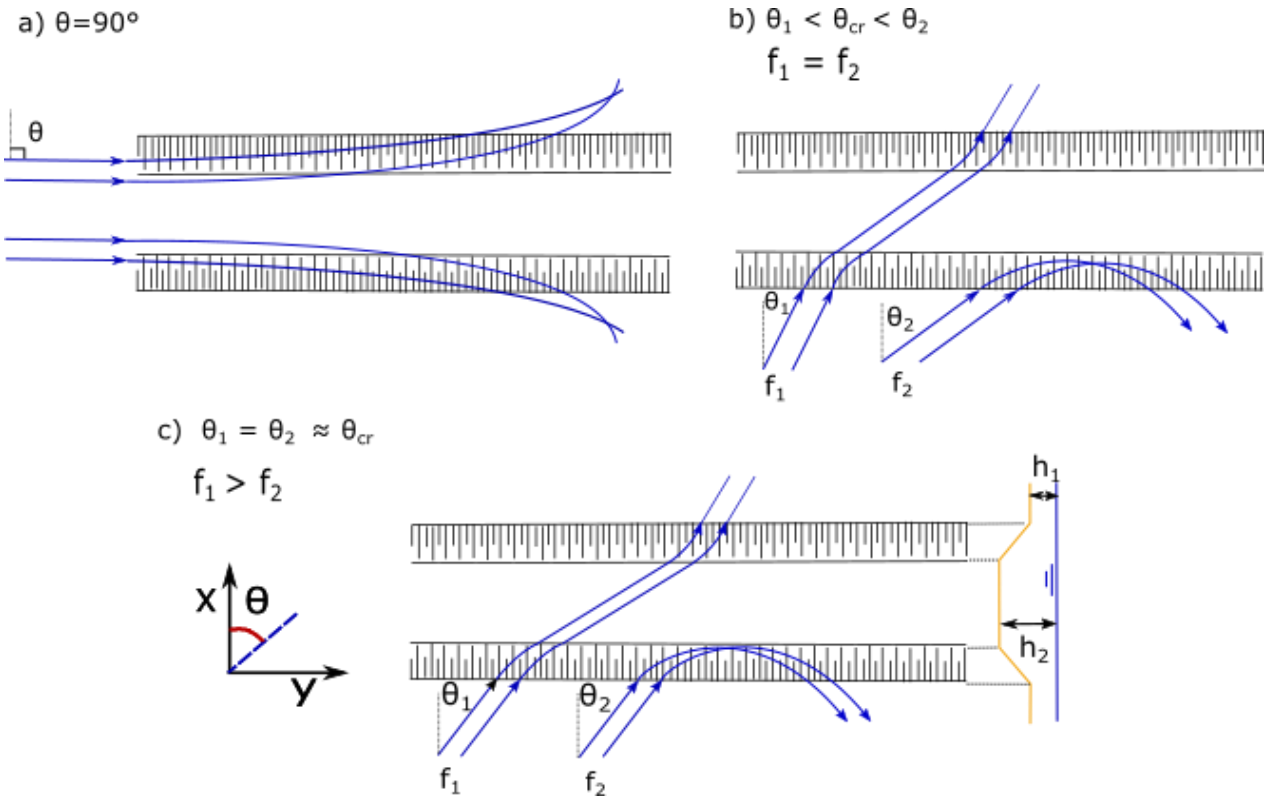

Figure 2.3. Wave refraction across a channel. (a) for waves parallel to the channel axis; (b) waves with the same frequency but different angles of approach; (c) waves with the same angle of approach but with different frequencies (after Dusseljee et al. (2012), Zwamborn and Grieve (1974))

Figure 2.4 shows a wave spectrum for waves which approach a navigation channel under a fixed angle of approach ($\theta = constant$), which is close to the critical angle. The high frequency waves are able to cross the channel, but the low frequency waves cannot (in this fictional case with a constant incoming wave angle for all frequencies). This demonstrates the importance of modelling the shape of the spectrum correctly.

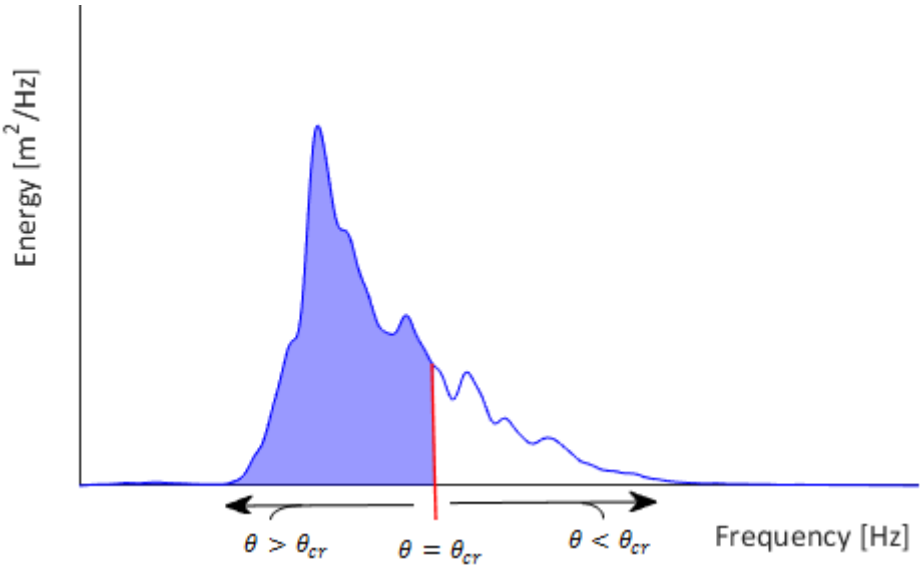

Figure 2.4. Incoming wave spectra for waves with a constant angle of approach θ. The coloured part of the spectra is not able to cross the channel, while the uncoloured part is.

Diffraction effects

The critical angle as defined by linear refraction theory only depends on the water depths and celerity's, inside and outside the channel and therefore only accounts for refraction. Further, the theory predicts an abrupt transition between reflected and transmitted waves. In reality, more physical processes play an important role which may allow waves with an angle greater than the critical angle to cross the channel and causing the transition between reflected and transmitted waves to be smoother.

When the width and the cross-sectional area are taken into account, diffraction effects start to play a role. Kirby and Dalrymple (1983) showed that waves may be (partially) transmitted when the incident wave angle is greater than the critical angle. Dusseljee et al. (2014) presented a modelling guideline whether or not diffraction effects need to be taken into account when modelling waves crossing a channel. Their assessment on the importance of diffraction can be made with the relative water depth (h_{in}/h_{out}), the incoming wave angle Θ and the relative wave period $T_0\sqrt{(g/h_{out})}$ outside the channel. Moreover, they concluded that diffraction effects are more pronounced for large $T_0\sqrt{(g/h_{out})}$, i.e. long waves. Also, wider channels lead to less wave transmission because the evanescent waves weaken in the deep part of the channel.

Tunnelling

Wave tunnelling is a phenomenon which allows wave transmission towards deeper water depths (inside the channel) than would be possible by refraction theory (Magne et al., 2007). It is a result of the combined effect of refraction, reflection, diffraction and exponentially decreasing (evanescent) modes in the channel direction. Evanescent modes are induced by the channel slopes and by partial wave reflection (Kirby and Dalrymple, 1983) and are spatially-decaying modes corresponding to the imaginary part of the wave number (Mei et al., 2016).

Random waves

Real sea states have a wide spread in frequencies and directions and therefore do not have one critical angle. As can be seen from Figure 2.3 (c), waves with different frequencies have different critical angles. Thus, when wave energy approaches a channel from one direction, the energy present in the upper part of the wave spectrum is able to cross the channels while the energy present at the lower part of the spectrum is not transmitted, see Figure 2.4. Furthermore, directional spreading results in a variety of incident wave angles. The wave energy present at wave angles lower than the critical angle can cross the approach channel.

Non- linear wave interactions

Groeneweg et al. (2014, 2015) raised and confirmed the hypothesis that sub-harmonic and super-harmonic interactions (nonlinear wave interactions) are an important process in determining the amount of transmitted wave energy. Neglecting these harmonic interactions lead to an under-prediction of wave energy crossing the channel. Groenenweg et al. (2014, 2015) and Dusseljee et al. (2014) found that SWAN under-estimates the wave height by 30-45% in the channel as well as after the channel. This under-estimation depends on the angle of approach and gets larger when waves become more non-linear and the energy transfer to sub- and super harmonics becomes stronger.

As explained in Section 2.1, sub harmonic interactions lead to a wider directional spreading of wave energy. Due to the broadening of the directional range of the energy density spectrum there is more

wave energy present at angles which are smaller than the critical angle and thus more energy can cross the channel compared with the original directional range of the energy density spectrum.

2.3 Numerical model classes

Many different wave models exist throughout literature which can be used for numerical modelling of wave penetration in harbours and access channels. Van Mierlo (2014) provided an overview of a variety of wave model classes relevant for wave penetration studies. Furthermore, an indication of which numerical model class can be used best in a particular situation is presented. The focus in this section lies on two classes of numerical models, i.e. Boussinesq-type models (MIKE 21bw is of this class) and non-hydrostatic models (SWASH is of this class).

2.3.1 Boussinesq-type models

Particle motions of waves in very shallow water are almost horizontal and the vertical accelerations are negligible. When this is the case, the shallow water equations can be used. Before waves enter very shallow water, the vertical accelerations cannot be ignored and a different theory is needed. The theory of Boussinesq does take vertical accelerations, up to a certain extent, into account and can be used for deeper waters than the shallow water equations.

The original derivation of the Boussinesq equations was done by Boussinesq as early as 1872. The starting assumptions are an incompressible fluid, a constant density, irrotational flow and the fluid can be described by a 3D velocity potential (Borsboom et al., 2001). Now, the essence of the Boussinesq equations is the elimination of the vertical coordinate, while still accounting for the vertical accelerations and the resulting non-hydrostatic pressure through higher order derivative (3rd order or higher) terms in the differential equations. Without these higher order terms, the shallow water equations are obtained (Dingemans, 1997). On the contrary to the shallow water equations, the Boussinesq equations can model frequency dispersion up to a certain extent due to the higher order derivative terms present in the differential equations. Adding even higher order derivatives improves the frequency dispersion, but increases the complexity of the momentum equations and therefore the computational costs for solving them.

Classical Boussinesq equations

Many different types of Boussinesq equations exist throughout literature, with the main difference arising from how the vertical acceleration is taken into account. The classical Boussinesq equations as derived by Peregrine (1967) and used in MIKE 21bw in terms of flux densities (depth integrated velocity components) is given in Eqs. (2.3-2.7).

$$\frac{\partial \xi}{\partial t} + \frac{\partial P}{\partial x} + \frac{\partial Q}{\partial y} = 0 \tag{2.3}$$

$$\frac{\partial P}{\partial t} + \frac{\partial}{\partial x}\left(\frac{P^2}{h}\right) + \frac{\partial}{\partial y}\left(\frac{PQ}{h}\right) + gh\frac{\partial \xi}{\partial x} = \psi_1 \tag{2.4}$$

$$\frac{\partial Q}{\partial t} + \frac{\partial}{\partial y}\left(\frac{Q^2}{h}\right) + \frac{\partial}{\partial x}\left(\frac{PQ}{h}\right) + gh\frac{\partial \xi}{\partial y} = \psi_2 \tag{2.5}$$

The two terms $\psi_1$and ψ_2 are the Boussinesq terms defined as:

$$\psi_1 = -\frac{1}{6}d^3\left(\frac{\partial^3\left(\frac{P}{d}\right)}{\partial t\partial x^2}+\frac{\partial^3\left(\frac{Q}{d}\right)}{\partial t\partial x\partial y}\right)+\frac{1}{2}d^2\left(\frac{\partial^3 P}{\partial t\partial x^2}+\frac{\partial^3 Q}{\partial t\partial x\partial y}\right) \quad (2.6)$$

$$\psi_2 = -\frac{1}{6}d^3\left(\frac{\partial^3\left(\frac{P}{d}\right)}{\partial t\partial x^2}+\frac{\partial^3\left(\frac{Q}{d}\right)}{\partial t\partial x\partial y}\right)+\frac{1}{2}d^2\left(\frac{\partial^3 P}{\partial t\partial x^2}+\frac{\partial^3 Q}{\partial t\partial x\partial y}\right) \quad (2.7)$$

With:

x, y	Horizontal coordinates (m)
t	Time (s)
g	Gravitational acceleration (m^2/s)
ξ	Water surface elevation, measured from still water level (m)
d	Still water depth, measured from still water level till bottom (m)
h	Total water depth (= $\xi + d$) (m)
P	Flux density in x-direction ($m^3/m/s$)
Q	Flux density in y-direction ($m^3/m/s$)

Eq. (2.3) is the continuity equation, Eq. (2.4) the momentum equation in x-direction and Eq. (2.5) is the momentum equation in y-direction. The higher order derivative terms can be recognised in the Boussinesq terms Eqs. (2.6-2.7). Note that ignoring these terms results in the shallow water equations.

Because the Boussinesq equations are based on shallow water assumptions (i.e. eliminating the z-coordinate from the 3D equations), a severe application limit of this class is the deep water limit, often expressed as h/L_0 (depth to deep water wavelength) or kh (wave number k (= $\frac{2\pi}{L_0}$) multiplied with the water depth). Hence, frequency dispersion can only be modelled accurate up to a certain extent, depending on the water depth. If kh values larger than the limit are used, significant errors in the linear dispersion occur. For modelling applications, in for instance MIKE 21bw, this translates in a minimum wave period the numerical model can resolve given a certain water depth.

Enhanced Boussinesq equations

Many researchers have tried to modify the original Boussinesq equations in order to improve the deep water limit and hence model frequency dispersion more accurate. A successful improvement was made by (Madsen et al, 1991) for a horizontal bottom and later by (Madsen and Sørensen, 1992) for a slowly varying bathymetry. These enhanced equations are also incorporated in MIKE 21bw, see Chapter 3 for more details.

2.3.2 Non-hydrostatic models

Hydrostatic models have been used numerous times for civil engineering purposes and are usually sufficiently accurate. However, they cannot be used if the assumption of hydrostatic pressure is no longer valid. This is for instance the case for waves propagating over steep slopes or for short waves (wave height/length ratio is not small).

A more recent class of numerical models that does not assume hydrostatic pressure are the non-hydrostatic models. Major contributions in the development of this class of models started with the works of Casulli and Stelling (1998) and Stansby and Zhou (1998). The non-hydrostatic terms can be found in the horizontal momentum equations. Further, the equations consist of the non-linear shallow water equations together with a vertical momentum equation. Inclusion of the non-hydrostatic part in the equations involves (for some proposed methods) a time consuming Poisson-equation solution (Stansby and Zhou, 1998) which is computationally expensive. Many solutions are therefore sought which split the hydrostatic from the non-hydrostatic pressure and only include the non-hydrostatic part in areas where it has a large influence in order to minimize computational demand. A great difficulty with this is that it introduces splitting errors. Solutions that do not split the hydrostatic and the non-hydrostatic pressure exist as well. It turned out however that these models become quickly unstable when there are strong vertical accelerations involved. For an overview of non-hydrostatic computing including splitting of the pressure terms as well as solutions that do not split the pressure terms, the reader is referred to Zijlema and Stelling (2005).

Contrary to the Boussinesq equations, the vertical coordinate is not removed from the 3D partial differential equations. Instead, the vertical is discretised by dividing it in vertical layers. Therefore, the vertical structure of the flow is part of the actual solution and is not imposed as in the Boussineq equations. To illustrate this clearly, the 3D Euler equations as given by Stelling and Zijlema (2003) are given in Eqs. (2.9-2.11), together with the continuity equation presented in Eq. (2.8). They decomposed the pressure p into a hydrostatic part p_h and a non-hydrostatic part q, i.e. $p = p_h + q$. Further, the hydrostatic balance between gravity and the hydrostatic part ($\frac{\partial p_h}{\partial z} = -g$) was subtracted out of Eq. (2.11).

$$\frac{\partial u}{\partial t} + \frac{\partial v}{\partial y} + \frac{\partial w}{\partial z} = 0 \tag{2.8}$$

$$\frac{\partial u}{\partial t} + u\frac{\partial u}{\partial x} + v\frac{\partial u}{\partial y} + w\frac{\partial u}{\partial z} + g\frac{\partial \xi}{\partial x} + \frac{\partial q}{\partial x} = 0 \tag{2.9}$$

$$\frac{\partial v}{\partial t} + u\frac{\partial v}{\partial x} + v\frac{\partial v}{\partial y} + w\frac{\partial v}{\partial z} + g\frac{\partial \xi}{\partial y} + \frac{\partial q}{\partial y} = 0 \tag{2.10}$$

$$\frac{\partial w}{\partial t} + u\frac{\partial w}{\partial x} + v\frac{\partial w}{\partial y} + w\frac{\partial w}{\partial z} + \frac{\partial q}{\partial z} = 0 \tag{2.11}$$

Where u, v, w the velocities (m/s) in x-, y- and z-direction, respectively. The differences with the (classical) Boussinesq equations (Eq. 2.3-2.7), as explained above can clearly be seen.

The non-hydrostatic part (q) accounts for the vertical distribution of the velocities and consequently, enables the modelling of frequency dispersion. Hence, there is no need for higher order (3rd or higher) terms as is the case with the Boussinesq equations. How accurately frequency dispersion can be resolved depends on the resolution of the vertical grid. The finer this grid, the more accurate frequency dispersion can be modelled. The application limits of this class regarding the water depth (or kh value) can therefore easily be extended by simple increasing the resolution of the vertical dimension. Nevertheless, non-hydrostatic models need quite a large number of vertical layers to be able to resolve frequency dispersion accurate (Zijlema and Stelling, 2008).

3 Phase-resolving numerical models SWASH and MIKE 21bw

In this chapter the two numerical phase resolving models MIKE 21bw and SWASH are introduced. Their underlying equations, assumptions, numerical aspects and previous validation studies are presented. First, MIKE 21bw will be described in Section 3.1, followed by SWASH in Section 3.2. Previous comparison studies between the two numerical models are presented in Section 3.3. Section 3.4 provides conclusions about the main theoretical differences between the two numerical models.

3.1 MIKE 21bw

MIKE 21bw (Boussinesq waves) is a Boussinesq type model which is used for studies of wave penetration in harbours and coastal areas. It is a phase-resolving numerical wave module which is part of DHI's MIKE 21 and includes two modules, 1DH and 2DH, which covers one and two horizontal space co-ordinates, respectively. For this thesis use was made of the 2DH module and therefore this module is further evaluated in this chapter.

The following physical wave phenomena are taken into account which are of interest in ports and access channels (DHI, 2007):

- Shoaling
- Refraction
- Diffraction
- Wave breaking
- Bottom dissipation
- Partial reflection
- Wave transmission
- Nonlinear wave-wave interactions

For this thesis, the MIKE 2014 software package was used. Moreover, it is a commercial software which is not freely available. For this thesis use was made of an academic license provided by DHI.

3.1.1 Model equations and assumptions

MIKE 21bw is a time domain model which solves either the classical or the enhanced Boussinesq equations as derived by Madsen et al. (1991) and Madsen and Sørensen (1992). The full equations which MIKE 21bw solves are presented in Eqs. (3.1-3.3) (DHI, 2015).

Continuity

$$n\frac{\partial \xi}{\partial t}+\frac{\partial P}{\partial x}+\frac{\partial Q}{\partial y}=0 \tag{3.1}$$

X-momentum

$$n\frac{\partial P}{\partial t}+\frac{\partial}{\partial x}\left(\frac{P^2}{h}\right)+\frac{\partial}{\partial y}\left(\frac{PQ}{h}\right)+n^2gh\frac{\partial \xi}{\partial x}+\frac{\partial R_{xx}}{\partial x}+\frac{\partial R_{xy}}{\partial y}+n^2P\left[\alpha+\beta\frac{\sqrt{P^2+Q^2}}{h}\right]+\frac{gP\sqrt{P^2+Q^2}}{h^2C^2}+F_x+n\psi_1=0 \tag{3.2}$$

y-momentum

$$\underbrace{n\frac{\partial Q}{\partial t}+\frac{\partial}{\partial y}\left(\frac{Q^2}{h}\right)+\frac{\partial}{\partial x}\left(\frac{PQ}{h}\right)+n^2gh\frac{\partial \xi}{\partial y}}_{\text{(I)}}+\underbrace{\frac{\partial R_{yy}}{\partial x}+\frac{\partial R_{xy}}{\partial x}}_{\text{(II)}}+\underbrace{n^2Q\left[\alpha+\beta\frac{\sqrt{P^2+Q^2}}{h}\right]}_{\text{(III)}}+\underbrace{\frac{gQ\sqrt{P^2+Q^2}}{h^2C^2}}_{\text{(IV)}}+\underbrace{F_y}_{\text{(V)}}+\underbrace{n\psi_2}_{\text{(VI)}}=0 \tag{3.3}$$

In the Eqs. (3.1-3.3), the shallow water equations can be recognised with number (I) (blue color), which includes a term of the local change over time, two advection terms and a gravitational term. The term (II) (red) accounts for wave breaking, number (III) (purple) accounts for energy dissipation in porous media, number (IV) (orange) accounts for bottom friction, number (V) (grey) is the horizontal stress term and number (VI) (green) is the dispersive Boussinesq term which makes it possible to include frequency dispersion in the computations. These dispersive Boussinesq terms are presented in Eqs. (3.4-4.5).

$$\begin{aligned}\psi_1 = &-\left(B+\frac{1}{3}\right)d^2\left(\frac{\partial^3 P}{\partial t\partial x^2}+\frac{\partial^3 Q}{\partial t\partial y\partial x}\right)-nBgd^3\left(\frac{\partial^3 \xi}{\partial x^3}+\frac{\partial^3 \xi}{\partial x^2\partial y}\right)\\&-d\frac{\partial d}{\partial x}\left(\frac{1}{3}\frac{\partial^2 P}{\partial t\partial x}+\frac{1}{6}\frac{\partial^2 Q}{\partial t\partial y}+nBgd\left(2\frac{\partial^2 \xi}{\partial x^2}+\frac{\partial^2 \xi}{\partial y^2}\right)\right)-d\frac{\partial d}{\partial y}\left(\frac{1}{6}\frac{\partial^2 Q}{\partial t\partial x}+nBgd\frac{\partial^2 \xi}{\partial x\partial y}\right)\end{aligned} \tag{3.4}$$

$$\begin{aligned}\psi_2 = &-\left(B+\frac{1}{3}\right)d^2\left(\frac{\partial^3 Q}{\partial t\partial y^2}+\frac{\partial^3 P}{\partial t\partial y\partial x}\right)-nBgd^3\left(\frac{\partial^3 \xi}{\partial y^3}+\frac{\partial^3 \xi}{\partial x^2\partial y}\right)\\&-d\frac{\partial d}{\partial y}\left(\frac{1}{3}\frac{\partial^2 Q}{\partial t\partial y}+\frac{1}{6}\frac{\partial^2 P}{\partial t\partial x}+nBgd\left(2\frac{\partial^2 \xi}{\partial y^2}+\frac{\partial^2 \xi}{\partial x^2}\right)\right)-d\frac{\partial d}{\partial y}\left(\frac{1}{6}\frac{\partial^2 P}{\partial t\partial y}+nBgd\frac{\partial^2 \xi}{\partial x\partial y}\right)\end{aligned} \tag{3.5}$$

With:

	x, y	Horizontal coordinates (m)
	t	Time (s)
	g	Gravitational acceleration (m^2/s)
	ξ	Water surface elevation, measured from still water level (m)
	d	Still water depth, measured from still water level till bottom (m)
	h	Total water depth ($\xi + d$) (m)
	P	Flux density in x-direction ($m^3/m/s$)
	Q	Flux density in y-direction ($m^3/m/s$)
	α	Resistance coefficient for laminar flow in porous media (-)
	β	Resistance coefficient for turbulent flow in porous media (-)
	C	Chezy resistance number ($m^{0.5}/s$)
	n	Porosity (-)
	B	Coefficient (-)

The horizontal stress terms are defined in Eqs. (3.6-3.7).

$$F_x = -\left(\frac{\partial}{\partial x}\left(\upsilon_t\frac{\partial P}{\partial x}\right)+\frac{\partial}{\partial y}\left(\upsilon_t\left(\frac{\partial P}{\partial y}+\frac{\partial Q}{\partial x}\right)\right)\right) \tag{3.6}$$

$$F_y = -\left(\frac{\partial}{\partial y}\left(\upsilon_t\frac{\partial Q}{\partial y}\right)+\frac{\partial}{\partial x}\left(\upsilon_t\left(\frac{\partial Q}{\partial x}+\frac{\partial P}{\partial y}\right)\right)\right) \tag{3.7}$$

With υ_t the turbulent eddy viscosity (m^2/s) which is estimated using the Smagorinsky formulation, for details see Sørensen et al. (2004).

The linear dispersive coefficient B is used as a curve fitting parameter in order to get the best agreement of the group velocity and phase celerity with Stokes first order theory. Madsen and Sørensen (1992) recommended B = 1/15 for which the best results are obtained. Note that with B = 0, the classical Boussinesq terms are obtained as given in Eqs. (2.6-2.7). The application limits for different values of the coefficient B are:

- For B = 0: kh < 1.4 (h/L_0 < 0.22)
- For B = 1/15: kh < 3.1 (h/L_0 < 0.5)

With: k Wave number, defined as $(2\pi/L_0)$ (rad/m)
h Water depth (m)
L_0 Deep water wavelength (m)

If the maximum water depth inside the computational domain is known and using the expression from linear wave theory to determine the deep water wave length ($L_0 = \frac{2\pi}{\sqrt{gh}}$), the application limit can also be expressed as a minimum wave period the model can resolve and is given in Eq. (3.8).

$$T_{min} \geq \sqrt{\frac{2\pi h_{max}}{g\beta}} \tag{3.8}$$

With: T_{min} Minimum wave period the model is able to resolve (s)
h_{max} Maximum water depth inside the computational domain (m)
g Gravitational acceleration (m^2/s)
β β=0.22 for classical and $\beta = 0.5$ for enhanced Boussinesq (-)

Wave breaking

The assumption of irrotational flow was made in the derivation of the Boussinesq equations, which makes the modelling of wave breaking not straightforward. In MIKE 21bw wave breaking is included by adding a dissipation term to the differential equations and is based on the concept of surface rollers. The terms which take the excess momentum which originates from the surface roller into account are defined in Eqs. (3.9-3.11) (Schäffer et al., 1993).

$$R_{xx} = \frac{\delta}{1-\frac{\delta}{h}}\left(c_x - \frac{P}{h}\right)^2 \tag{3.9}$$

$$R_{xy} = \frac{\delta}{1-\frac{\delta}{h}}\left(c_x - \frac{P}{h}\right)\left(c_y - \frac{Q}{h}\right) \tag{3.10}$$

$$R_{yy} = \frac{\delta}{1-\frac{\delta}{h}}\left(c_y - \frac{Q}{h}\right)^2 \tag{3.11}$$

With c_x and c_y components of the roller celerity (m/s) in x- and y-direction, respectively, and δ the roller thickness (m) which is a function of the horizontal coordinates and time. Figure 3.1 provides a sketch with the definition of the parameters.

The basic principle of the surface roller is that it is considered as a volume of water on top of the water surface. Further, the surface roller is transported by the wave celerity. The assumed distribution of the horizontal velocities over the vertical is given in Figure 3.1 (right sketch).

Breaking is initiated when the (local) slope of the surface is larger than an initial defined breaking angle. This initial breaking angle differs for different breaker types (i.e. spilling, surging and plunging breakers) and a value of 20° is assumed for spilling breakers in MIKE 21bw, based on Schäffer et al. (1993). For the full details of how wave breaking is modelled in MIKE 21bw, the reader is referred to Madsen et al. (1997a).

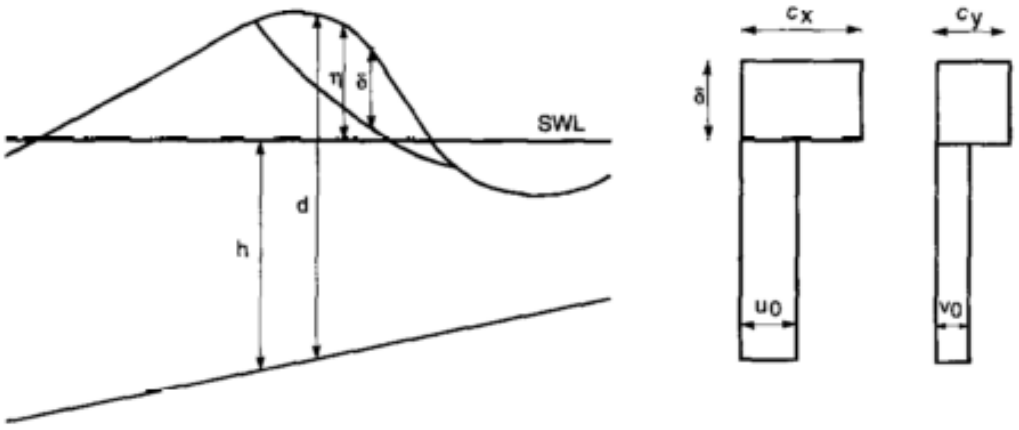

Figure 3.1. Left sketch, definition of parameters used for the modelling of breaking waves. Right sketch, the assumed horizontal velocities over the vertical profile (Madsen et al., 1997a)

3.1.2 Boundary conditions and schematisations

Wave generation

The boundaries of the computational domain can either be open or closed. At the open boundaries, the incoming waves can be specified. Another way of generating incoming waves is by a so called 'internal wave generation line'. This line can be specified everywhere in the domain, with the restriction that it should be parallel with the x- or y-axis of the bathymetry. The main advantage of placing the generation line inside the domain, instead of imposing it at an open boundary, is that a sponge layer can be placed at the boundary to dissipate all the wave energy leaving the computational domain.

The wave data needed at the wave generation line (either at the open boundary or at the internal generation line) depends on the form of the Boussinesq equations. For the enhanced equations the flux density and the slope of the surface elevation has to be specified at all grid point along the generation line for each time step. In order to prepare this input, MIKE 21bw has toolboxes which generate this input from wave spectra, time series or from a given wave height and period. Consequently, regular as well as irregular waves can be specified. Note that no waves can be generated with a period smaller than the minimum period as defined in Eq. (3.8).

Sponge layers

Sponge (absorbing) layers are numerical wave absorbers which can be specified at the boundaries in order to absorb wave energy radiating out of the computational domain. These radiation boundary conditions are based on Larsen and Dancy (1983). They found that a sponge layer with a width of only 5% of the wave length resulted in a reflection less than 7% magnitude. To minimize the reflection as much as possible, it is recommended to use sponge layers with a width of one to two times the wave length which corresponds to the most energetic waves.

Porosity layers

Porosity layers can be specified in the computational domain to model partial reflection and transmission. Two different types of structures can be modelled with porosity layers, i.e. permeable and non-permeable structures. Non-permeable structures need to be backed up by land and only have wave reflection, while permeable structures have both wave reflection and transmission.

A porosity number need to be specified which depends on the amount of reflection or transmission required. MIKE 21bw has a toolbox which calculates the reflection and transmission coefficients as function of the porosity, width of the porosity layer, diameter of the stones, the water depth, the wave height and wave period. The method is based on Madsen (1983) and Madsen and Warren (1984). For the detailed equations and their derivations the reader is referred to these papers. By means of example, a graph created by MIKE 21bw toolbox for a permeable structure modelled as a porosity layer is presented in Figure 3.2 which relates the porosity to the reflection/transmission coefficient. It can be seen from this figure that when both transmission and reflection play a role, it is not possible to choose both the reflection and the transmission coefficient freely. For practical applications this is usually not a problem. For instance, breakwaters are structures which have both transmission and reflection. Because engineers are primarily interested in what happens behind a breakwater, in the sheltered area, the porosity is usually chosen so that it corresponds with the transmission coefficient.

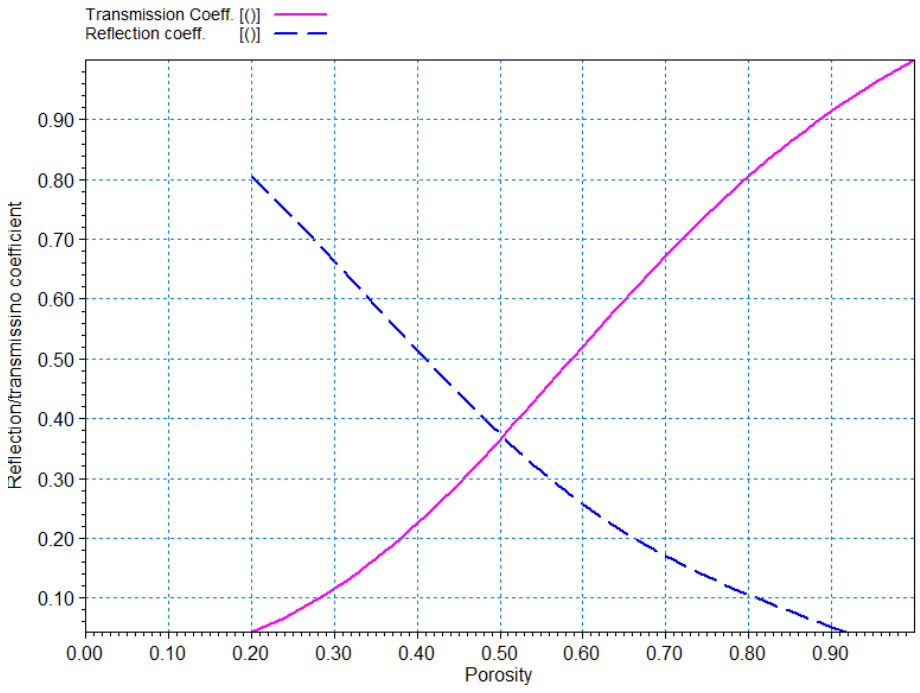

Figure 3.2. Transmission and reflection coefficients as function of porosity values generated by MIKE 21bw toolbox.

In Eqs. (3.1-3.3) the porosity value (n) takes reflection and transmission into account. Further, the terms (III) (purple) in Eqs. (3.2-3.3) take the energy dissipation inside a permeable structure into account. The values α and β are the resistance coefficients for laminar and turbulent flow, respectively. These values are determined by the empirical formulas as given by Engelund (1953) and are presented in Eqs. (3.12-3.13).

$$\alpha = \alpha_0 \frac{(1-n)^3}{n^2} \frac{\upsilon}{d^2} \tag{3.12}$$

$$\beta = \beta_0 \frac{(1-n)}{n^3} \frac{1}{d} \tag{3.13}$$

With:
- d Grain size (m)
- n Porosity (-)
- υ Kinematic viscosity (m^2/s)
- α_0 Particle form constant (Default = 1000)
- β_0 Particle form constant (Default = 2.8)

Sloping boundaries

MIKE 21bw requires a minimum water depth in order to be able to run stable computations. The minimum water depth determines (together with the minimum wave period) the minimum wave length the model needs to resolve and consequently also determines the minimum grid size needed. Further, when the minimum water depth is small compared to the wave height, wave breaking occurs which requires a fine horizontal grid resolution to be able to run stable computations.

Sloping boundaries cannot be modelled in full detail because this would violate the minimum water depth requirement. In Figure 3.3 (left plots) a cross section of a sloped breakwater is given, together with some schematisations in MIKE 21bw. Schematisation (I) is preferred because it still includes some part of the slope and will therefore model the relevant wave phenomena (reflection, shoaling, diffraction, refraction) more accurate than the other schematisations.

But, when the incoming waves are relatively high compared to the water depth (large a/h ratio), the minimum water depth comes close to the actual water depth to avoid wave breaking. In this case, the breakwater is schematised as a vertical wall and does not account for the slope anymore. Three different possibilities are presented in the left plots of Figure 3.3 (schematisation II, III, IV). The head of the breakwater is modelled as a vertical wall as well and therefore schematisation (II) will result in the shortest breakwater length, while schematisation (IV) leads to the largest length. Consequently, schematisation (II) results in the most wave energy penetration a port, while schematisation (IV) will give the least amount of wave energy penetration. To illustrate the schematisations more clearly, the right plot of Figure 3.3 shows the original breakwater (including the slope) and schematisation (II) in pink.

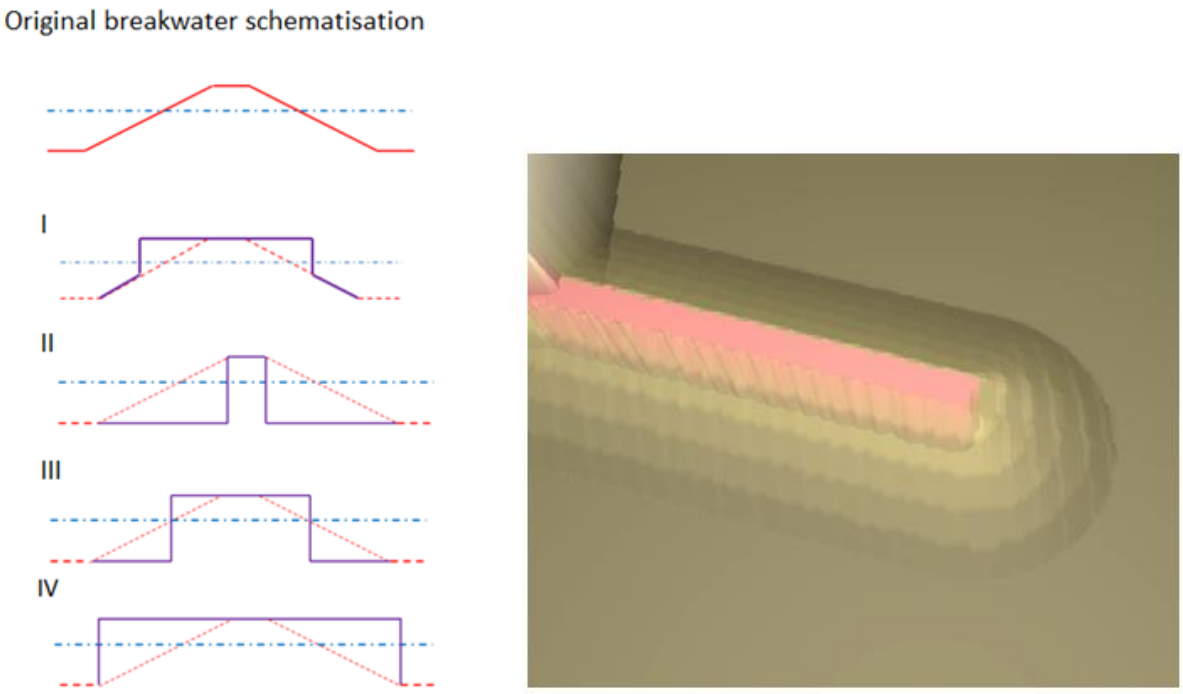

Figure 3.3. Left figures, cross section schematisation of a breakwater in MIKE 21bw. The red line is the measured profile of the breakwater used in the physical model tests of the harbour (see Section 5.1) and the purple lines represent possible schematisations in MIKE 21bw. Right figure, a 3D plot of a breakwater together with schematisation (II) (in pink) for MIKE 21bw.

3.1.3 Numerical aspects

Computational grid

The Boussinesq equations are discretised on a rectangular staggered grid. The flux components (P and Q) are defined exactly halfway between the grid points, whereas the scalar quantities are defined at the grid points, see Figure 3.4. Important to note is that the computational grid resolution is identical to the bathymetric resolution.

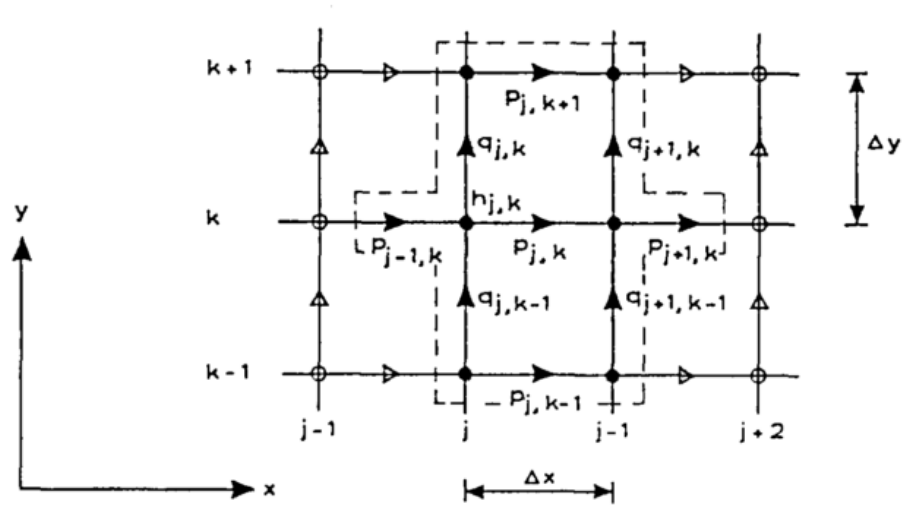

Figure 3.4. Staggered grid as defined in MIKE 21bw. (Madsen and Sørensen, 1992)

Numerical Schemes

The time integration is done using a time-centered implicit scheme. The method applied can be found in detail in Madsen et al. (1991) and is based on the so called ADI (Alternating Direction Implicit) algorithm with 'Side feeding', see Abbot and Mins (1998). The cross-Boussinesq terms (e.g. in x-direction $\frac{\partial^3 Q}{\partial t \partial y \partial x}, \frac{\partial^2 Q}{\partial t \partial y}\ and \frac{\partial^2 Q}{\partial t \partial x}$) are discretised by linear-time extrapolation to limit numerical damping (Madsen and Sørensen, 1992). In the MIKE 21bw module, the user can specify a so called time extrapolation factor between the values zero and one. A value of one corresponds to linear-time extrapolation of the cross Boussinesq terms and has the least amount of numerical damping. Further, a value of zero leads to backward centering of the Boussinesq terms and has a considerably amount of numerical damping. However, the advantage of backward centering is enhanced numerical stability.

Four different numerical schemes are available for the space discretisation of the partial differential Boussinesq equations. These four schemes are listed below (DHI, 2015).

- Central differencing with side-feeding
- Central differencing with simple upwinding at steep gradients and near land
- Quadratic upwinding with simple upwinding at steep gradients and near land
- Simple upwind differencing

The amount of numerical damping increases from the central differencing with side-feeding scheme (which has the least amount of numerical damping) up to the simple upwind differencing scheme which has the largest amount of numerical damping. Therefore, the central differencing with side-feeding should be used to avoid numerical damping as much as possible. However, this scheme gets unstable relatively quick if gradients in the convective terms are large and other schemes have to be used in that case.

Time step and grid size restrictions

When an explicit scheme is used for the discretisation of the differential equations, the time-step is restricted by the CFL condition ($C_r < 1$). If this condition is not fulfilled, the numerical domain of dependence can fall outside the analytical domain of dependence which leads to unrealistic results. For MIKE 21bw, the courant number is given in Eq. (3.14).

$$C_r = c\frac{\Delta t}{\Delta x} \tag{3.14}$$

With:
- C_r Courant number (-)
- c Wave propagation speed (m/s)
- Δt Time step (s)
- Δx Spatial resolution (m)

Further, the minimum wave period should be resolved with a minimum of 35 time steps to get accurate results. The restriction of the grid size was found to be less important and should be at least 7 grid points per minimum wave length (DHI, 2007).

Parallelization

Parallelisation is incorporated in MIKE 21bw using shared memory architecture. The benefit of using multiple processors can be expressed with a speed up factor S, defined in Eq. (3.15).

$$S_p = \frac{T_1}{T_p} \tag{3.15}$$

Where T_1 the computational time using only one core, T_p the computational time using p cores and S_p the speed up factor of p cores (relative to one core). The speed up factor which can be obtained using multiple cores is given in Figure 3.5 and is around 3-4 (DHI, 2015). Furthermore, a special license is needed in order to control the parallelization option in MIKE 21bw.

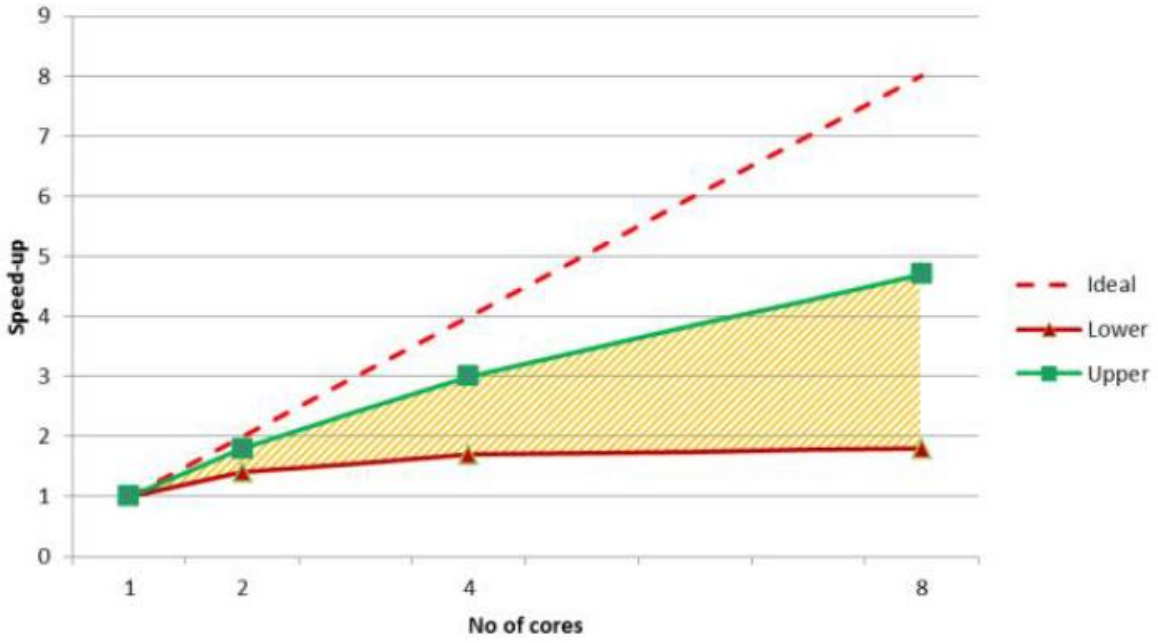

Figure 3.5. Speed up factor for MIKE 21bw (DHI, 2015). The shaded area between the upper and lower limit indicates the typical speed-up range.

3.1.4 Previous validation

Benchmark tests regarding the Boussinesq equations which are incorporated in MIKE 21bw have been conducted multiple times. A list is given in the MIKE 21bw user manual. In the following paragraphs, a short summary is given with multiple benchmark tests and validation studies on waves penetrating harbours.

Madsen and Sørensen (1992) verified the numerical tool for shoaling, refraction and diffraction in deep and shallow water with analytical results. Further, multiple tests were done regarding surf zone dynamics by Madsen et al. (1997a,b) and Sørensen et al. (1998) for the basic features in the case of regular waves, wave breaking (surface roller concept), linear dispersion characteristics, shoaling, run-up, generation of surf beats and moving shoreline. They concluded that the agreement with the physical model results and analytical results are satisfactory.

Madsen and Sørensen (1993) investigated wave-wave interactions in shallow water by applying the enhanced Boussinesq equations. It was found that wave transformations of irregular wave trains (monochromatic as well as bichromatic waves) showed reasonable agreement with measurements.

However, it was found that in general the super-harmonics are under-estimated and sub-harmonics can be under or over-estimated. Errors were found up to 40%, but on average the discrepancies were less than 10%.

Furthermore, Sørensen et al. (2004) presented four more test cases including nonlinear refraction-diffraction over a semi-circular shoal, shoaling and breaking of regular and irregular waves on a gentle sloping beach and a test for rip channels. The numerical results showed good agreement with the measurements.

A couple of validation studies regarding wave penetration studies have been performed by Koefoed-Hansen (2000, 2005). It was shown that the numerical and physical model results are in good agreement and that the model is able to predict non-linear features which are responsible for long wave agitation in harbours.

3.2 SWASH

The numerical phase resolving model SWASH (Simulating WAves till SHore) is a non-hydrostatic wave-flow model which can be used for simulating non-hydrostatic, free surface, rotational flows and transport phenomena in one, two or three dimensions. The main goal of the program is to provide a robust and efficient model which can be applied on different time and spatial scales in order to simulate surface waves and shallow water currents.

The model can account for many physical processes, a limited selection is given below, and for the full list of features the reader is referred to the SWASH user manual (The SWASH team, 2016).

- Wave propagation, frequency dispersion, shoaling, refraction and diffraction
- Nonlinear wave-wave interactions
- Wave breaking
- Wave run-up and run-down
- Partial reflection and transmission
- Wave interaction with structures
- Wave-current interaction
- Wave-induced currents
- Wave damping induced by aquatic vegetation

SWASH is developed at Delft University of Technology and is an open source code which can freely be downloaded from http://swash.sourceforge.net. The current version of the software package SWASH is 3.14 which is also used for this thesis.

3.2.1 Model equations and assumptions

The equations SWASH solves are based on the non-linear shallow water equations including non-hydrostatic pressure and can be derived from the incompressible Navier-Stokes equations. The Navier-Stokes equations are based on the conservation of mass and momentum. By using Reynolds decomposition (splitting the velocity in a mean (overbar) and fluctuating part (prime), i.e. $u = \overline{u} + u'$) and averaging, results in the Reynold-averaged Navier-Stokes equations (RANS). SWASH solves the RANS equations (together with continuity) by averaging over the vertical for each vertical layer. Depth averaged the equations are given in Eqs. (3.16-3.18) (Zijlema et al., 2011).

$$\frac{\partial \xi}{\partial t} + \frac{\partial hu}{\partial x} + \frac{\partial hv}{\partial y} = 0 \tag{3.16}$$

$$\frac{\partial u}{\partial t} + u\frac{\partial u}{\partial x} + v\frac{\partial u}{\partial y} + g\frac{\partial \xi}{\partial x} + \frac{1}{h}\int_{-d}^{\xi}\frac{\partial q}{\partial x}dz + c_f\frac{u\sqrt{u^2+v^2}}{h} = \frac{1}{h}\left(\frac{\partial h\tau_{xx}}{\partial x} + \frac{\partial h\tau_{xy}}{\partial y}\right) \tag{3.17}$$

$$\underbrace{\frac{\partial v}{\partial t} + u\frac{\partial v}{\partial x} + v\frac{\partial v}{\partial y} + g\frac{\partial \xi}{\partial y}}_{\text{(I)}} + \underbrace{\frac{1}{h}\int_{-d}^{\xi}\frac{\partial q}{\partial y}dz}_{\text{(II)}} + \underbrace{c_f\frac{v\sqrt{u^2+v^2}}{h}}_{\text{(III)}} = \underbrace{\frac{1}{h}\left(\frac{\partial h\tau_{yx}}{\partial x} + \frac{\partial h\tau_{yy}}{\partial y}\right)}_{\text{(IV)}} \tag{3.18}$$

With:	x, y	Horizontal coordinates (m)
	t	Time (s)
	g	Gravitational acceleration (m^2/s)
	ξ	Water surface elevation, measured from still water level (m)
	d	Still water depth, measured from still water level till bottom (m)
	h	Total water depth ($\xi + d$) (m)
	q	Non-hydrostatic pressure (normalised by the density)
	c_f	Dimensionless friction coefficient

The horizontal stresses are given in Eq. (3.19).

$$\tau_{xx} = 2\upsilon_t\frac{\partial u}{\partial x}, \tau_{xy} = \tau_{yx} = \upsilon_t\left(\frac{\partial v}{\partial x} + \frac{\partial y}{\partial y}\right), \tau_{yy} = 2\upsilon_t\frac{\partial v}{\partial y} \tag{3.19}$$

Where υ_t is the turbulent eddy viscosity (m^2/s) which is calculated by means of the Prandtl mixing length hypothesis, see Zijlema et al. (2011). The molecular viscosity has been neglected in the equations because it is order of magnitude smaller than the eddy viscosity.

In Eqs. (3.16-3.18) the non-linear shallow water equations (including a term with local change over time, two advection terms and a gravity term) can be recognised with number (I) (blue). Number (II) (red) indicates the non-hydrostatic pressure term, number (III) (purple) accounts for bottom friction and number (IV) (green) are the turbulent stress terms.

The surface elevation $\xi(x, y, t)$ in Eqs. (3.16-3.18) is a function of the horizontal coordinates and time. A drawback of this approach is that overturning waves cannot be modelled. However, the non-hydrostatic models cannot model all the details of wave breaking (such as air-entrainment) to begin with. Furthermore, for coastal engineering purposes there is no need for detailed modelling of wave breaking as long as the statistical effect on for instance the wave height is correct.

The energy dissipation of breaking waves in SWASH is taken into account by using the similarity between breaking waves and hydraulic jumps, by making sure that mass and momentum are conserved. However, this is only accurate when a sufficient amount of vertical layers (10-20) are used. When the vertical is discretised by just a few vertical layers (1-3), then the horizontal velocities of the waves will be under-estimated resulting in an under-estimation of the onset of wave breaking (Smit et al., 2013). In order to accurately take energy dissipation due to wave breaking into account when using a coarse vertical resolution, a hydrostatic front approximation is introduced by Smit et al.

(2013) which assumes a hydrostatic pressure in front of the wave to initiate wave breaking. The hydrostatic pressure in SWASH is used when the local surface steepness exceeds a pre-set value α, see Eq. (3.20) (The SWASH team, 2016). After the crest has passed, the non-hydrostatic pressure computation is used again.

$$\frac{\partial \xi}{\partial t} > \alpha \sqrt{gd} \tag{3.20}$$

3.2.2 Boundary conditions and schematisations

Wave generation
The boundaries in SWASH can either be open or closed. At the open boundaries waves can be generated. SWASH is able to generate regular waves (from time series or Fourier series), irregular uniform waves (by means of a 1D spectrum and irregular directional waves (by means of a 2D spectrum). At the boundaries where waves are generated, a radiation condition can be specified to minimize the amount of reflection.

Sponge layers
If there should be no reflection from a boundary, i.e. when waves should leave the domain freely without being reflected, sponge layers can be defined. These layers absorb the incoming wave energy while minimizing the artificial reflection as much as possible. The user manual suggests that the width of this layer should be at least 3-5 times the typical wave length, i.e. the wave length corresponding to the peak period.

Porosity layers
In order to model partial reflection/transmission at open boundaries or for instance a breakwater, porosity layers are defined. Beside the porosity, the stone size and the height of the structure should be defined. Further, the stone size and height of the structures can be constant, or vary over the domain. In the latter case, the stone size and the height of the structures should be defined in a separate file. A particle form factor for the laminar friction and for the turbulent friction loss has to be specified as well.

Other boundary conditions which can be imposed are (The SWASH team, 2016): velocity or discharge, Rieman invariants, Sommerfield or radiation conditions and periodic boundary conditions.

Sloping boundaries
Sloping boundaries such as for instance breakwaters or a beach can be modelled in SWASH as porous structures. The slope can be specified in full detail and there is no need to 'cut' the slope off as is the case for MIKE 21bw. This is because SWASH can compute the water depth for porous structures, even with a height which is larger than the water depth. Therefore, there is no need to specify a minimum water depth.

3.2.3 Numerical aspects

Computational grid

SWASH discretises the differential equations on a rectangular or a curvilinear staggered grid in the horizontal direction. The grid in the vertical is defined by a number of terrain following vertical layers. Further, there are two different arrangements of the staggered grid regarding the vertical pressure gradient: a standard layout where the vertical pressure gradient is located in the cell centre or the box layout where the pressure gradient is located at the layer interface. Which layout to choose depends on how the vertical pressure gradient is discretised (see next section about numerical schemes).

Numerical schemes

The time integration in SWASH is done by the explicit leapfrog scheme with a second order explicit time step for the advection terms. For the viscosity term a first order explicit time step is applied and finally for the non-hydrostatic part a first order implicit time step is used (Zijlema et al., 2011).

For the discretisation of the advection terms (for example: the advection terms of the u-momentum for the horizontal coordinates are: $u\frac{\partial u}{\partial x}, v\frac{\partial u}{\partial y}$), multiple schemes are available. The central schemes are generally accurate, but are very prone to generate wiggles. Schemes that add more numerical diffusion (e.g. upwind schemes) are not prone to wiggles, but instead damp the wave height or wave energy. For the full list of schemes available in SWASH the reader is referred to the user manual. Details on how the schemes are incorporated are given in (Stelling and Duinmeijer, 2003) and (Zijlema and Stelling, 2008).

The pressure term in SWASH is separated in a hydrostatic and a non-hydrostatic part. A solution of the Poisson equation is needed when the non-hydrostatic pressure term is included in the computation. Two linear solvers are incorporated in SWASH to solve the Poisson equation and for details on how SWASH solves the equations, the reader is referred to (Zijlema and Stelling, 2005).

Two different numerical schemes can be used to discretise the vertical pressure gradient, namely the (explicit) central differencing and the (implicit) Keller Box scheme. The Keller Box scheme should be used when the vertical resolution is low and the pressure gradient should be arranged on the interface of the grid (box layout). The combination of the Keller box scheme with the box layout makes the implementation of the zero pressure boundary condition to be very accurate, enhancing the accuracy of the frequency dispersion (Stelling and Zijlema, 2003). For a high vertical resolution, the central differencing with the standard layout is recommended because it is more robust in this case (The SWASH team, 2016).

Time step and grid size restrictions

Because the time integration in SWASH is explicit, the CFL condition restricts the size of the time step (for a given grid size). The way the courant number is defined in SWASH is given in Eq. (3.21). The applied CFL condition is given in Eq. (3.22).

$$C_r = \Delta t\left(\sqrt{gd} + \sqrt{u^2 + v^2}\right)\sqrt{\frac{1}{\Delta x^2} + \frac{1}{\Delta y^2}} \tag{3.21}$$

$$Cr_{min} < Cr < Cr_{max} \tag{3.22}$$

The time step is dynamically adjustable in SWASH, meaning it will update automatically. First, the courant number is calculated over all the wet points and the maximum value is determined. When the courant number becomes larger than a predefined maximum courant number Cr_{max}, then the time step is halved. If the courant number becomes smaller than the set minimum courant number Cr_{min}, then the time step is doubled. A maximum courant number of 0.5 is advised in case of nonlinearities, high waves and wave interactions with steep structures (The SWASH team, 2016).

The SWASH user manual recommends a horizontal grid resolution of at least 51 grid points per wave length in case of low waves (ratio wave height over still water depth small (H/d<<1)) and 101 grid cells for relatively high waves.

The amount of vertical layers depends on the maximum kd value in the computational domain. For two vertical layers, the kd value should be smaller than 2.9 and for three layers the maximum kd value is 16.4 in order to have an error of less than 1% in the normalised wave celerity.

Parallelization

SWASH has the option of using multiple cores or processors for the computations in order to reduce the computational time. The computational domain is divided into a number of subdomains which are strips along the x- or y-axis. Each subdomain is assigned to a different processor, so the number of subdomains depends on the number of processors used. Moreover, each subdomain needs to communicate with its neighbouring sub-domains to get the data needed for the computation, which is called overhead time.

In Figure 3.6 the speed up factor, defined in Eq. (3.15), is shown as the mean of five identical test runs together with plus or minus two standard deviation. The test runs are for scenario C1 of the approach channel case, which is introduced in Section 5.2. No output is requested during the runs, so that only pre-processing and computation time is included.

From the Figure 3.6 it follows that the computation speeds up very fast up till twenty cores. After twenty cores, the speed up factor gradient levels off and from around eighty cores the speed up factor even decreases when more processors are used. This is because the computational grid is subdivided into (too) many sub-domains which need to communicate (overhead time). Consequently, the added speed up by using more cores (because each subdomain has less computational points) is counteracted by the overhead time.

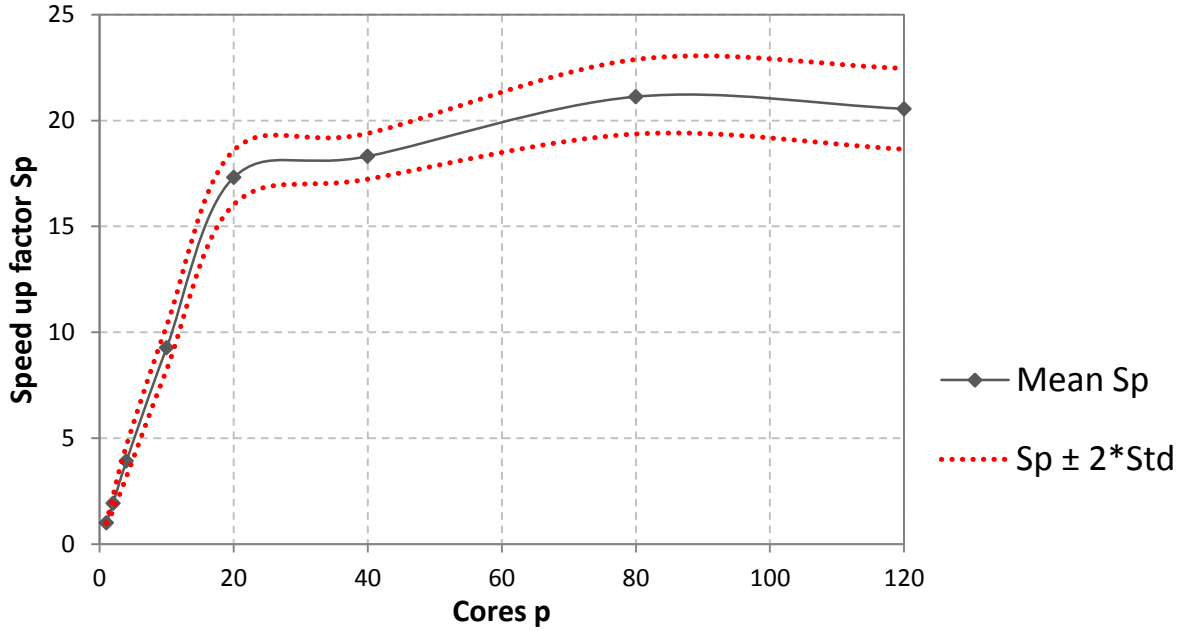

Figure 3.6 Speed up factor as function of the number of cores for scenario C1 of the approach channel with a simulation time of five minutes. Five test runs were performed to compute the mean speed up factor and the standard deviation (Std).

3.2.4 Previous validation

Multiple benchmark tests have been performed with the numerical model SWASH. For a list of examples the reader is referred to the SWASH website (http://swash.sourceforge.net). In the following, a short summary is given of benchmark results and some pervious validation studies performed.

Stelling and Zijlema (2003) and Zijlema and Stelling (2005) tested the model for non-breaking situations with either analytical or experimental data and it was concluded that SWASH can solve the essential wave phenomena such as: shoaling, dispersion, diffraction, refraction and frequency dispersion. Further, Stelling and Duinmeijer (2003) reported a test case which involves flows with steep gradients.

In Zijlema and Stelling (2008) the focus was extended to breaking waves and wave run-up. By comparing numerical results with physical experiment results, it was concluded that the level of agreement is favourable. The initial point of wave breaking is predicted very well when using a fine vertical resolution. For a coarse vertical resolution (1-3 layers), Smit et al. (2013) introduced a hydrostatic front approximation, see Section 3.2.1, and they demonstrated that the energy dissipation by wave breaking can be modelled accurately even with a coarse vertical resolution.

Zijlema et al. (2011) gives eleven more test cases which cover a wide range of wave and flow conditions which are computationally challenging. The performance of the model was satisfactory and SWASH is able to simulate the relevant wave processes involved in complex nearshore environments, including non-linear interactions, wave-breaking, wave run up and wave induced circulations.

Van den Bos et al. (2014) performed a physical experiment and compared the measured reflection and transmission with (amongst others) the values computed by SWASH. It was concluded that the

reflection was measured with an accuracy of 5%, while the transmission was measured with an accuracy of 20%.

Regarding the validation of SWASH for wave penetration studies in ports, a study was performed by Van Vledder and Zijlema (2014), including an example of wave diffraction around a semi-infinite breakwater and for wave penetration into the Lymassol harbour, located in Cyprus. The computed wave heights showed good agreement with the measurements and it was concluded that SWASH can be used as a tool to compute the wave conditions inside harbours or sheltered areas.

Some studies involving approach channels were done previously in SWASH. These studies made use of the same physical experiment also used in this thesis. For more details, see Section 5.2.2.

3.3 Previous comparison studies between MIKE 21bw and SWASH

Two different comparison studies (to the author's knowledge) had been performed which compared the numerical models MIKE 21bw and SWASH. The first one was done by Suzuki et al. (2012) which involved a case study of waves penetrating a shallow marina in Blankenbergen, Belgium. Both numerical model results were compared with field measurements and it was found that both models were able to reproduce the significant wave height with differences in normalised wave heights of 5% for both models.

Another comparison study was performed by De Roo et al. (2015) between the numerical models SWASH, MIKE 21bw and Xbeach. The three models were quantitatively evaluated with field measurement data. The results of MIKE 21bw and SWASH were similar, although the preference was given to the latter model because it turned out to be numerically more robust and therefore easier to use. Another great benefit of SWASH is that it is open source, while MIKE 21bw is a commercial numerical program.

3.4 Conclusions

In this chapter the underlying equations, assumptions, boundary schematisations and previous validation studies are summarized. One of the main theoretical differences is that MIKE 21bw already introduces errors/simplifications in the differential equations by eliminating the vertical coordinate, while SWASH resolves the Reynolds-Averaged Navier Stokes equations. The errors/uncertainties in SWASH are therefore mainly introduced in the discretisation of the equations (numeric), while in MIKE 21bw the errors/uncertainties are introduced in both the differential equations and the numeric. Other differences are primarily found in the boundary schematisations and the different speed up factors which can be obtained in both models. Table 3.1 provides an overview with the main characteristics of both numerical models, i.e. their similarities and differences. With this table, the first research question is answered; what are the theoretical differences between Mike 21bw and SWASH?

From previous validation and comparison studies both models should in principle be able to model wave penetration in ports and access channels accurately.

Another main difference between the two numerical models is that SWASH is open source, and therefore freely available. MIKE 21bw on the other hand is a commercial program and a licence is needed in order to use the program.

Table 3.1. Main characteristics of SWASH and MIKE 21bw.

Characteristic	SWASH	MIKE 21bw
Type	Phase-resolving	Phase-resolving
Equations	Non-linear shallow water equations, including the vertical coordinate	(Enhanced) Boussinesq equations, excluding the vertical coordinate
Grid	Rectangular and curvilinear, resolution computational grid can differ from resolution bathymetric grid	Rectangular, resolution computational grid is the same as the resolution of the bathymetric grid
Rotational flow	Rotational flow	Irrotational flow
Pressure	Hydrostatic as well as non-hydrostatic pressure	Non-hydrostatic pressure is included through adding higher order derivative terms to the non-linear shallow water equations
Vertical structure velocity	Included in the equations, i.e. part of the solution	Imposed on the equations, i.e. not part of the solution
Included processes	Both models include the important wave phenomena which are of interest in the application area of ports and access channels: wave transmission, frequency dispersion, shoaling, refraction, wave breaking, non-linear wave-wave interactions, bottom dissipation, partial reflection and transmission	
Boundary schematisation	Boundaries can either be (almost) fully reflective, partially reflective or (almost) fully dissipating. Sloping boundaries can be modelled in full detail because SWASH does not require a minimum water depth	Boundaries can either be (almost) fully reflective, partially reflective or (almost) fully dissipating. Sloping boundaries cannot be modelled in full detail because a minimum water depth is required to be able to run stable computations
Wave generation	Generation at open boundaries	Generation at open boundaries or at an internal wave generation line
Maximum kd ratio	Maximum kd depends on the amount of vertical layers, for two vertical layers: $kd \leq 7.7$	Maximum $kd \leq 3.1$ (Enhanced Boussinesq equations)
Partial reflection and transmission	To simulate partial reflection or transmission, a porosity value, structure height and stone size needs to be defined. The stone size and the structure height can vary over the domain	Specify porosity values at boundaries where partial transmission and/or reflection is/are required. Further, a constant stone diameter is defined
Wave-current interactions	Build in	Not possible with MIKE 21bw
Wave breaking	Build in and good results when using at least 10-20 vertical layers. If vertical resolution is low (1-3 layers), hydrostatic front approach should be used	Concept of surface rollers (added dissipation model to the Boussinesq equations)
CFL condition	Maximum and minimum Courant number defined. Time step is automatically updated	Maximum Courant number defined which restricts the time step. Time step is fixed
Parallelization	Using domain decomposition. Speed up factor of around 20 can be obtained	Parallelization using shared memory architecture. Maximum speed up factor which can be obtained is 3-4

4 Methodology

Beside an analysis of the theoretical differences between the various models (see Chapter 3), a comparison study was performed between the numerical models making use of two physical experiments. This comparison is used to determine the computational efficiency and consequently, to answer the second research question; what is the computational efficiency of SWASH and MIKE 21bw and what are their boundaries of applicability based on the simulation results of the physical experiments? Moreover, sensitivity analyses were performed by varying certain model parameters to explain the obtained differences in modelling results and thereby aiming to answer the third research question; what causes the differences between the numerical and physical model results and how can they be minimized?

In the next paragraphs the boundaries of applicability considered for this thesis are explained.

4.1 Boundaries of applicability

Numerical models have different boundaries of applicability which (predominantly) depend on what type of application the model is used for. In literature, many authors give boundaries of applicability in terms of a maximum water depth over deep water wave length ratio (h/L_0) for which the phase celerity has a certain error. For example, the best form of the classical Boussinesq equations has a practical deep water limit of $h/L_0 < 0.22$ for which the phase celerity is less than 5% (Madsen and Sørensen, 1992).

For this thesis, the application of the numerical models considered are waves crossing approach channels and penetrating harbours. Moreover, the computational efficiency of the two numerical models is compared. To determine the computational efficiency with respect to the application of the models considered here, the accuracy, computational time and the numerical stability or robustness of the models are evaluated.

The differences between the physical and numerical models are expressed in this thesis as a relative bias in percentages at each wave gauge and is calculated by Eq. (4.1). Furthermore, a mean absolute percentage error (MAPE), see for instance Sutherland et al. (2004), is used which is the sum of the absolute values of the bias at each wave gauge divided by the total number of wave gauges, see Eq. (4.2). The MAPE is always a positive value, while the bias at each wave gauge can be a negative value, which indicates an under-estimation. Vice versa, a positive value indicates an over-estimation.

$$Bias\ (\%) = \left(\frac{f_i}{y_i} - 1\right) * 100 \tag{4.1}$$

$$Mean\ absolute\ percentage\ error\ (\%) = \frac{1}{n}\sum_{i=1}^{n}\left|\left(\frac{f_i}{y_i} - 1\right) * 100\right| \tag{4.2}$$

With: f_i Estimated value numerical model
y_i Estimated value from physical experiment
n Number of wave gauges

The required accuracy for estimating the significant wave heights and mean energy periods in this thesis is considered to be sufficient or 'good' if the bias or MAPE (defined in Eqs. 4.1-4.2) is less than ±15% deviation in the measurements. This value is chosen because requiring a higher accuracy is not realistic or useful for engineering purposes. Furthermore, the discretisation of the differential equations and the schematisations of the boundaries and structures (see also Chapter 3) will always results in some uncertainties. Another reason is that for design studies, the uncertainty of the wave climate and the bathymetry is usually considerable, adding to the total errors in the final result.

More practical issues which, as well as accuracy, determine the computational efficiency are the computational requirements and how robust a model is. The computational requirements include the total computation time, parallelisation aspects and computational cost. The computational cost is defined as the computation time multiplied with the amount of processors used and is evaluated here to not only see how long a computer is running, but also how many processors it is using.

With the robustness of the model it is expressed how easy it is to set up a model and to get it running, without too many numerical instabilities or 'tricks' in order to avoid unwanted numerical instabilities. Computational time is important in the coastal engineering field because projects usually have a set deadline and there is no time to wait for model results for a long time, especially when multiple runs need to be performed. The maximum amount of time a simulation ideally should take is not more than one night.

5 Datasets physical experiments

The two physical experiments which were used for the comparison study are introduced in this chapter. First, the physical experiment performed by Deltares called 'Benchmark tests of wave penetration in harbours' (Van der Ven, 2016) is briefly described followed by the physical experiment of an approach channel performed by Witteveen + Bos together with Deltares (Dusseljee et al., 2014).

5.1 Wave observation set harbour basin

The validation of numerical models with field measurements had been done many times. Common problems with field measurements are that this data is used for commercial ends and is not always freely available or only supplied under strict conditions. Moreover, because the measurements are taken for commercial projects, the lack of knowledge about the measurement accuracy, the boundary conditions and boundaries schematisations can be severe causing it to be less relevant for the validation of numerical models.

Scale model test have the advantage that the imposed conditions can be controlled, on the contrary to field measurements. Further, the accuracy of the measurement devices is better in scale model tests and the imposed conditions and boundary schematisations are well defined. However, such open source scale model tests are rare and therefore Deltares carried out this physical experiment.

The goal of the physical experiment was to produce a benchmark dataset which can be used for the determination of the usability and validity of numerical models for waves penetrating harbours. This dataset is going to be freely available and is purely dedicated for the validation of numerical models.

In this chapter, the scale model test will be introduced with special focus on the relevant aspects for the purpose of this thesis. The model setup including the layout, the measurement locations and the imposed wave conditions are briefly described. The following is a short summary of the measurement report (Van der Ven, 2016) and the reader is referred to this report for more details.

5.1.1 Model setup

For the physical experiments, three different model layouts were used with an increasing basin layout complexity, see Table 5.1. The most complex layout, layout three, consists of a main basin, a breakwater and a secondary basin which is connected under an angle of 45°. This layout yields the highest amount of physical processes and consequently comes closest to simulating processes in a realistic port, i.e. the most representative to a real harbour. The first two layouts govern less physical processes and are more fictitious and can be used to look at some processes individually.

Layout

In Figure 5.1 a top view of the wave basin is presented. The wave basin used is approximately 40 m x 40 m and has an uniform water depth of 0.44 m was used for all the tests. The main basin has dimensions of 8.66 m x 14.53 m and the side basin 3.07 m x 10.49 m. The breakwater is present in layout 3 and is shown in Figure 5.1 in red. It has a length of 4.6 m and a height of 0.7 m. To make sure that the amount of reflected wave energy was limited, a damping slope was constructed at the sides and at the back of the main basin.

Table 5.1. The physical model layouts with their governing wave processes (Van Mierlo, 2014).

(Landward side) Harbour contour Breakwater (Seaward side)	Layout 1	Layout 2	Layout 3
Governing wave processes	Reflection Harbour oscillations	Reflection Diffraction Harbour oscillations	Reflection Diffraction Refraction over the breakwater slope Transmission Harbour oscillations
Eigenmodes	Trivial	Less trivial	Many, increased complexity

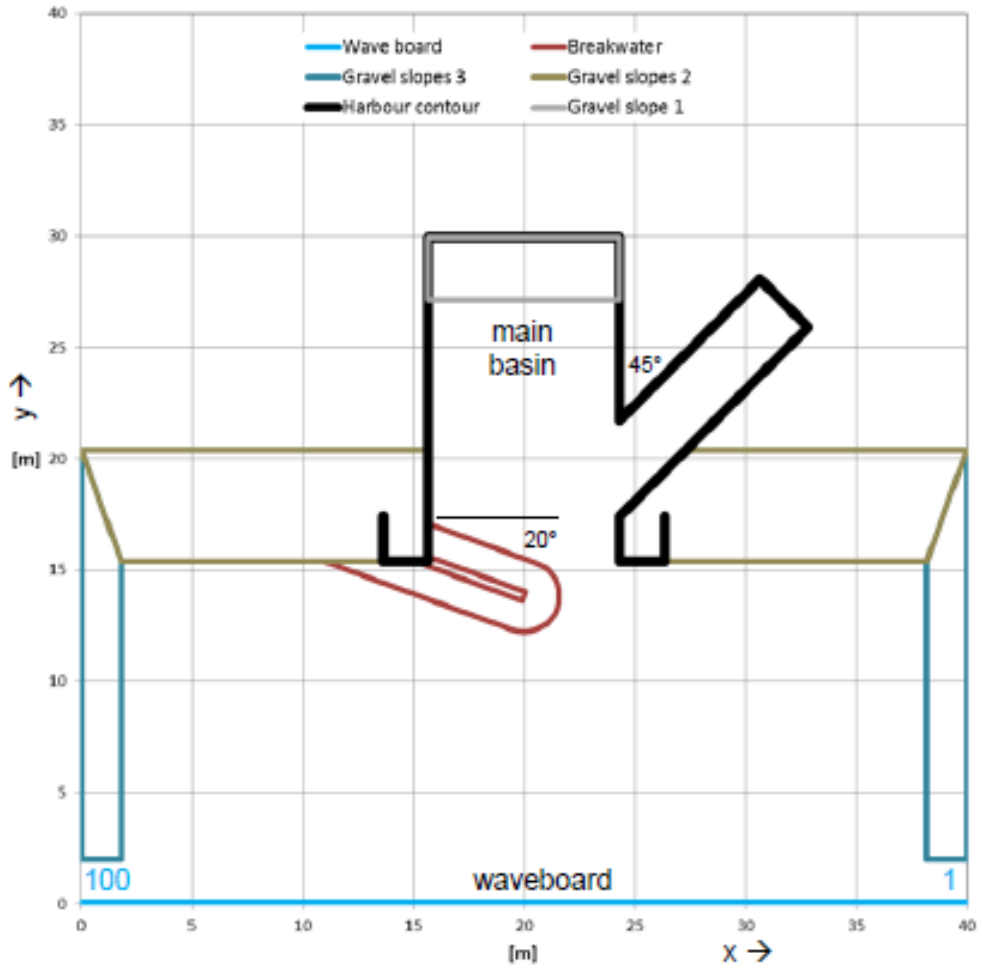

Figure 5.1. Top view of the scale model test (Van Mierlo, 2014).

Measurement locations

Figure 5.2 shows the location of the measurement devices used. The circles represent GHM wave height meters. They have a measuring range of 50 cm and an accuracy of 0.5%. The squares indicate GRSM wave height and direction meters. These devices also measure, beside the wave height, the velocities in x and y direction. The velocity accuracy is around 1%.

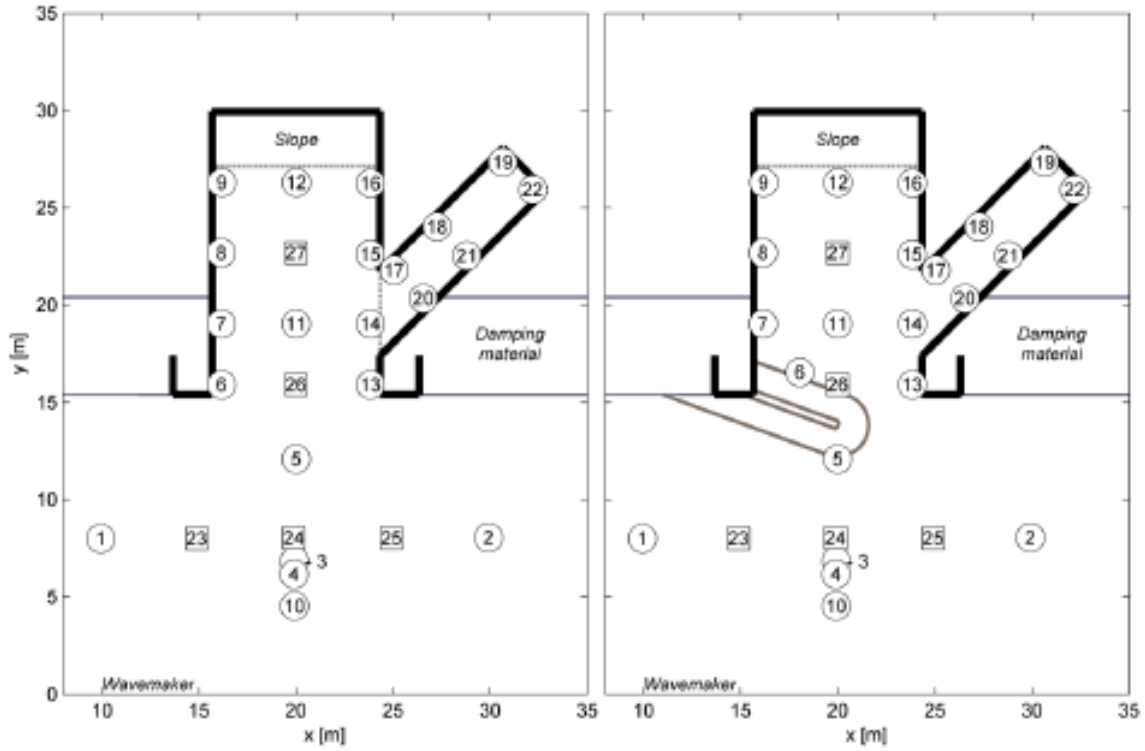

Figure 5.2. Measurement locations for layout 1 and 2 (left panel) and for layout 3 given in the right panel (Van der Ven, 2016).

Imposed wave conditions

The waves are generated by a wave board located at the bottom of Figure 5.1. This wave board consists of 100 paddles which are all 40 cm wide. At both sides of the wave board, the motion of a few paddles had been reduced up to 0% at paddle 1 and 100. In most cases, the motion of the segments 5-96 was 100%.

Second order wave board steering as described by Van Dongeren et al. (2002) was used to avoid the occurrence of spurious wave components in the case of long-crested waves. Further, all the experiments made use of active reflection compensation to prevent wave reflecting at the wave board as much as possible.

During the experiments, the following wave conditions were imposed:

- Monochromatic waves
- Bichromatic waves
- Spectral waves using JONSWAP shape function (with and without directional spreading, i.e. long and short crested waves)
- Sea + swell (this is a combination of a sea state from a certain direction together with a swell from a different direction).

In total 56 different combinations of layouts and wave conditions were simulated. The scenarios used in this thesis are given in Table 5.2. A full list is given in Van der Ven (2016).

Table 5.2. Used scenarios in this thesis.

Scenario	Layout	Type	H_{m0} (m)	T_p (s)	Angle (°)	Directional spreading (°)	Duration (s)
T035	2	JONSWAP (long-crested)	0.106	1.49	90	0	1791
T079	3	JONSWAP (long-crested)	0.106	1.49	90	0	1791

5.1.2 Previously used dataset

Van Mierlo (2014) used the physical experiment to compare the numerical models: PHAROS, TRITON and SWASH. With respect to SWASH, the following conclusions were drawn:

- The wave heights for the primary waves (f > 0.3 Hz) are predicted rather well, with an average error less than 15%. Even for wave heights up to half the water depth.
- The low frequency wave energy (f < 0.3 Hz) is over-estimated by approximately 20%.
- The amplitudes of the harbour oscillations are in some cases predicted with an accuracy of about 20%, but large errors were found in the amplitude of the Helmholtz mode of the side basin, up to an over-estimation of a factor 4.

5.2 Dataset approach channel

The second dataset is for an approach channel towards a harbour for long waves which travel under a relative small angle with the channel access direction. This physical experiment was performed in the 3D wave basin of Deltares together with Witteveen + Bos. Originally, the experiment was meant for a design project of a coastal structure, but due to its relevance for research purposes, it was slightly altered to serve this purpose as well. In this chapter the physical setup together with the imposed wave conditions are briefly described, for the full details see Dusseljee et al. (2014) and Riezebos (2014). Further, previous studies where this physical experiment was used are presented.

5.2.1 Model setup

The model setup of the navigation channel is presented in Figure 5.3. In prototype scale, the channel has a length of 15 km and has a bottom width of 250 m between the two breakwaters and 170 m offshore. Furthermore, the side slopes are 1:5 and the water depth inside the channel is 21.3 m. The water depth offshore is 21.3 m and a slope of 1:10 is used to guide the waves towards the harbour. A scale factor of 1:60 was applied and is Froude scaled to include most wave processes correctly. At the top of the left panel of Figure 5.3, a dissipative beach was installed to prevent wave reflection as much as possible. A bar was placed at the entrance of the approach channel (see right panel of Figure 5.3) to make the wave field inside the channel more realistic, see Riezebos (2014). Two different type of wave gauges were used, i.e. WHM resistant type wave gauges (open circles in the left panel of Figure 5.3) and GRSM directional wave gauges (closed circles in the left panel of Figure 5.3). At the WHM gauges the total wave spectra (including incoming and reflected waves) are provided, while at the GRSM gauges only the incoming wave spectra are known, without any directional information.

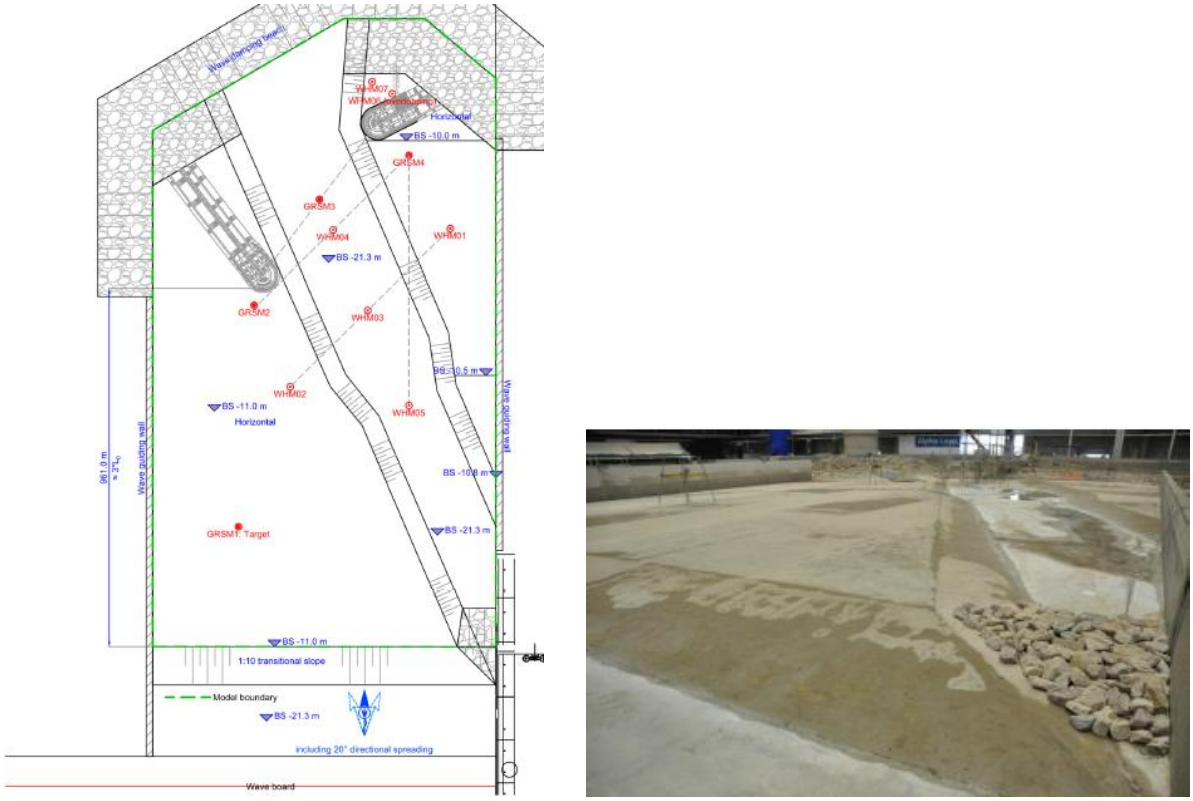

Figure 5.3. Left panel, model setup of the approach channel. The bar built at the beginning of the navigation channel is shown in the right picture (Riezebos, 2014).

Imposed wave conditions

The wave board is located at the bottom of the left panel of Figure 5.3 and made use of active reflection and second-order wave generation. A normal distributed directional spreading as defined by Kuik et al. (1988) with 20° standard deviation was applied. The mean direction of the incident waves has an orientation of 0° normal to the wave board. Moreover, the incident waves make an angle of 23° with the approach channel. Two different wave conditions were imposed: C1 and C2, see Table 5.3. Scenario C1 corresponds to a return period of 1 year, while scenario C2 has a return period of 100 years for the design locations that were considered.

Table 5.3. Imposed wave conditions, after Dusseljee et al. (2014).

Scenario	H_{m0} (m)	T_p (s)	$T_{m-1,0}$ (s)
C1	3	9.7	7.9
C2	4.8	14.1	10.7

5.2.2 Previously used dataset

Dusseljee et al. (2014) performed a study with the numerical models SWASH and SWAN and provided a modelling guideline for navigation channels. They found that SWASH performed reasonably well because it includes evanescent modes and diffraction, on the contrary to SWAN. However, the computational demands are much higher for SWASH compared to SWAN. Further, SWASH was not able to resolve the high frequency part of the spectrum (f > 0.13 Hz). They subscribed this to a grid resolution which was taken to coarse (3 m x 3 m) in order to limit computational cost.

Riezebos (2014) used the physical model to validate SWASH for simulating wave-channel interactions. The following conclusions are given in his report:

- SWASH performs well in simulating low frequency waves (f < 0.13 Hz) for wave-channel interactions, with errors smaller than ±15% inside and across the channel.
- The sponge layer in SWASH is more efficient than the wave spending beaches in the physical model because the amount of reflection in the physical model was quite large. Therefore, a comparison with the WHM gauges which represent the total wave spectra is distorted and an one-on-one comparison is not straight forward.
- At the beginning of the approach channel a bar is present, constructed from stones which are not to scale. This bar is implemented in SWASH as an impermeable bar and deviates from the physical model, hence introducing uncertainties. Though, the exact effect of the sill on the wave pattern inside the channel is unknown.
- The grid resolution of SWASH (3 m x 3 m) is too coarse to correctly represent the high frequency part of the wave spectra (f > 0.13 Hz), therefore leading to an under-prediction of the significant wave height. Upscaling of the spectra does not work because this results in more energy present at the low frequencies and a wrong spectral shape, which is important for wave-channel interactions (see also Section 2.2).

6 Comparison Case 1: approach channel

This chapter presents the results of the numerical simulations of the approach channel (Case 1) at the GRSM wave gauges and the comparison with the physical model test. The comparison here is made for the GRSM gauges because it was concluded by Riezebos (2014) that an one-on-one comparison with the WHM gauges is not straightforward, see also Section 5.2.2.

The comparison is done for the significant wave height (H_{mo}) and energy period ($T_{m-1,0}$) based on the cut-off spectrum which considers frequencies lower than 0.13 Hz. Moreover, this cut-off frequency is identical to the one used by Dusseljee et al. (2014) and was chosen because the computed shape of the spectrum in SWASH above the cut-off frequency differs significantly from the one obtained from the physical model. This cut spectrum is considered here in order to see whether the results from SWASH as presented by Dusseljee et al. (2014) can be reproduced and to extend it to MIKE 21bw.

In addition, to see how the upper frequency part of the computed spectra in SWASH and MIKE 21bw relate to one another, the comparison is done for the significant wave height and energy period based on the total spectra as well.

Due to the kd limit in MIKE 21bw, there is a maximum frequency the model can resolve. This already introduces a bias in the significant wave height and energy period at the wave generation line. Additional tests were performed where the incoming wave spectrum is scaled, i.e. the incoming significant wave height is then identical to the one of the spectrum used in the physical model.

The output of both SWASH and MIKE 21bw at the wave gauges are all exported as time series of water level elevations with a time step of 0.1 second and are post processed with the WAFO toolbox in MATLAB, see Appendix A for details about the toolbox. MIKE 21bw has its own toolbox to process the output, but is not used in order to make sure that no differences arise between the numerical models from the post processing of the results. The errors in this chapter are either given in a bias at a certain wave gauge, as defined in Eq. (4.1) or as a mean absolute percentage error (MAPE) over the four GRSM wave gauges, as defined in Eq. (4.2).

First, in Section 6.1 a brief overview of the setup of both numerical models is presented followed by the comparison with the physical experiment in Section 6.2. Next, in Section 6.3 results of sensitivity analyses are presented regarding the horizontal resolution in SWASH, a scaled incoming wave spectrum and on the influence of wave breaking. The main reason for the sensitivity analyses is to see whether the differences in results found in Section 6.2 can be explained. Finally, the conclusions are presented in Section 6.4.

6.1 Numerical model setup

A brief overview of the numerical setup in MIKE 21bw and SWASH is given below. A more detailed description can be found in Appendix B1 and B2 for MIKE 21bw and SWASH, respectively.

MIKE 21bw settings:

- Horizontal resolution of the computational grid is 3 m x 3 m (46 grid cells per deep water wave length for scenario C1, corresponding to a peak period of 9.7 s).
- Breakwaters do not include slopes and are modelled as vertical (impermeable) walls with 15 porosity layers in front and a fixed porosity value of 0.83. Transmission of the breakwater was not included because it was found that MIKE 21bw computes a (too) large transmission

coefficient given a geometry and (fixed) porosity of the structure, see Appendix C3. Lowering the porosity values in order to get a lower transmission coefficient resulted in numerical instabilities, i.e. blow-ups of the simulations.

- Sponge layers are applied at the top and bottom of the computational domain with a width of 300 meter, corresponding to almost twice the deep water wave length.
- Waves are generated at the wave generation line by imposing the wave spectra which were used during the physical experiment. However, the spectra are cut-off at the maximum frequency (for scenario C1 and C2: T_{min} = 5.32 s; f_{max}= 0.187 Hz) and the resulting truncated spectra under-estimate the significant wave height by 14% and 9% at the wave generation line for scenario C1 and C2, respectively.
- Wave breaking is included for scenario C2 with the concept of surface rollers. The default coefficients were applied and the most important values are: type of roller celerity 3, mean wave direction 0° and an initial breaking angle of 20°.
- Bottom friction is included by means of a Manning number of 0.019 ($m^{-(1/3)}\ s$).
- Time step of 0.05 s is used.
- Equations: use was made of the enhanced Boussinesq equations as described in Madsen et al. (1991).
- Numeric: central differencing with simple upwinding at steep gradients and near land is used for the space discretisation of the convective terms.

SWASH settings:

- An uniform rectangular computational grid in a Cartesian coordinate system is implemented.
- Horizontal resolution of the computational grid is 3 m x 3 m (46 grid cells per deep water wave length for scenario C1, corresponding to a peak period of 9.7 seconds).
- Two vertical layers of equal thickness.
- The breakwaters are modelled as porous structures. A porosity value of 0.45 was applied and the stone size and structure height vary over the cross section and consequently, the slope of the breakwater is included. The stone diameter is 0.65 m at the beginning of the slope and gradually decreases towards 0.2 m located at the crest of the breakwater.
- Waves are generated at the Southern boundary by imposing the spectra which were also used during the physical experiment. The incident waves have a mean wave direction of 0° normal to the wave board. Further, a normal distributed directional spreading with 20° standard deviation was applied.
- Wave breaking: the hydrostatic front approach is used (using default parameters) to model wave breaking because of a coarse vertical resolution (2 vertical layers).
- Bottom friction is included by means of a Manning number of 0.019 ($m^{-(1/3)}\ s$).
- Time step of 0.025 s is used.
- Numeric: Keller box scheme is applied together with the default momentum conservative schemes, which are a central differencing scheme for the horizontal advection terms and an upwind scheme for the vertical advection terms.

6.2 Results

In Figure 6.1 the spatial distribution of the significant wave height (H_{m0}) as computed by SWASH and MIKE 21bw is presented based on the total frequency spectra. It can be seen that SWASH and MIKE 21bw show similar patterns regarding the spatial distribution of the significant wave height.

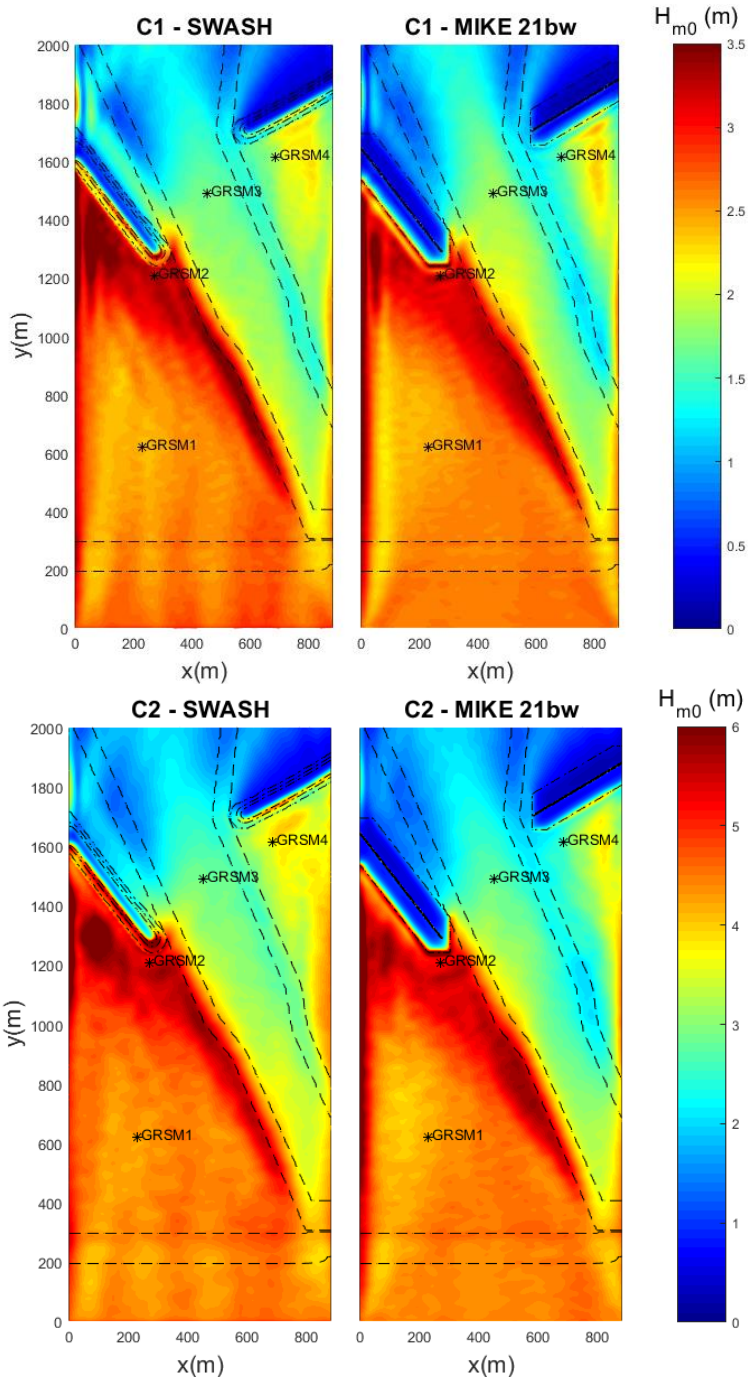

Figure 6.1. Spatial distribution of the significant wave height as computed by SWASH (left) and MIKE 21bw (right) over the computational domain for scenario C1 (top figures) and scenario C2 (bottom figures).

The energy focussing along the wave-ward side of the channel (left side of the channel, GRSM1 and GRSM2 are located here) can be seen for the scenarios in both models. This wave attenuation is mainly due to wave refraction and reflection by the navigation channel and causes wave energy to focus along the channel which results in an increase in wave height. For scenario C2, this increase in wave height along the wave-ward side of the channel caused severe wave breaking to occur. The significant wave height computed by MIKE 21bw for this scenario along the wave-ward side of the channel is slightly larger than computed in SWASH. Inside the channel the significant wave height is lower than the incoming significant wave height because part of the wave energy is not able to cross the channel due to an angle of approach which is larger than the critical angle, see Section 2.2. This

effect can be seen in both numerical model results. At the lee-ward side of the channel (at location GRSM4) the significant wave height increases again due to the decrease in water depth and because of reflections of the breakwater and wave guiding walls. Furthermore, the computed wave height by SWASH at the lee-side of the channel is larger than in MIKE 21bw, in particular for scenario C2. Another noticeable difference between the two numerical model results is the computed significant wave height behind the breakwaters. The estimates of MIKE 21bw are significantly lower than the computed values in SWASH. This is because in MIKE 21bw the breakwaters are modelled as impermeable structures while the breakwaters in SWASH have some transmission.

Accuracy

Figure 6.2 shows the results of the inter comparison of the two numerical model results for both wave conditions (scenario C1 and C2) considered at the GRSM gauges (locations can be seen in Figure 6.1). The results are presented in terms of significant wave height and energy period based on the cut-off and total frequency spectrum. In addition, bars showing a fixed measurement deviation of ±15% are plotted. Estimations within this deviation in measurement are considered to be good, see also Section 4.1. Figure 6.3 presents the frequency spectra at the GRSM wave gauges for scenario C2. All the estimated wave spectra for scenario C1 and C2 can be found in Appendix B3.

By looking at the shapes of the frequency spectra measured at the wave gauges, it can be seen that SWASH reproduces the spectral shape accurately for frequencies lower than 0.13 Hz as was also found by Dusseljee et al. (2014). Further, the upper part of the spectrum is not well computed and shows a clear under-estimation. The spectral shape computed by MIKE 21bw shows a similar trend and is very well reproduced for frequencies lower than 0.13 Hz. However, the upper part of the spectrum also shows an under-estimation and the maximum resolved frequency can clearly be seen, i.e. there is no energy present at frequencies higher than the maximum frequency. Noticeable is that the computed spectrum by MIKE 21bw at GRSM2 for scenario C2 shows a clear over-estimation at the second peak which is due to an under-estimation of wave breaking, see also Section 6.3. Further, MIKE 21bw under-estimates the spectrum at GRSM4 more than SWASH.

The comparison of the significant wave heights and energy periods based on the cut-off spectra ($f < 0.13$ Hz) show that both SWASH and MIKE 21bw perform well and similar. For SWASH, the MAPE in significant wave height is 8% and 6% for scenario C1 and C2, respectively. The MAPE in energy period is 2% for scenario C1 and 3% for scenario C2. The significant wave height as computed by MIKE 21bw show a MAPE of 10% and 14% for scenario C1 and C2, respectively, and a MAPE in energy period of 3% for scenario C1 and 4% for scenario C2.

The computed significant wave heights by the two numerical models based on the total frequency spectra show an under-estimation in both numerical models. The MAPE of the numerical models are very similar and are for scenario C1 21%, for both SWASH and MIKE 21bw. For scenario C2, the MAPE in SWASH is 12% and in MIKE 21bw 16%.

The energy periods based on frequencies larger than 0.13 Hz are over-estimated in both models. SWASH has a MAPE of 11% and 8% for scenario C1 and C2, respectively. MIKE 21bw has a MAPE of 14% and 12% for scenario C1 and C2, respectively. The over-estimation of both models indicates that there is a lack of high frequency energy which can also be seen from the computed frequency spectra.

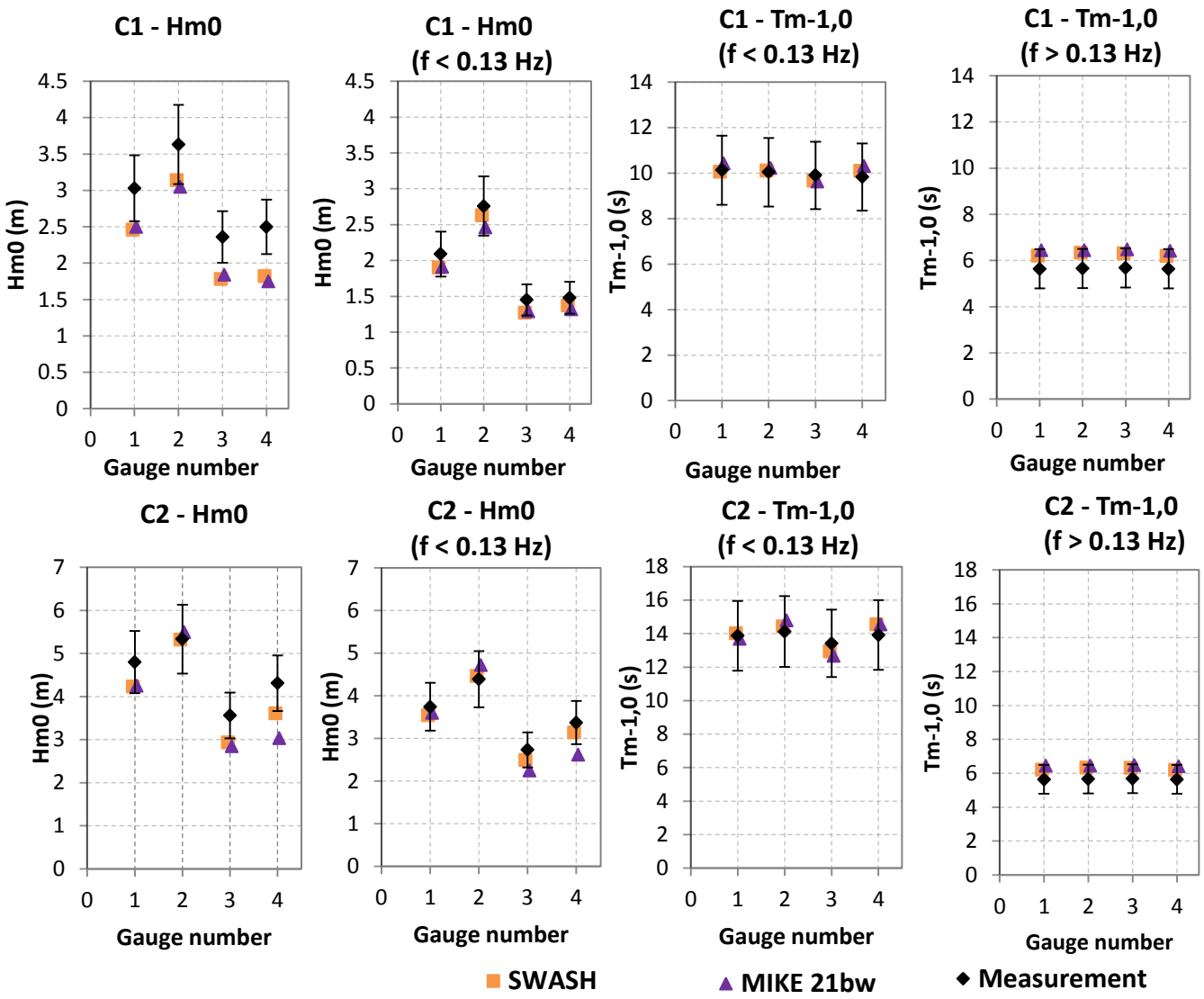

Figure 6.2. Computed significant wave height (Hm0) and energy period (Tm-1,0) based on the total and cut-off spectra at the GRSM wave gauges. The scenarios C1 and C2 are presented in the top and bottom figures, respectively. Note that the bars indicate a (fixed) measurement deviation of ±15%.

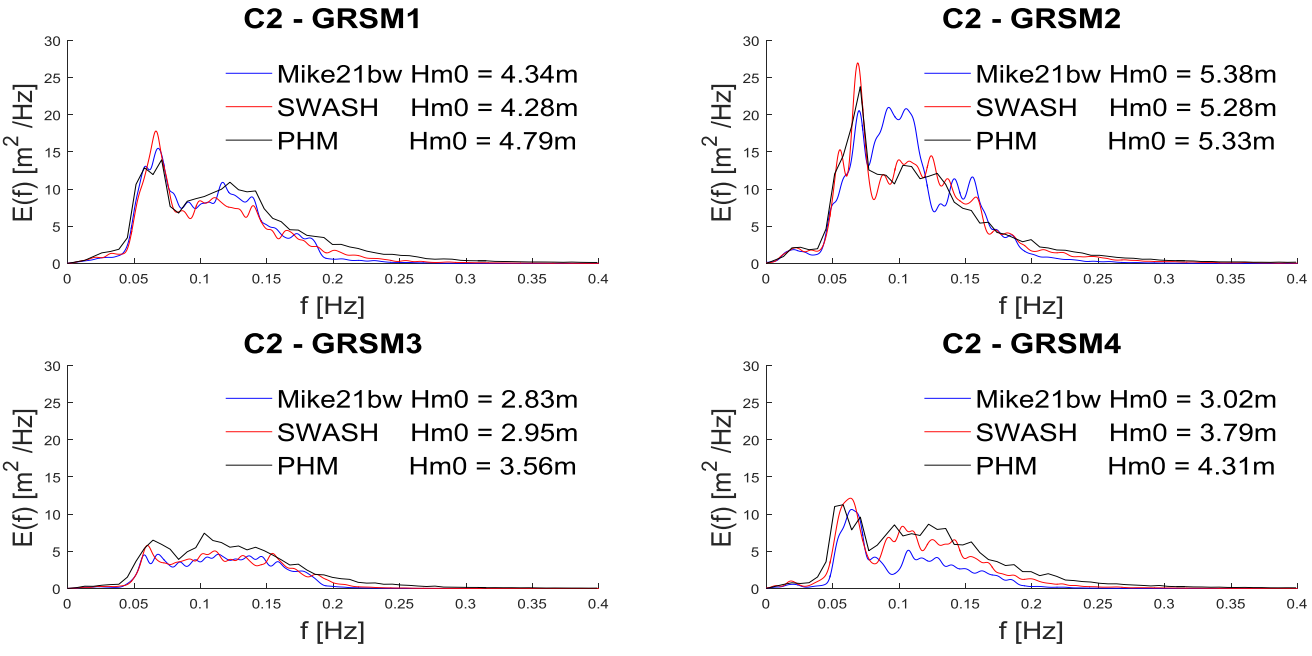

Figure 6.3. Estimated frequency spectra at the GRSM gauges for scenario C2.

Computation time

The parallelisation aspect of both models was already treated in Section 3.1.3 and 3.2.3 for MIKE 21bw and SWASH, respectively. It followed that the speed up factor which can be obtained in SWASH is around 20, while for MIKE 21bw the maximum speed up factor is around 4. Therefore, it is more beneficial to use more processors in SWASH than in MIKE 21bw.

In order to compare the computation time, additional runs had been performed on the same computer (with six processors) based on scenario C1. The total elapsed time is compared together with the computational cost which is defined as the amount of processors multiplied with the elapsed time. The simulation time was reduced to 15 minutes and no output was requested for both models to make sure the post-processing time is minimal and the comparison is mainly for the computation time (pre-processing time is included, but is very small compared to the computation time). The amount of computational cells is larger in MIKE 21bw because the model domain was extended so that a sponge layer can be placed behind the wave generation line.

The results are presented in Table 6.1. From this table it follows that the computational cost per computational grid cell per time step is a factor 10 lower for MIKE 21bw than for SWASH, when two vertical layers are used.

A run with SWASH using only one vertical layer was performed as well. The computational cost for SWASH using one vertical layer is (almost) identical to MIKE 21bw. However, the predictions of the significant wave height, expressed in a mean average percentage error, are 5% worse (13% when using one vertical layer, 8% when using two vertical layers).

Table 6.1. Comparison of the computational time and computational cost between MIKE 21bw and SWASH. Both computations are carried out on an Intel (R) Xeon(R) CPU W3690 @ 3.47 GHz on a 64-bit operating system.

	MIKE 21bw	SWASH (2 layers)	SWASH (1 layer)
Horizontal resolution computational grid (m)	3	3	3
Amount of vertical layers	-	2	1
Computational cells	365,161	245,600	245,600
Total simulation time (s)	900	900	900
Time step (s)	0.05	0.05	0.05
Amount of time steps	18,000	18,000	18,000
Processors used	6	6	6
Elapsed time (hours)	0.31	2.47	0.25
Computational cost (Elapsed time (s) * processors)	6,696	53,352	5,400
Computational cost per computational grid cell	0.02	0.22	0.02
Computational cost per computational grid cell per time step	1.02E-06	1.21E-05	1.22E-06

Stability

The stability or robustness of both numerical models was comparable and not many critical numerical instabilities occurred during the modelling. A main reason for this is because there are not many structures or internal boundaries present in the model where numerical instabilities may occur. Only the slopes of the breakwaters in MIKE 21bw were not taken into account because including these slopes resulted in numerical instabilities which terminate model runs.

6.3 Sensitivity analyses

Numerical damping

In Dusseljee et al. (2014) and Riezebos (2014) it was concluded that the high frequency wave energy dampens out over the first few grid cells (for a horizontal resolution of 3 m x 3 m). To confirm this, an additional SWASH run had been performed without the breakwaters. The results are presented in the left panel of Figure of 6.4. It can clearly be seen that the high frequency part of the spectrum significantly dampens over the first 200 meter in SWASH.

The same run was performed in MIKE 21bw (excluding the breakwaters) and the results are presented in the right panel of Figure of 6.4. These result show that the numerical damping in MIKE 21bw is almost negligible over the first 200 meter (by comparing the spectrum at y = 200 m with the spectrum obtained at y = 001 m). The difference in numerical damping between the two models is due to different discretisation methods which both models use for mainly the convective terms, where most numerical dissipation occurs.

An additional SWASH run was done with the central differencing scheme for the discretisation of the vertical advection term of u- and v- momentum instead of upwinding. This however resulted in critical numerical instabilities and was therefore not used any further.

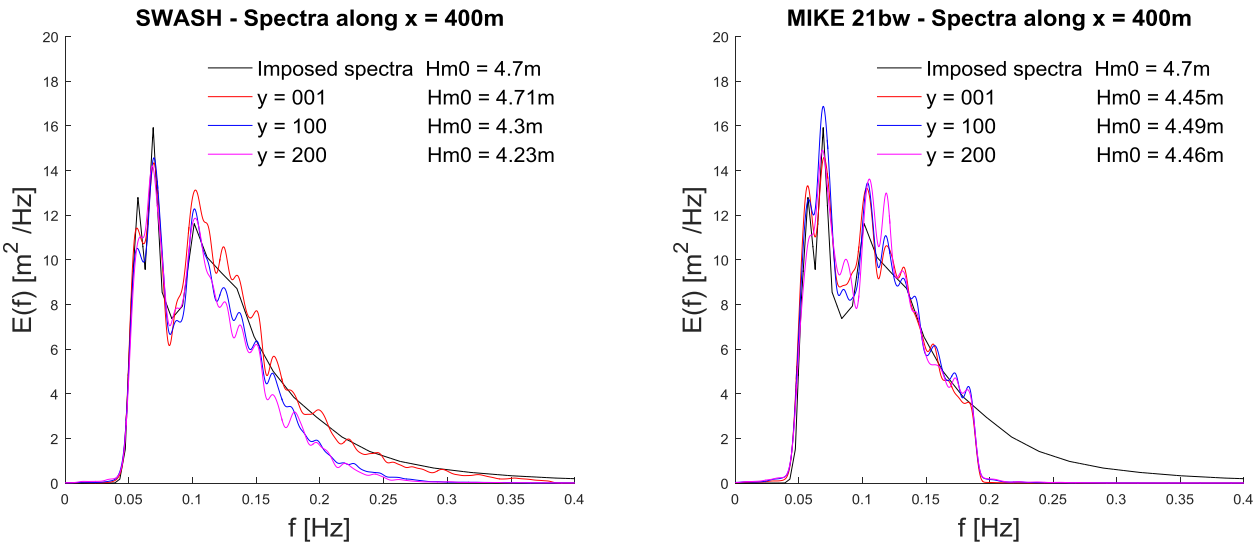

Figure 6.4. Estimated frequency spectra at multiple y-coordinates at x-coordinate of 400 m. The left figure presents the results for SWASH and the right figure for MIKE 21bw.

Varying horizontal resolution SWASH

In order to see if numerical damping in SWASH is the reason why the significant wave height based on the total wave spectrum is under-estimated, two additional runs were performed in SWASH with different horizontal resolutions.

Figure 6.5 shows the computed frequency spectra including the significant wave height at wave gauge GRSM1 for both scenario C1 and C2. It can be seen that the computed significant wave height improves by refining the horizontal resolution from 5 m to 3 m, but to a lesser extend from 3 m to 1.5 m. Further, the finest horizontal resolution (1.5 m) still shows an error compared to the physical model. This indicates that numerical damping cannot (fully) explain the under-prediction observed at the wave gauges.

Furthermore, MIKE 21bw shows over the first 200 m almost no numerical damping (see Figure 6.4) and also under-estimates the significant wave height at the wave gauges inside and at the lee-side of the channel (bias of -22% and -30% at wave gauges GRSM3 and GRSM4 for scenario C1) which is larger than the -14% bias introduced at the wave generation line. This gives more confidence in the fact that numerical damping is not the (only) reason for the under-estimation in SWASH.

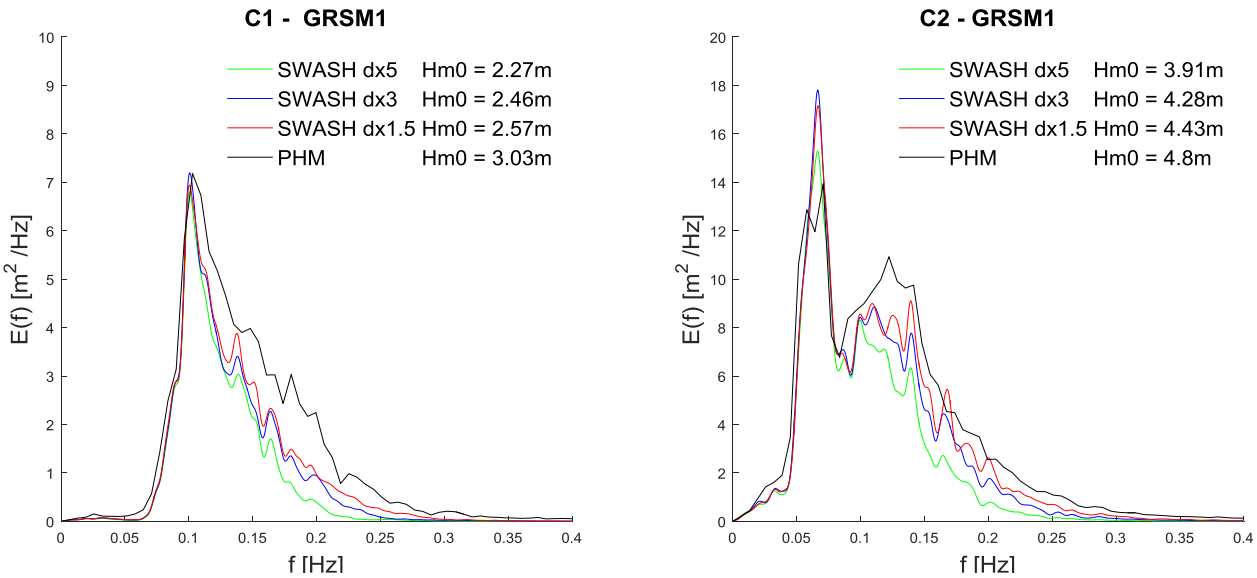

Figure 6.5. Estimated frequency spectra at GRSM1 computed by SWASH for scenario C1 and C2 using three different horizontal resolutions. Note that dx is equal to dy.

Wave breaking

The frequency spectrum computed by MIKE 21bw for scenario C2 at wave gauge GRSM2 shows an over-estimation at the second peak, compared to SWASH and the physical experiment. This is because wave breaking is under-estimated. To illustrate this, a SWASH run was performed for scenario C2 without using the hydrostatic front approach to model wave breaking.

Although SWASH always accounts for wave breaking, it had been shown before by Smit et al. (2013) that SWASH under-predicts energy dissipation by wave breaking largely when using a coarse vertical resolution, which is the case in these model runs (2 vertical layers).

The SWASH results are shown in Figure 6.6. From this graph it can be seen that when wave breaking is not taken into account properly, the second as well as the first peak are over-estimated. In addition, the second peak looks very similar to the obtained results of MIKE 21bw in Figure 6.3 at GRSM2. This result gives confidence in the fact that the over-estimation of the second peak is due to an under-estimation of wave breaking in MIKE 21bw.

It was not possible to calibrate wave breaking in MIKE 21bw in the allotted time. However, it is believed that when using a finer horizontal resolution and after calibration, wave breaking will be predicted much better because good results have been presented before by for instance Madsen et al. (1997a).

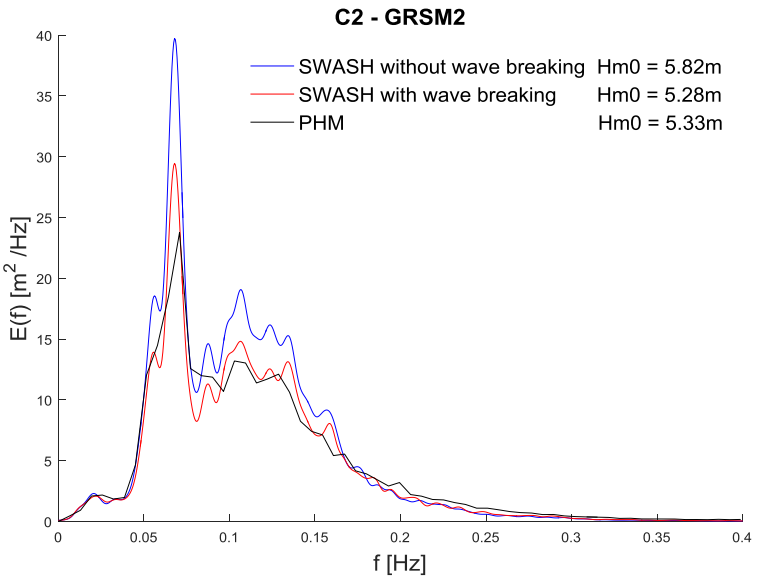

Figure 6.6. Estimated frequency spectra at gauge GRSM2 for scenario C2. The red line indicates a SWASH run including the hydrostatic front approach used to model energy dissipation due to wave breaking, while the blue line is for a SWASH run without the hydrostatic front approach.

Scaled incoming wave spectrum in MIKE 21bw

The wave generation in MIKE 21bw for scenario C1 already under-estimates the significant wave height by 14% at the wave generation line due to the kd limit. A MIKE 21bw run was performed with an up-scaled spectrum so that the incoming significant wave height is correct, i.e. has the same significant wave height as the original spectrum. The up-scaled spectrum is shown in Figure 6.7 in blue. It can be seen that the incoming wave height is now correct, but the spectral shape is not predicted correctly.

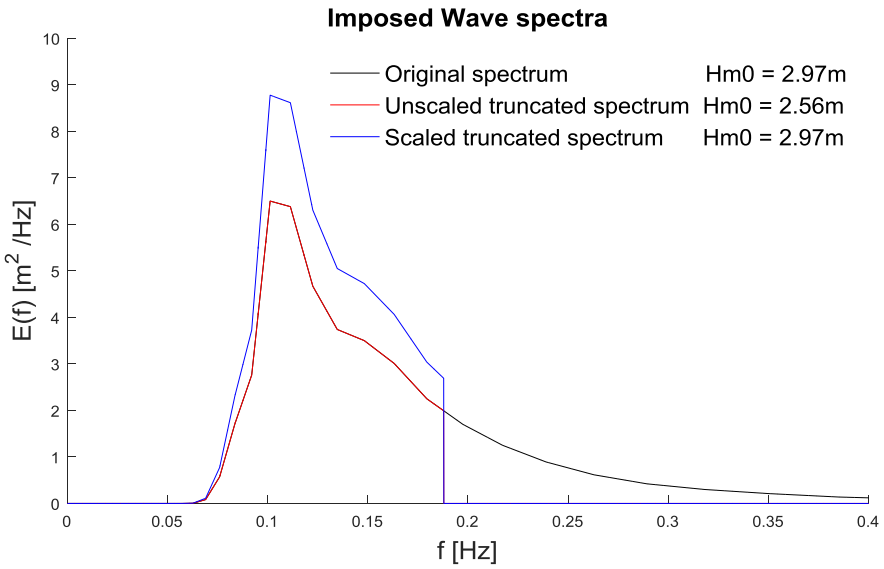

Figure 6.7. The estimated wave spectra as used in the physical experiment (black), the unscaled spectrum in MIKE 21bw (red) and the scaled spectrum (blue) in MIKE 21bw, at the wave generation line for scenario C1. Note that part of the black line and the red line overlap.

The results of the simulations based on the scaled and the unscaled spectrum for scenario C1 in MIKE 21bw are presented in Table 6.2. From this table it can be seen that the computed significant wave heights from the wave gauges at the wave-ward side (GRSM1 and GRSM2) of the channel increase by 14% or more and that the bias at the wave gauges is low (±3%). The predictions inside the channel (GRSM3) and at the lee-side (GRSM4) do improve, but not as much as the estimates at the wave gauges at the wave-ward side of the channel. Moreover, they still show a large under-estimation.

The reason why upscaling the incoming wave spectrum only partially works is because reproducing the shape of the spectrum is very important due to the fact that different frequencies have different critical angles, see Section 2.2. By upscaling the spectrum, the energy which is present at the upper part of the spectrum is shifted towards the lower part of the spectrum to make sure the incoming significant wave height is correct. Lower frequencies have a lower critical angle and therefore the shifted wave energy due to the up-scaling of the spectrum is less likely to cross the channel and will focus along the wave-ward side of the channel. This can be seen from the computed values in Table 6.2. At the wave-ward side of the channel, at GRSM2, the computed significant wave height is 18% larger for the scaled spectrum compared to the unscaled spectrum while at the lee-side of the channel, at GRSM4, the significant wave height is only 9% larger even though the incoming wave height was increased by 14%.

Table 6.2. Computed significant wave height for the simulations with the unscaled and scaled spectrum at the wave generation line for scenario C1 in MIKE 21bw. Note that the difference in bias is the bias of the scaled spectrum minus the bias of the unscaled spectrum simulation.

Gauges	Measurement	Unscaled spectra		Scaled spectra		Difference Bias (%)
	Hm0 (m)	Hm0 (m)	Bias (%)	Hm0 (m)	Bias (%)	
GRSM1	3.03	2.52	-17	2.93	-3	14
GRSM2	3.63	3.09	-15	3.75	3	18
GRSM3	2.36	1.84	-22	2.06	-13	9
GRSM4	2.5	1.62	-35	1.85	-26	9

6.4 Discussion and conclusions

The results of the comparison study presented in Section 6.2 show that:

- The spatial variation of significant wave heights in SWASH and MIKE 21bw show very similar patterns. However, MIKE 21bw over-estimates the significant wave height at the wave-ward side of the channel and under-estimates the significant wave height at the lee-side of the channel for scenario C2 more than SWASH, i.e. SWASH is slightly more accurate.
- The spectral shape at the GRSM wave gauges is well represented by SWASH and MIKE 21bw for frequencies lower than 0.13 Hz. For higher frequencies both models show an under-estimation.
- SWASH and MIKE 21bw perform very well in predicting the significant wave height for frequencies lower than 0.13 Hz. The mean average percentage errors of the significant wave height are 8% and 6% in SWASH for scenario C1 and C2, respectively. Further, MIKE 21bw shows mean average percentage errors of 10% for scenario C1 and 14% for scenario C2. Moreover, the accuracy of both models is comparable. All the errors lie within the ±15% deviation in the measurements and therefore, the performance is considered to be good.
- The energy periods based on the cut-off spectrum are also predicted well with mean average percentage errors of 2% and 3% in SWASH and MIKE 21bw, respectively, for scenario C1. The mean average percentage errors for scenario C2 are 3% and 4% for SWASH and MIKE 21bw, respectively.
- The numerical models perform relatively poor in estimating the significant wave height based on the total wave spectra with a mean average percentage error of 21% in SWASH and MIKE 21bw for scenario C1. The mean average percentage errors for scenario C2 are 12% in SWASH and 16% in MIKE 21bw. Moreover, the significant wave heights are under-estimated.
- The energy period based on the upper part of the spectrum ($f > 0.13$ Hz) is over-estimated in both numerical models because contributions in the upper part of the spectrum are omitted. The mean average percentage errors are 11% and 14% in SWASH and MIKE 21bw for scenario C1, respectively. For scenario C2 the mean average percentage errors are 8% and 12% for SWASH and MIKE 21bw, respectively. The performance of the numerical models is still considered to be good because the bias at each wave gauge is less than ±15% deviation in the measurements.
- The computational time for MIKE 21bw is a factor 10 faster than SWASH (using two vertical layers) when simulating on 6 processors. This factor gets larger when less processors are used and gets smaller when more processors are used due to the different speed up factors in SWASH and MIKE 21bw.
- The computational cost for SWASH, using one vertical layer, is (almost) identical to MIKE 21bw. However, for scenario C1, the mean average percentage error in significant wave height becomes 13% when using one vertical layer (was 8% for two vertical layers).
- The stability or robustness is comparable in this case and not many critical numerical instabilities were encountered. This is mainly because not many structures or internal boundaries are present.

The sensitivity analyses of Section 6.3 show that:

- SWASH has more numerical damping than MIKE 21bw when using a horizontal grid size of 3 m x 3 m with the used discretisation schemes which lead to stable results. However, MIKE 21bw does not include the high frequency part of the spectrum at all.
- The under-estimation of the significant wave height cannot be (fully) explained by numerical damping, i.e. using a finer horizontal resolution in SWASH does not lead to significant better results. Moreover, MIKE 21bw shows almost no numerical damping and also shows an under-estimation which is significantly larger than the -14% bias introduced at the wave generation line. This gives more confidence in the fact that numerical damping is not the main reason for the under-estimation in SWASH as suggested by Dusseljee et al. (2014) and Riezebos (2014).
- The over-estimation of MIKE 21bw at the wave-ward side of the channel, including wave gauge GRSM2, is due to an under-estimation of wave breaking when using the default breaking parameters and a horizontal resolution of 3 m x 3 m.
- Upscaling the incoming wave spectrum at the wave generation line to make sure that the incoming wave height is correct only partially works because it comes at the expense of the spectral shape. This is in agreement with the results obtained by Riezebos (2014) from upscaling the frequency spectra in SWASH.

Because both numerical models show an under-estimation of the significant wave height based on the total spectra and this cannot be (fully) explained by numerical damping, it is possible that an error is made in the schematisation of the physical experiment in the two numerical models. In addition, the conclusions regarding the model observations given by Riezebos (2014) (also provided in Section 5.2.2) about the relative high reflection of the energy dissipating beach and the bar implementation at the entrance channel with stones which are not to scale, introduce uncertainties on how the physical model setup should be schematised in the numerical models.

Another reason could be inaccuracies in the measurements of the physical experiment. The GRSM wave gauges provided the incoming wave spectra while at the WHM gauges the total wave spectra were given. The raw data was not available for this thesis and therefore the post processing of the raw data could not be checked.

7 Comparison Case 2: harbour

This chapter presents the results of the numerical simulations of the harbour case (Case 2) which was introduced in Section 5.1 for the scenarios T035 and T079, which exclude and include the breakwater, respectively. The simulations were performed in physical model scale and are identical to the scale of the physical experiment to avoid scale effects. However, due to some numerical instabilities, which are explained in Section 7.2, the simulations were also carried out on a prototype scale, Froude scaled at scale 1:20. At scale 1:20, length scales are scaled with a factor 20, time is scaled with the square root of 20 and the frequencies are scaled with a factor $\frac{1}{\sqrt{20}}$, see also Table 2.1 for the multiplication factors of some physical parameters when Froude scaling is applied.

The comparison is made for the significant wave height (H_{m0}) and energy period ($T_{m-1,0}$) based on the low frequency and upper frequency part of the spectra. In the latter, the upper frequency part is referred to as primary wave energy. Frequencies lower than 0.3 Hz and 0.067 Hz are considered low frequency energy for physical model and prototype scale, respectively. The reason these frequencies were chosen is because the wave spectra shows a clear distinction between the primary and low frequency wave energy. Furthermore, the separating frequency of 0.3 Hz (physical model scale) is identical to the one used by Van Mierlo (2014). In this way, it can be checked whether his obtained results in SWASH can be reproduced.

Beside the comparison of wave parameters based on the primary and low frequency energy, two different long period oscillations, i.e. the amplitude of the Helmholtz mode of the main and side basin are compared. The amplitude of the Helmholtz mode is obtained by integrating a narrow frequency range of the wave spectra. Moreover, the frequency ranges used are identical to the ones used by Van Mierlo (2014) as well.

The errors in this chapter are either given in a bias at a certain wave gauge, as defined in Eq. (4.1) or as a mean average percentage error (MAPE) over the 27 wave gauges, as defined in Eq. (4.2).

As for the approach channel (Case 1), the output of all the wave gauges was exported as time series of water level elevations in meters. Moreover, the output is saved with a time step of 0.025 seconds, which is identical to the time step the output of the physical experiment is saved. The post processing of the output of the physical experiment and the numerical models was done with the WAFO- toolbox in MATLAB. For details about the toolbox see Appendix A.

First, in Section 7.1 the numerical setup of both models is briefly described followed by a selection of results from the simulations performed in physical model scale and the encountered numerical instabilities in Section 7.2. Next, in Section 7.3 the results of the comparison based on the simulations performed on prototype scale are presented, including a discussion on accuracy and stability. This chapter is concluded by a discussion and conclusions presented in Section 7.4.

7.1 Numerical model setup

A brief overview of the numerical setup in MIKE 21bw and SWASH is given below. A more detailed description can be found in Appendix C1 and C2 for MIKE 21bw and SWASH, respectively.

MIKE 21bw settings:

- Simulations were carried out on physical model scale which is identical to the scale used in the physical experiment and on a prototype scale, which is Froude scaled at scale 1:20.
- Horizontal resolution of the computational grid is 0.07 m x 0.07 m and 1.4 m x 1.4 m for physical model scale and prototype scale, respectively (39 grid cells per wave length corresponding to the peak periods of 1.49 s and 6.66 s for physical model and prototype scale, respectively). Note that the amount of grid cells of the computational domain is identical in both scales.
- The reflection coefficients (in terms of wave height) assigned to the different boundaries are
- taken from Van Mierlo (2014) and are:
    - Breakwater: 0.3
    - Gravel slopes: 0.2
    - Vertical concreate wall: 1

  The reflection coefficient of 1 for the vertical concrete walls resulted in numerical instabilities in physical model scale (see Section 7.2) and therefore a reflection coefficient of 0.9 was used.
- The breakwater and gravel slopes are modelled as vertical (impermeable) walls with porosity layers in front. The porosity values assigned are calculated with the MIKE 21bw toolbox to get the desired reflection coefficients. Runs including transmission of the breakwater had been performed as well, but this resulted in a large over-estimation of the significant wave height inside the harbour due to a transmission coefficient which was too large. Lower porosity values which would lead to a lower transmission coefficient could not be used because this resulted in numerical instabilities. For the full details on the schematisation of the breakwater, see Appendix C3.
- A sponge layer is applied behind the wave generation line in order to dampen the reflected waves and it has a width of 50 grid cells (model domain has been extended by this width) corresponding to almost twice the wave length based on the peak periods of 1.49 s (physical model scale) and 6.66 s (prototype scale).
- Waves are generated by imposing time series of surface elevation at the wave generation line. These time series were calculated from the motions of the wave board used in the physical experiment. By imposing these time series the same realisation of the JONSWAP spectrum in the physical and numerical model is obtained. No directional spreading is applied and the orientation of the incoming waves is normal to the wave generation line.
- Wave breaking is not included because the generated waves are far away from the breaker limit and it enhances numerical stability.
- No bottom friction is included, because the distance over which the waves travel is relatively small and therefore the effect of bottom friction is very small.
- Time steps of 0.005 s and 0.02 s were used for physical model and prototype, respectively.
- Equations: use was made of the enhanced Boussinesq equations as described in Madsen et al. (1991a).

- Numeric: Central differencing with simple upwinding at steep gradients and near land is used for the space discretisation of the convective terms.

SWASH settings:

- An uniform rectangular computational grid in a Cartesian coordinate system is implemented for both model scale and prototype scale (Froude scaled with a scale of 1:20).
- Horizontal resolution of the computational grid is 0.07 m x 0.07 m and 1.4 m x 1.4 m for physical model scale and prototype scale, respectively (39 grid cells per wave length corresponding to both the peak period of 1.49 s and 6.66 s for physical model and prototype scale, respectively). Note that the amount of grid cells of the computational domain is identical in both scales.
- Two vertical layers of equal thickness.
- The breakwater, vertical walls and gravel slopes are modelled as porous structures with a porosity of 0.4 for the breakwater and gravel slopes and 0.001 for the vertical concrete walls. A stone size of 150 mm, 30 mm and 1 mm was used for the gravel slopes, the breakwater and the vertical concrete walls, respectively.
- Waves are generated by imposing time series of the surface elevation at the Southern boundary. These time series were calculated from the motions of the wave board used in the physical experiment. By imposing these time series the same realisation of the JONSWAP spectrum in the physical and numerical model is obtained. No directional spreading is applied and the orientation of the incoming waves is normal to the wave generation line.
- Wave breaking: hydrostatic-front approach was not used because no significant wave breaking occurred during the physical experiment.
- No bottom friction is included, because the distance over which the waves travel is relatively small and therefore the effect of bottom friction is very small.
- Time steps of 0.005 s and 0.02 s were used for physical model and prototype scale, respectively.
- Numeric: Keller box scheme is applied together with the default momentum conservative schemes, which are a central differencing scheme for the horizontal advection terms and an upwind scheme for the vertical advection terms.

7.2 Results simulation physical model scale

A selection of results for scenario T079 simulated in physical model scale are presented in this section. For all the results of scenario T035 and T079, on physical model scale, see Appendix C4 and C5. The spatial variation of the significant wave height as computed by MIKE 21bw and SWASH is presented in Figure 7.1. It can be seen that there are some striking differences between the two numerical models. SWASH shows a strange symmetrical pattern in front of the breakwater. Inside this symmetrical pattern the computed significant wave height is lower than the incoming significant wave height. Another noticeable difference is that the computed significant wave height in MIKE 21bw in the shadow zone behind the breakwater is larger than in SWASH.

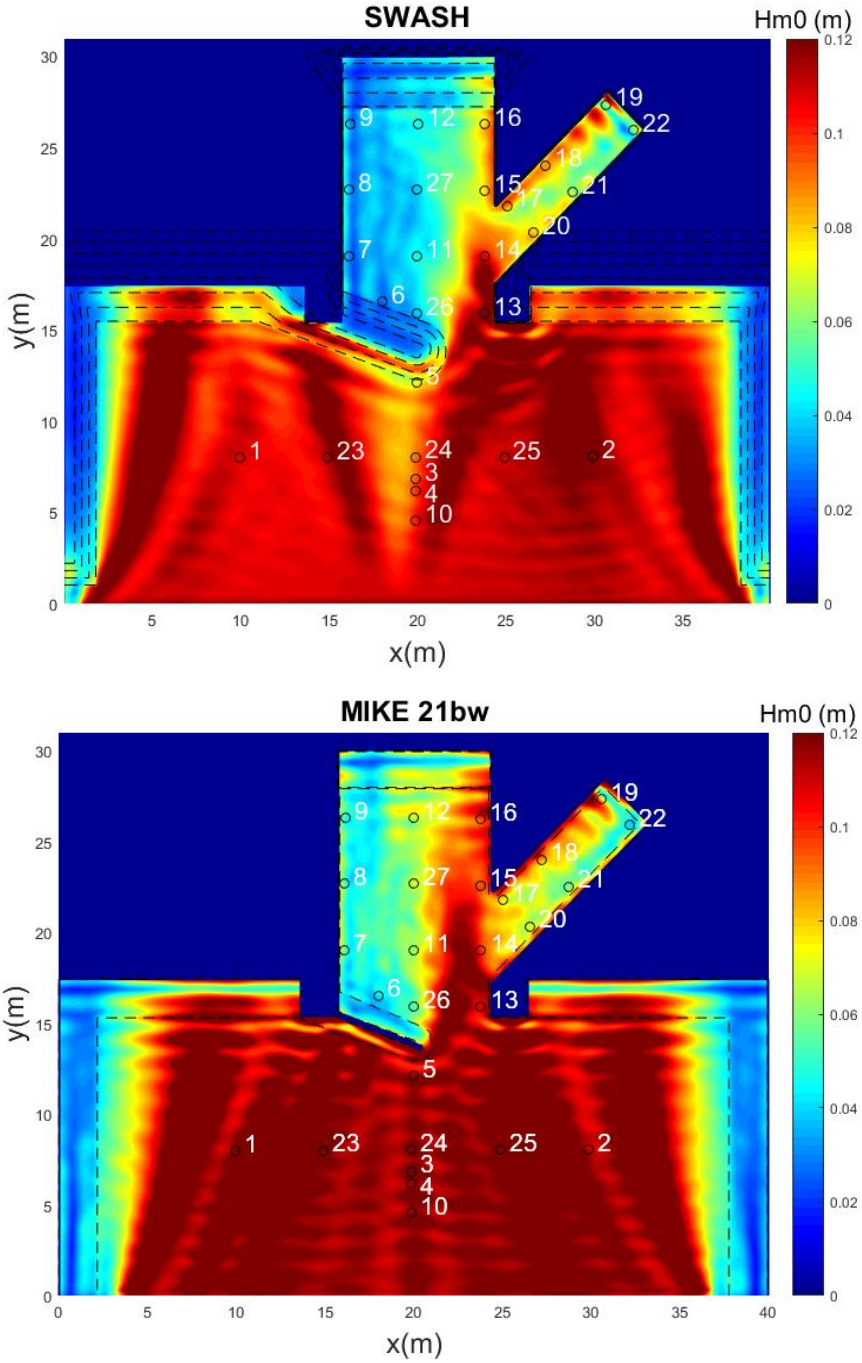

Figure 7.1. Spatial variation of the significant wave height (Hm0) for scenario T079 in physical model scale. The in black super imposed contour lines are for the height of the structures and porosity layers in SWASH and MIKE 21bw, respectively.

Figure 7.2 shows the comparison of the significant wave height based on the primary wave energy (f > 0.3 Hz) at all the wave gauges, see Figure 7.1 for the positions. From Figure 7.2 it follows that SWASH under-estimates the significant wave height by roughly 15-20% at the wave gauges in front of the breakwater which lie inside the symmetrical pattern observed in Figure 7.1. The accuracy at the other wave gauges in SWASH, besides the ones in front of the breakwater, is good and the bias at each wave gauge is on average smaller than ±10%.

MIKE 21bw performs rather poor for this scenario with a MAPE of 17.4%. The largest bias is found in the main basin, behind the breakwater and is +78%, observed at wave gauge 7.

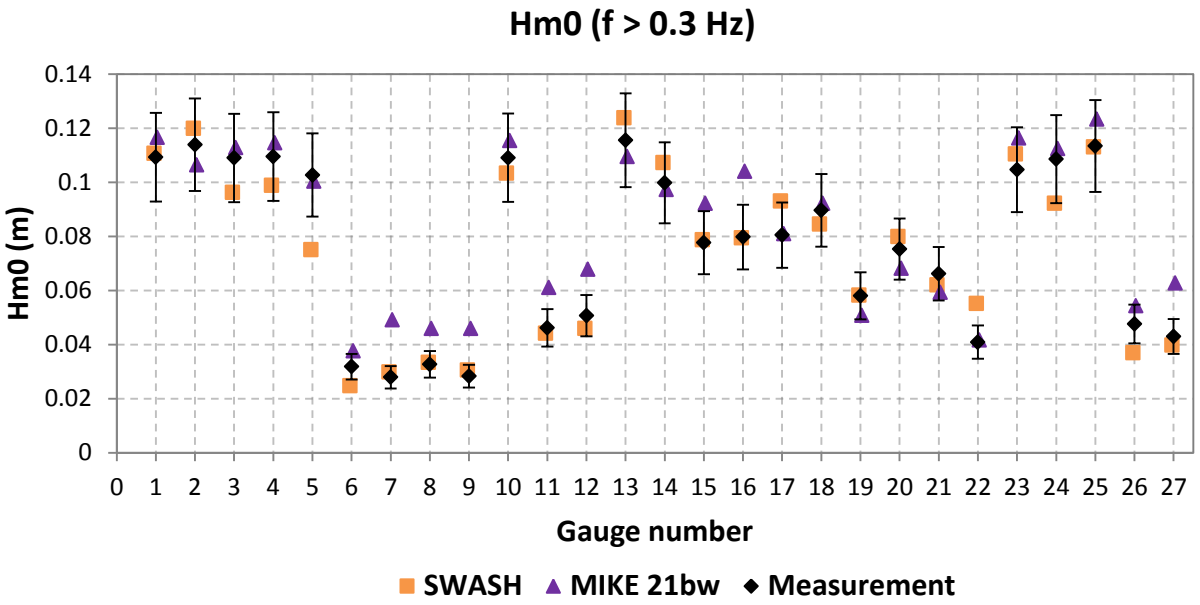

Figure 7.2. Comparison of the significant wave height (Hm0) based on the primary wave energy (f > 0.3 Hz) for scenario T079 on physical model scale. Note that the bars indicate a (fixed) measurement deviation of ±15%.

The symmetrical pattern observed in SWASH in front of the breakwater (see top panel of Figure 7.1) seems to occur due to waves which are reflected from the gravel slopes present at the left and right side of the domain (at x = 3 and x = 37 in Figure 7.1). These reflected waves from the gravel slopes interact in the middle and an anti-node seems to be present. Because this pattern is also observed for scenario T035 (see Appendix C4), it is not caused by the breakwater. Several attempts were made to prevent this symmetrical pattern from occurring. When the gravel slopes at the sides of the domain were modelled as sponge layers, i.e. (almost) no reflection, the symmetrical pattern showing an under-estimation of the significant wave height was not observed. This gives more confidence in the fact that this symmetric pattern is due to reflected waves from the gravel slopes. However, the schematisation with sponge layers is totally different than the physical model and is therefore an unrealistic schematisation.

The vertical concrete walls present at the side basin were initially modelled in MIKE 21bw as land, leading to a reflection coefficient of nearly 1. With this schematisation however, numerical instabilities (blow-up) occurred and this was circumvented by placing multiple porosity layers in the side basin in order to lower the reflection coefficient to 0.9. Nevertheless, at the end of the side basin, at wave gauge 19 and 22, an instability in the form of a resonant standing wave developed in MIKE 21bw which was not observed during the physical experiment. Therefore, this resonance is caused numerically instead of physically. A screenshot of the surface elevation is presented in Figure 7.3. The resonant wave can clearly be seen at the end of the side basin.

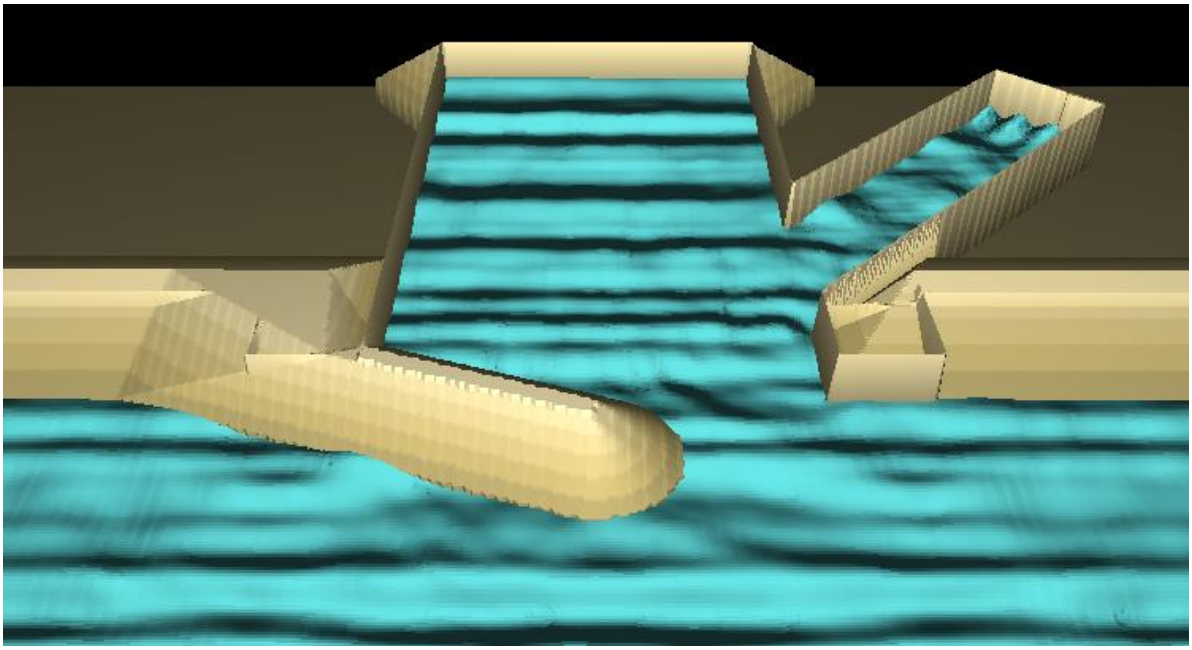

Figure 7.3. Screenshot of the surface elevation as computed by MIKE 21bw. At the end of the side basin, the resonant standing wave can clearly be seen. The screenshot is taken at the end of the simulation.

Despite multiple trial runs performed in MIKE 21bw by adding more numerical damping, i.e. using different discretisation schemes and lowering the porosity values to add more damping, the standing wave pattern kept occurring, although less significant. Further, this resonant wave pattern is also clearly visible at the obtained wave spectra at gauge 19 and 22. In Figure 7.4 the frequency spectra at wave gauge 19 are shown. The peak frequency computed by MIKE 21bw is shifted towards a frequency of 1.3 Hz due to this resonant standing wave. Furthermore, an additional run with a wider side basin was performed which resulted in a standing wave with a different frequency. Therefore, this is clearly an unwanted resonant phenomenon.

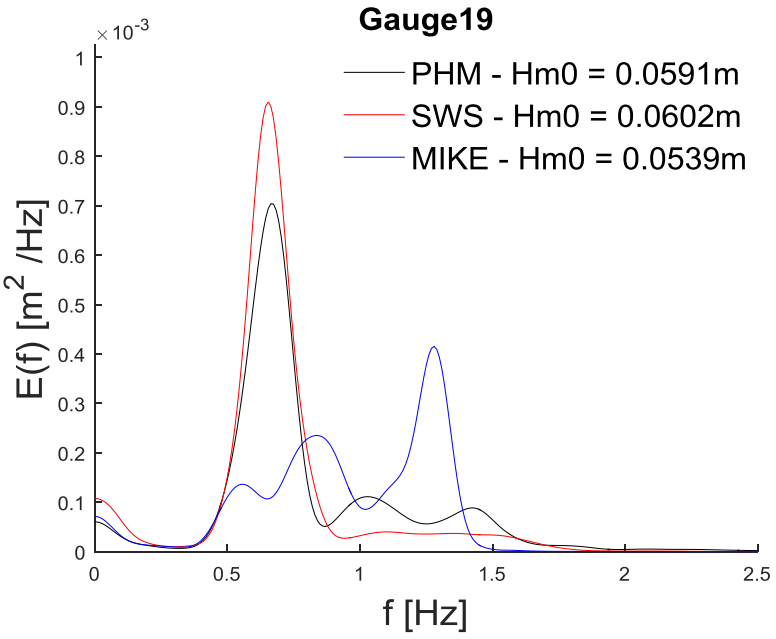

Figure 7.4. Estimated frequency spectra by MIKE 21bw, SWASH and the physical experiment at wave gauge 19 for scenario T079 in physical model scale.

The comparison of the energy period based on the primary wave energy is presented in Figure 7.5. The MAPE is 8.3% and 6.3% in SWASH and MIKE 21bw, respectively. Most noticeable is the under-prediction of MIKE 21bw at the wave gauges 19 and 22, located at the end of the side basin. Also this is due to the resonant standing wave which has a frequency of 1.3 Hz, corresponding to a period of 0.77 s. This causes the energy period for (f > 0.3 Hz) to be under-estimated by 17% and 21% at the wave gauges 19 and 22, respectively.

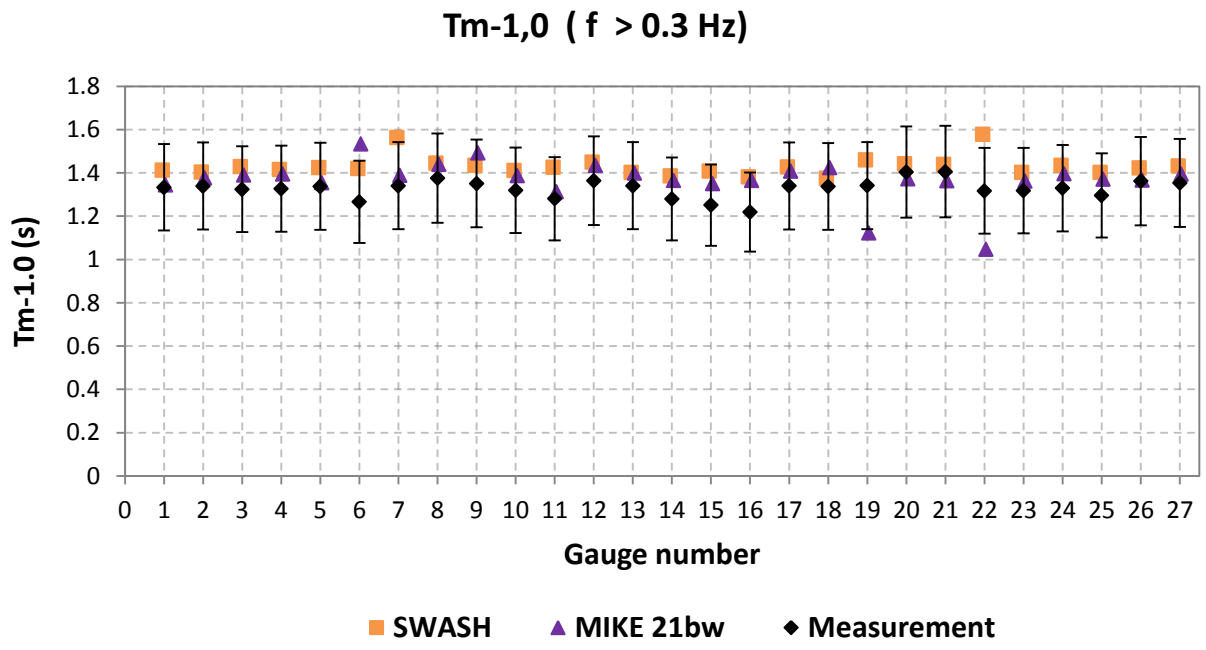

Figure 7.5. Comparison of the energy period based on the primary wave energy (f > 0.3 Hz). Note that the bars indicate a (fixed) measurement deviation of ±15%.

It turned out that by up-scaling the physical model and simulating in prototype scale, the numerical instabilities observed in MIKE 21bw and SWASH did not occur. Therefore, the comparison was made on prototype scale, at scale 1:20. As it turned out, the accuracy in predicting the wave parameters based on the low frequency energy and the low period oscillations did not change (much) when simulating in prototype scale. For that reason, the results for these wave parameters are only presented for the prototype scale in the next section. All the results in physical model scale for scenario T079 can be found in Appendix C5.

7.3 Results simulation prototype scale

This section presents a selection of results of the simulations performed on prototype scale for scenario T079. See Appendix C6 for all the results. Figure 7.6 presents the spatial variation of the significant wave height for scenario T079 on prototype scale for SWASH and MIKE 21bw. The observed patterns in both numerical models look rather similar now. It can be seen that the strange symmetrical pattern in front of the breakwater in SWASH is not present and that the estimation of the significant wave height in MIKE 21bw in the shadow zone behind the breakwater is very similar to SWASH. Furthermore, the patterns in the side basin look similar. Differences can be found in front of the breakwater, where MIKE 21bw seems to predict a slightly larger significant wave height. Further, at the gravel slopes and at the breakwater differences can be seen due to the different schematisation of the structures (breakwater and gravel slopes) in SWASH and MIKE 21bw.

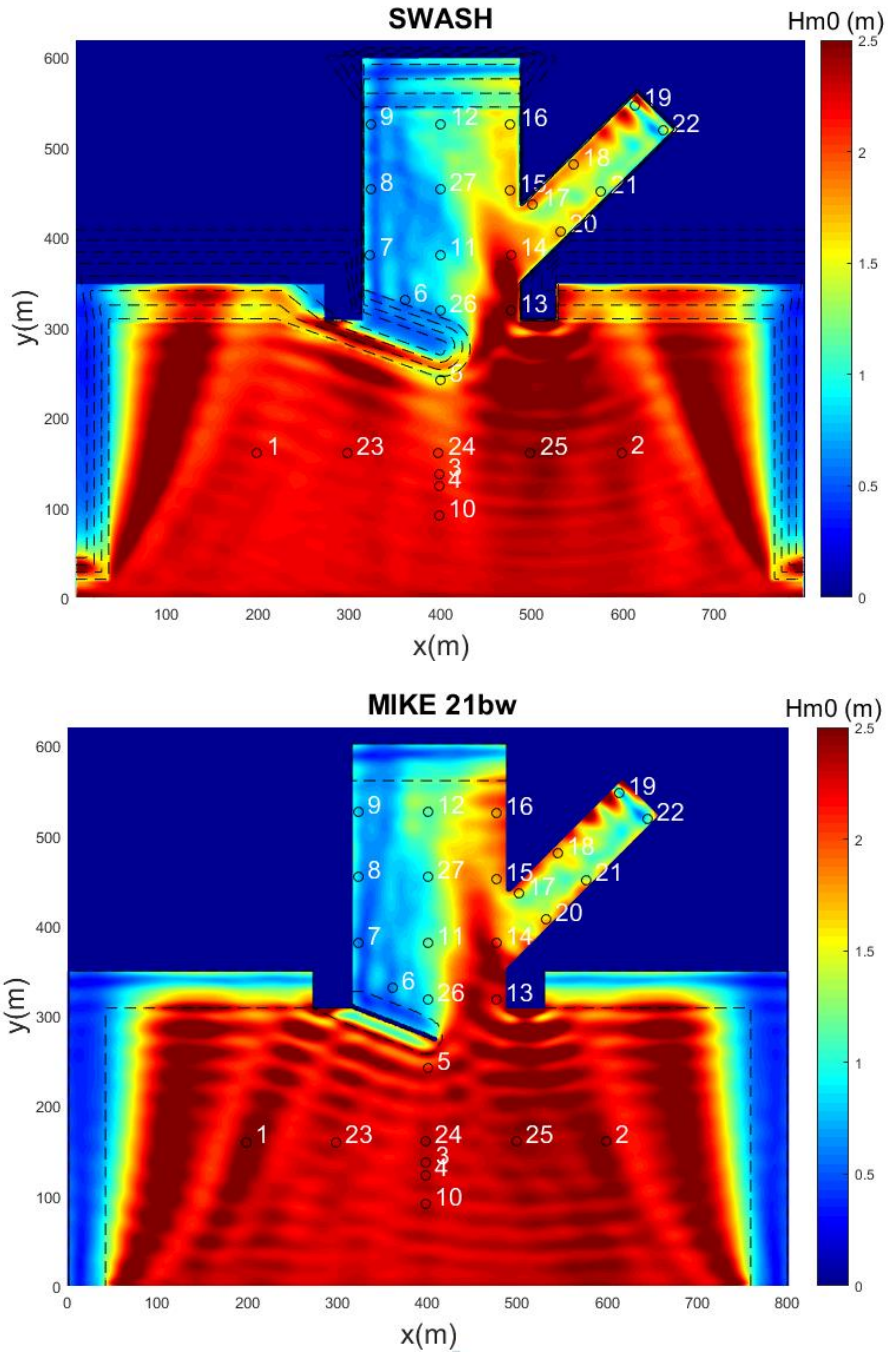

Figure 7.6. Spatial variation of the significant wave height (Hm0) for scenario T079 on prototype scale. Note that the in black superimposed contour lines present the height of the structures and the porosity layers in SWASH and MIKE 21bw , respectively.

7.3.1 Primary and low frequency waves

Significant wave height

The comparison of the significant wave height based on the primary wave energy and low frequency energy are presented in Figure 7.7, see Figure 7.6 for the position of the wave gauges. Both numerical models perform very well for the primary wave energy (f > 0.067 Hz) based on the set accuracy limit of ±15% deviation from the measurements. Only at wave gauge 22 the bias is +40% in SWASH and +27% in MIKE 21bw. However, from observing the spatial variation of significant wave height in Figure 7.6, it can be seen that for both numerical models the gradient in significant wave

height is large in the side basin. Moving the wave gauge slightly can change the estimation significantly. Therefore, this measurement is less reliable.

The low frequency energy is over-predicted in both numerical models with a MAPE of 30% in SWASH and 21% in MIKE 21bw. This is because both numerical models work with a frequency dependent reflection which follows from the porosity. Furthermore, the reflection of long waves is larger than for short waves given a certain (fixed) porosity value and geometry (see Figure 2.1). In MIKE 21bw, the porosity values assigned are based on the desired reflection coefficient for the peak period. Therefore, the reflection coefficient of the low frequency waves is too large and hence, the low frequency energy is over-predicted.

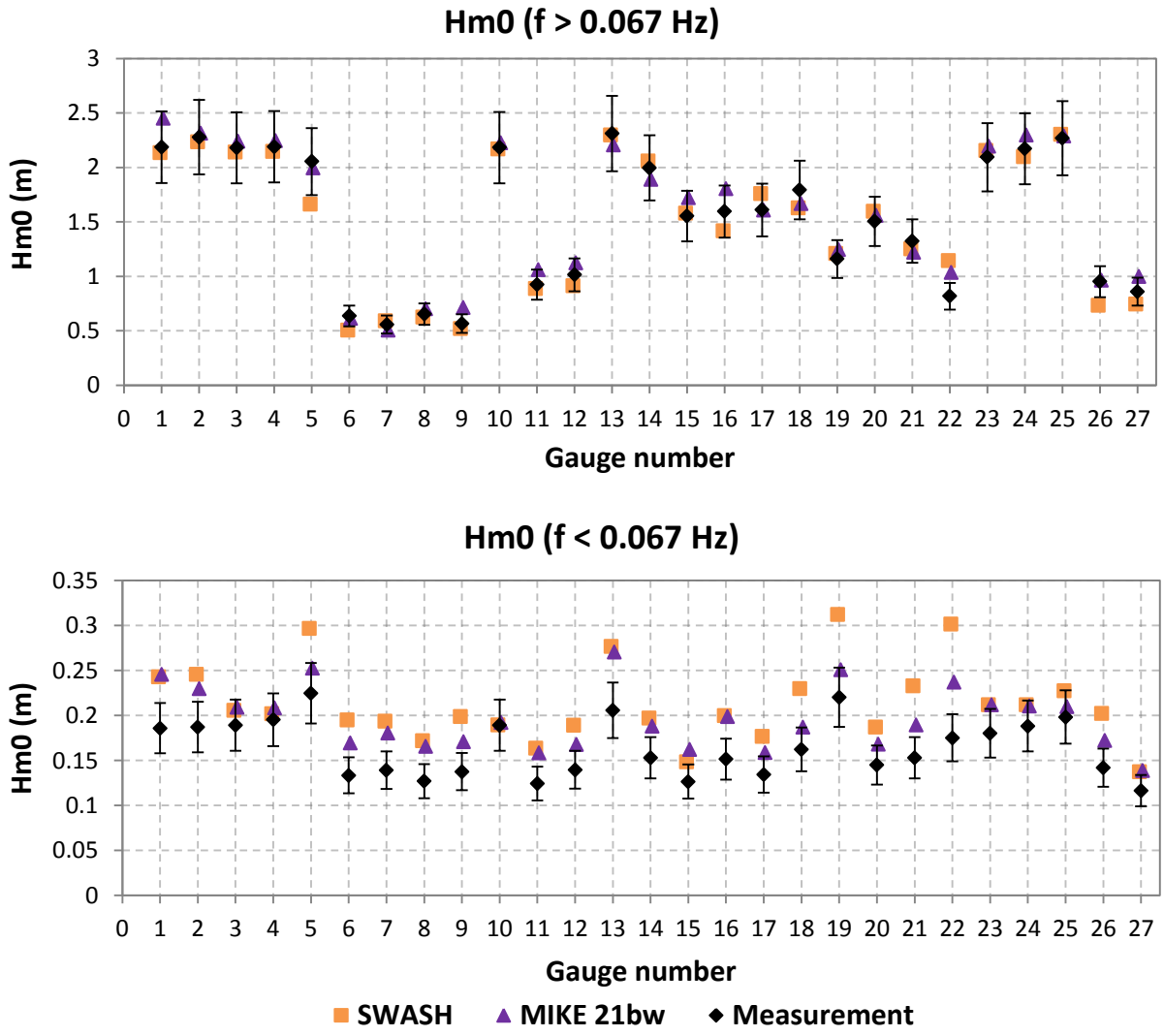

Figure 7.7. Comparison of the significant wave height (Hm0) based on the primary wave energy (f > 0.067 Hz) and on the low frequency energy (f < 0.067 Hz). Note that the bars indicate a (fixed) measurement deviation of ±15%.

By comparing the results of the simulation on physical model and prototype scale, it follows that the accuracy in predicting the significant wave height based on the primary energy is improved for both numerical models, in particular for MIKE 21bw. This is summarized in Table 7.1. The improvements in SWASH are primarily found at the wave gauges 3, 4, 10 and 23 in front of the breakwater, all lying inside the symmetrical pattern which under-predicts the significant wave height in physical model

scale. For MIKE 21bw, predictions of the significant wave height inside the main basin of the harbour have improved significantly. Also, the resonant standing wave in the side basin was not observed. To illustrate this clearer, the frequency spectra at wave gauge 19 are presented in Figure 7.8. The shift in wave energy due to the resonant standing wave as can be seen in Figure 7.4, is not present in this case.

Further, the simulations in both scales over-predict the low frequency energy by (almost) the same mean average percentage error.

Table 7.1. The mean average percentage error (MAPE), as defined in Eq. (4.2), of the significant wave height based on the primary wave energy over all the wave gauges for the simulations on physical model and prototype scale.

	Mean average percentage error (%)	
	Model type scale	**Prototype scale**
SWASH	9.3	8
MIKE 21bw	17.4	7.8

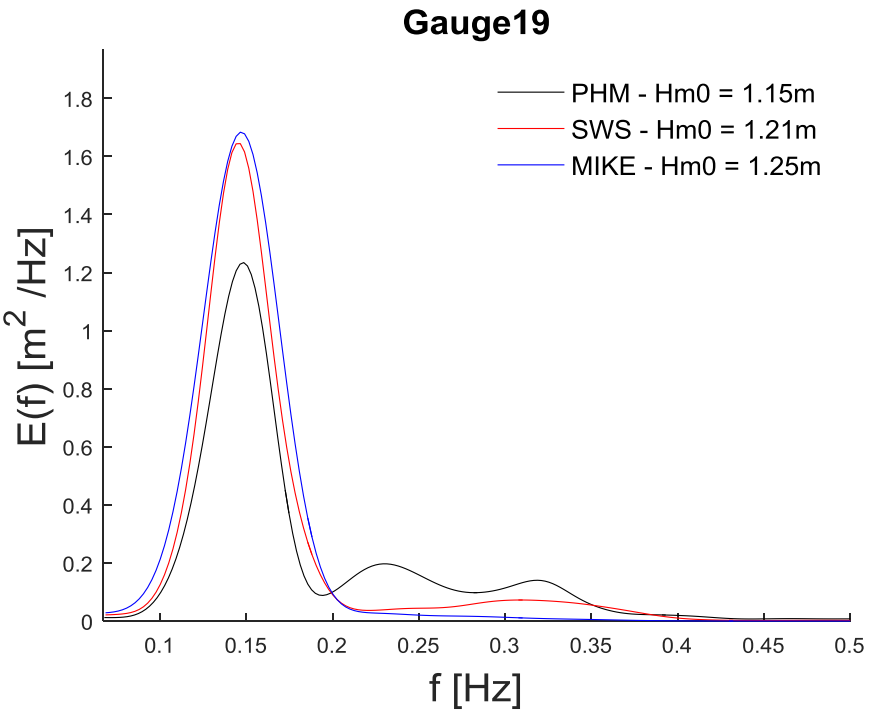

Figure 7.8. Estimated frequency spectra at wave gauge 19 for scenario T079 simulated in prototype scale.

Energy period

The comparison of the energy period based on the primary and low frequency energy shows that both numerical models perform very well, see Figure 7.9. The MAPE over all the wave gauges based on frequencies greater than 0.067 Hz is 4.8% and 7% in SWASH and MIKE 21bw, respectively. Moreover, the energy period at all the wave gauges is over-predicted. This indicates a lack of high frequency energy which is to be expected. Due to numerical damping, some high frequency energy is always filtered. Moreover, MIKE 21bw cuts the wave spectra above the maximum frequency the model can resolve, resulting in a lack of high frequency energy.

The estimated energy period based on the lower frequencies (f < 0.067 Hz) shows a MAPE of 5.9% and 8.1% for SWASH and MIKE 21bw and is considered to be good.

By comparing the predictions with the physical model scale, it follows that the MAPE estimated by both numerical models is (almost) the same. Only at the wave gauges 19 and 22, located at the end of the side basin, the estimates improve significantly in MIKE 21bw. This is because the resonant standing wave which occurred in physical model scale causing a significant under-estimation, is not present in this case.

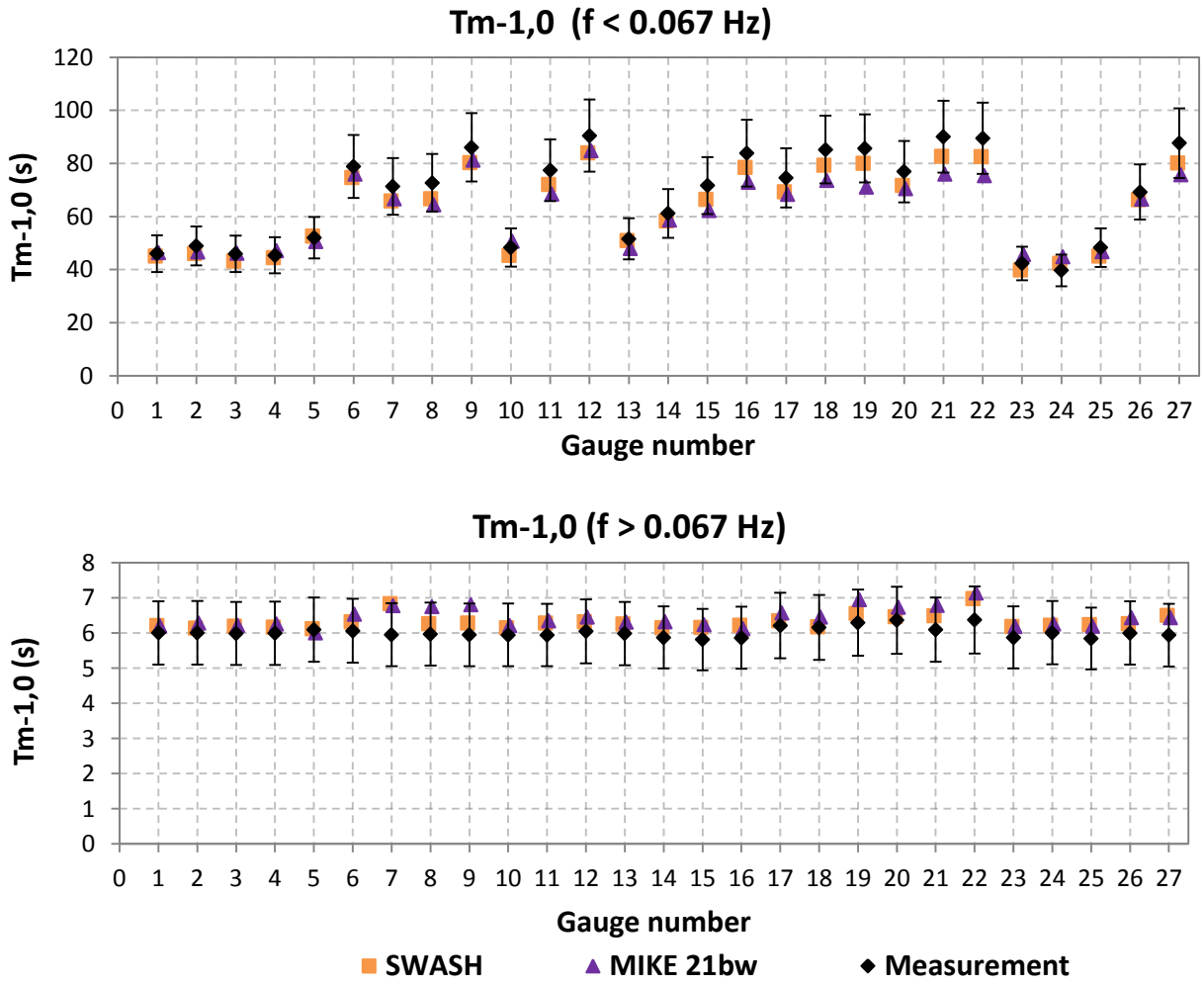

Figure 7.9. Comparison of the energy period (Tm-1,0) based on the primary wave energy and low frequency energy. Note that the bars indicate a (fixed) measurement deviation of ±15%.

7.3.2 Harbour oscillations

The results of the comparison of the amplitude of the Helmholtz modes of the main and side basin are presented in Figure 7.10. The MAPE of the amplitude of the Helmholtz mode of the main basin is 8.5% and 17.8% in SWASH and MIKE 21bw, respectively. The relative high bias in MIKE 21bw is mainly caused by the wave gauges in front of the harbour where the bias is up to +60%, observed at wave gauge 4. Though, without the wave gauges in front of the harbour, the MAPE is 10% in MIKE 21bw.

The comparison of the amplitude of the Helmholtz mode of the side basin reveals that both models perform relatively poor, with a MAPE of 62% and 29% in SWASH and MIKE 21bw, respectively. The

largest over-estimations are found in the side basin, where the significant wave height is over-estimated up to a factor of 2.5 in SWASH and 1.7 in MIKE 21bw.

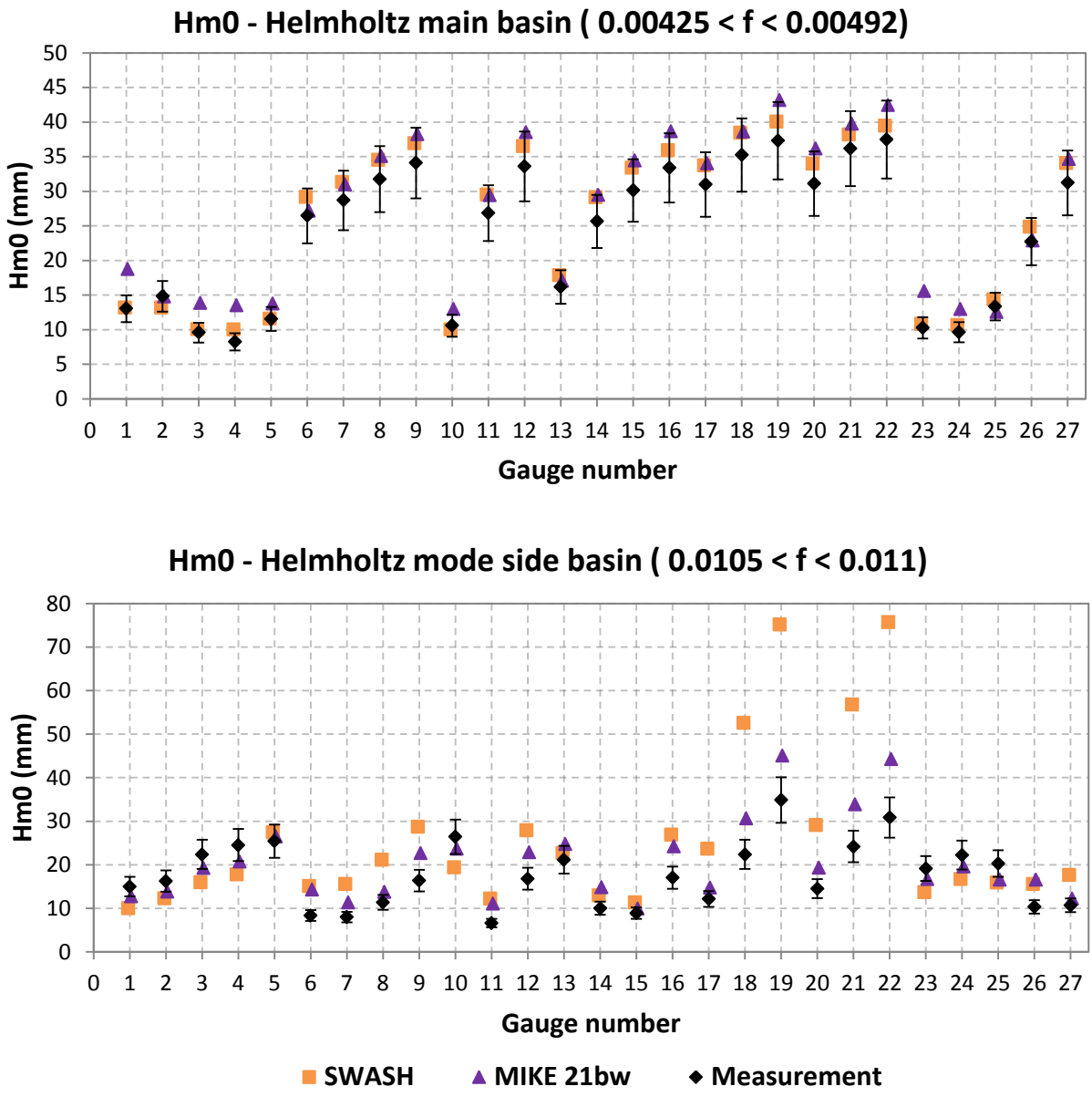

Figure 7.10. Comparison of the amplitude of the Helmholtz mode of the main and side basin. Note that the bars indicate a (fixed) measurement deviation of ±15%.

Van Mierlo (2014) reported an over-estimation of a factor 4 in SWASH for the amplitude of the Helmholtz mode of the side basin using a model setup which was identical to the one used here. Though, here it was found that the over-estimation is up to a factor 2.5. This is most likely due to a different spectral resolution. The predictions of the amplitude of the Helmholtz mode are based on the integration of a narrow frequency range and therefore, the estimations are very sensitive to the spectral resolution. When the spectral resolution is not identical in the spectra obtained from the numerical and physical model, then relative large errors are obtained. During the post processing of the data in this thesis, it was made sure that the spectral resolution of the spectra obtained from the physical model was identical to the resolution of the numerical models.

The significant wave heights based on the harbour modes are in the order of millimeters and are very sensitive to the smoothing function used to calculate the spectral density. For the same data, differences up to 100% in estimating the significant wave height were observed for different smoothing values, see Appendix A. Therefore, the reliability of the computed significant wave height is considered to be low. Although the reliability of the actual over-estimation factor is low, it is clear that SWASH over-estimates the Helmholtz mode by looking at the low frequency spectra.

Some additional runs were performed in SWASH with different porosity values for the vertical concrete wall in the side basin to investigate the effect on the amplitude of the Helmholtz mode. The results are presented in Figure 7.11. A higher porosity value leads in this case to more accurate results. This could be expected because using a higher porosity value leads to more damping and hence a lower effective reflection coefficient. However, it is questionable if a porosity value of 0.3 is realistic for a concrete wall.

A reflection coefficient of exactly 1 is never obtained in the physical experiment because there will always be some damping (friction) due to some irregularities of the concrete wall. This friction by the vertical wall can only be taken into account by using a higher porosity value in the numerical model and consequently lowering the effective reflection coefficient. Therefore, it is argued here that using a slightly higher porosity value does not necessarily need to be an unrealistic representation. Moreover, an additional advantage of using a higher porosity value is an increased stability.

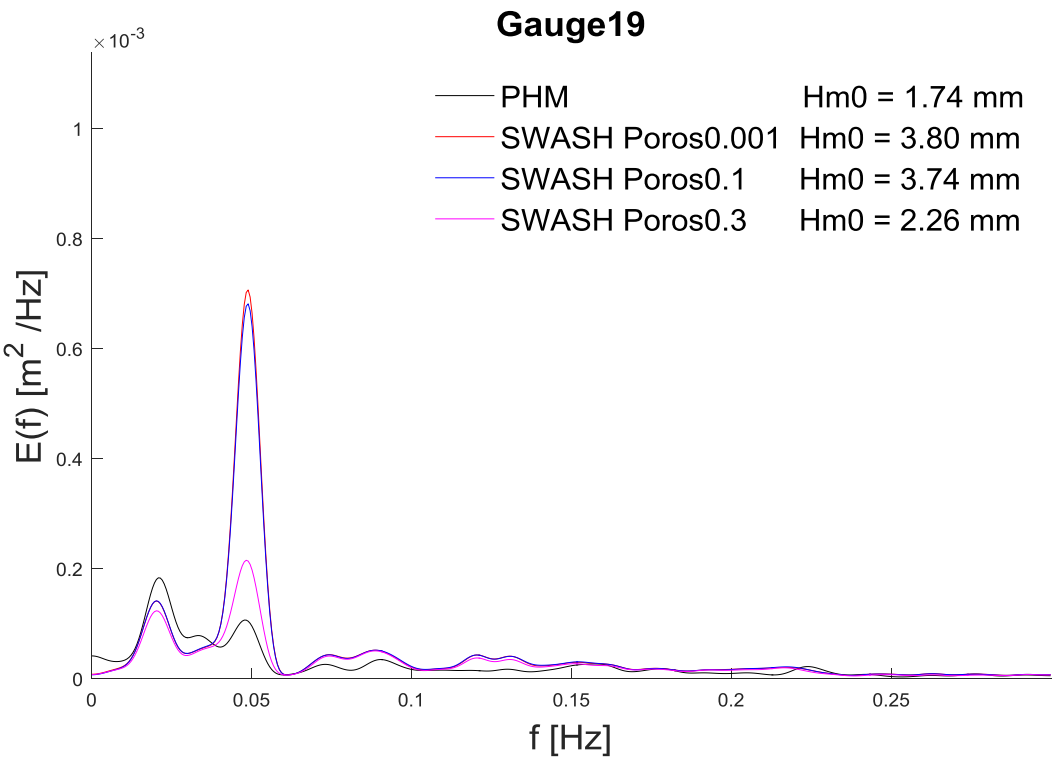

Figure 7.11. Estimated frequency spectra at wave gauge 19 for the low frequency energy (f < 0.3 Hz) in physical model scale. The spectra are plotted for different porosity values used for the schematisation of the vertical concrete wall in the side basin.

7.3.3 Stability

During the simulations it was found that SWASH is more robust than MIKE 21bw. Many critical numerical instabilities were encountered in MIKE 21bw at the boundaries with partial reflection which terminated simulations. This was circumvented by adding more porosity layers which adds more damping to the model, enhancing the stability.

Furthermore, attempts were made to add a part of the slope of the breakwater in the bathymetry in MIKE 21bw. This, however, resulted in model blow-ups and therefore no part of the slope was included. In addition, including transmission of the breakwater in MIKE 21bw resulted in a large over-estimation in the main basin (up to an over-estimation of 78%) due to a transmission coefficient which was too large. It was not possible to lower this coefficient because very low porosity values were required (< 0.2) which lead to critical numerical instabilities, see also Appendix C3. Also the gravel slopes were schematised as vertical walls without the slopes to avoid numerical instabilities.

Both models had instabilities when working in physical model scale. From Section 7.2 it follows that in MIKE 21bw a resonant standing wave occurred in the side basin, which was not present during the physical experiment. SWASH has a strange symmetrical pattern in front of the breakwater where the significant wave height is lower than the incoming significant wave height. These instabilities did not occur when simulating on prototype scale, at scale 1:20.

7.4 Discussion and conclusions

The results of the simulations on physical model scale show that:

- In both numerical models, and especially in MIKE 21bw, numerical instabilities were encountered in physical model scale. A strange symmetrical pattern was observed in SWASH in front of the breakwater where the significant wave height is lower than the incoming significant wave height. MIKE 21bw shows at the end of the side basin an unwanted resonant standing wave which was not present in the physical experiment and is therefore caused numerically. Even by adding more damping to the model, by using different discretisation schemes or lowering the porosity values, this resonant wave could not be prevented.
- The MAPE in significant wave height based on the primary wave energy (f > 0.3 Hz) is 9.3% in SWASH and is good, based on the accuracy limit of ±15% deviation in the measurements. However, in front of the breakwater at the gauges 3, 4, 10 and 24, an under-estimation up to 20% is observed.
- The performance of MIKE 21bw is poor for the simulations in physical model scale with a MAPE of 17.4% in significant wave height based on the primary wave energy (f > 0.3 Hz). Further, the significant wave height in the shadow zone of the breakwater shows a very large over-estimation, up to a bias of +78%.
- The MAPE for the energy period based on the primary wave energy (f > 0.3 Hz) is 8.3% in SWASH and 6.3% in MIKE 21bw and therefore the performance is considered good. Though, at wave gauge 19 and 22, MIKE 21bw shows an under-estimation of 17% and 21% at the wave gauges 19 and 22, respectively. This large under-estimation is due to the unwanted resonant standing wave present at the side basin.

The simulations on prototype scale show that:

- A mean average percentage error in significant wave height based on the primary and low frequency energy is 8% and 30% in SWASH. For MIKE 21bw the MAPE is 7.8% and 20.7% for the primary and low frequency energy, respectively.
- The over-prediction of the low frequency energy is because long waves are reflected more than short waves from an identical wall or slope. The porosity values are calculated (for MIKE 21bw) based on the reflection coefficient for the peak period. Therefore, the long waves will experience a higher reflection coefficient and as a result the low frequency energy is over-predicted.
- Both models perform well in predicting the energy period based on the low and high frequency energy, with mean average percentage errors below 10%.
- The Helmholtz mode of the main basin is predicted well by SWASH with a MAPE of 8.5%. MIKE 21bw shows a larger MAPE of 17.8% and is mainly caused by the wave gauges in front of the harbour. By only taking the wave gauges inside the harbour into account, the MAPE is 10% and therefore the performance in MIKE 21bw is still considered to be good.
- The Helmholtz mode of the side basin is over-predicted by both numerical models. MIKE 21bw has a MAPE of 29% while the MAPE in SWASH is 69%.
- The over-estimation of the amplitude of the Helmholtz mode in SWASH is up to a factor 2.5 in the side basin. This factor is lower than the factor 4 found by Van Mierlo (2014) and is most likely due different spectral resolutions used by Van Mierlo (2014) in the spectra of the physical and numerical model results.
- The over-prediction of the Helmholtz mode in the side basin, as computed by SWASH, can be reduced by using a higher porosity value at the vertical concrete walls. However, increasing the porosity value for a vertical concrete wall does not seem realistic. Though, a reflection coefficient of exactly 1 will be never be obtained in physical model scale due to some irregularities of the concrete walls. It can therefore be argued that a slightly lower reflection coefficient should be used in numerical models.

By comparing the simulations on physical model and prototype scale it is concluded that both models perform better when working on prototype scale. The numerical instabilities encountered when working on physical model scale are not observed in prototype scale which results in better estimations of the significant wave height based on the primary wave energy, especially in MIKE 21bw. The estimation of the mean energy period based on the primary wave energy improves slightly in MIKE 21bw because the resonant standing wave in the side basin is not observed which caused a severe under-estimation of the energy period in the side basin. The comparison of the wave parameters based on the low frequency energy and the long period oscillations do not show a significant difference when comparing the simulations in both scales.

It would be expected that the scale on which the simulations are performed should not matter when the same amount of grid cells (per wave length) are used. However, from the simulations performed here, it follows that running the numerical models on a small scale leads to numerical instabilities, in particular for MIKE 21bw. A possible explanation is that for the simulations on physical model scale, the small numbers used in the calculations can cause problems. Both MIKE 21bw and SWASH do not use double precision, so rounding errors could be of importance when working in small scales, leading to numerical instabilities.

8 Conclusions and recommendations

A comparison study between the two numerical models SWASH and MIKE 21bw is presented in this thesis. The main aim is to determine the computational efficiency of the two numerical models, given certain accuracy limits, for waves encountering approach channels and waves propagating into harbours. The study addresses the following research questions:

- What are the theoretical differences between Mike 21bw and SWASH?
- What is the computational efficiency of SWASH and MIKE 21bw and what are their boundaries of applicability based on the simulation results of two physical experiments?
- What causes the differences between the numerical and physical model results and how can they be minimized?

In this chapter the conclusions and recommendations drawn are presented and subdivided into three sections. In Section 8.1, specific conclusions and recommendations regarding the simulations of Case 1 (the approach channel) are presented. Next, in Section 8.2 specific conclusions and recommendations for Case 2 (the harbour) are presented. Finally in Section 8.3, more general conclusions are drawn regarding the differences between the numerical models and a discussion is given on the use of both numerical models. In addition, general guidelines on when or whether to choose one of the models is presented.

8.1 Case 1: approach channel

8.1.1 Conclusions

From the comparison study based on the physical experiment of the approach channel (Case 1) the following is concluded:

- Both numerical models perform well in predicting the significant wave height based on the cut-off spectra ($f < 0.13$ Hz) with mean average percentage errors of 8% and 6% in SWASH for scenario C1 and C2, respectively. Further, MIKE 21bw shows mean average percentage errors of 10% for scenario C1 and 14% for scenario C2. So, all the errors lay within the set accuracy limit of ±15% deviation in the measurements.
- The energy period is predicted well based on the cut-off spectra ($f < 0.13$ Hz) with mean average percentage errors of 2% and 3% in SWASH and MIKE 21bw, respectively, for scenario C1. The mean average percentage errors for scenario C2 are 3% and 4% for SWASH and MIKE 21bw, respectively.
- The numerical models perform relatively poor in estimating the significant wave height based on the total wave spectra with a mean average percentage error of 21% in SWASH and MIKE 21bw for scenario C1. The mean average percentage errors for scenario C2 are 12% in SWASH and 16% in MIKE 21bw. Moreover, the significant wave heights are under-estimated.
- The energy period based on the upper part of the spectrum ($f > 0.13$ Hz) is over-estimated in both numerical models because contributions in the upper part of the spectrum are omitted. The mean average percentage errors are 11% and 14% in SWASH and MIKE 21bw for scenario C1, respectively. For scenario C2 the mean average percentage errors are 8% and 12% for SWASH and MIKE 21bw, respectively. The performance of the numerical models is still considered to be good because the bias at each wave gauge is less than ±15% deviation in the measurements.

- The computational requirements are less for MIKE 21bw than SWASH. The computation time is a factor 10 faster in MIKE 21bw when simulating on six processors for this case. Although, this factor gets smaller when more processors are used due to higher speed up factors in SWASH compared to MIKE 21bw.
- The computational cost for SWASH using one vertical layer is (almost) identical to MIKE 21bw. However, for this particular case the mean average percentage error in significant wave height is 13%, which is 8% when simulating with two vertical layers.
- The numerical stability or robustness is comparable for both numerical models for this case.

Sensitivity analyses were performed by varying certain model parameters which aim to explain the observed differences in numerical model results. The following conclusions are drawn:

- Numerical damping cannot (fully) explain the under-prediction observed in the significant wave heights based on the total wave spectra in SWASH, a possible cause as was suggested by Dusseljee et al. (2014) and Riezebos (2014). Furthermore, SWASH has more numerical damping than MIKE 21bw for this case (using discretisation schemes which have the least amount of numerical damping and lead to numerical stable computations).
- MIKE 21bw under-estimates wave breaking when the default parameters and a horizontal resolution of 3 m x 3 m are used. This under-estimation of wave breaking explains the over-estimation of the significant wave height at the wave-ward side of the channel, observed in MIKE 21bw for scenario C2.
- Upscaling the incoming wave spectrum in MIKE 21bw to make sure the incoming significant wave height at the wave generation line is correct, only partially works because it comes at the expense of the spectral shape. In other words, the energy which MIKE 21bw cannot resolve above the maximum frequency, is shifted towards the lower frequencies to make sure the same amount of wave energy comes into the computational domain.

8.1.2 Recommendations

Based on the conclusions of the physical experiment of the approach channel presented in Section 8.1.1, the following recommendations are presented:

- As the measurement data was already post-processed it is recommended to check the post processing of the raw measurement data and in addition, to post process the raw measurement data on exactly the same way as the obtained results from the numerical models, to make sure that no differences arise from the post processing of the data.
- When directional information at the GRSM gauges becomes available, it is recommended to perform a directional analysis in both numerical models to compare the computed directional distribution of the wave energy per frequency and to see whether the numerical models accurately resolve the (long) wave refraction at the slopes of the navigation channel.
- It is recommended to use a different physical experiment of a navigation channel because the current experimental setup introduces quite some uncertainties on how the physical model should be schematised in the numerical models. Further, it is believed that the inaccuracies in the measurements of the physical experiment are quite severe. The new physical experiment should define the boundary conditions better, i.e. the bar at the entrance of the channel should not be present or stones which are to scale should be used. Further, because the wave-channel interaction is the main process of interest, no structures

should be present and ideally, the wave guiding walls at the boundaries should be as far away from the channel as possible to minimize the effect of other wave phenomena such as reflection.

8.2 Case 2: harbour

8.2.1 Conclusions

Initially, the comparison study based on the physical experiment of the harbour (Case 2) was done at physical model scale, which is identical to the scale of the physical experiment to avoid scale effects. However, due to some numerical instabilities encountered in the physical model scale for both numerical models, the comparison was also performed on a prototype scale, Froude scaled at scale 1:20.

From the comparison study based on the simulations performed at physical model scale the following is concluded:

- Both models have problems with the simulations performed at physical model scale due to encountered numerical instabilities, especially in MIKE 21bw.
- The overall accuracy in SWASH regarding the significant wave height based on the primary wave energy ($f > 0.3$ Hz) is good, based on the set accuracy limit of ±15% deviation in the measurements, with a mean average percentage error of 9.3%. Though, the wave gauges in front of the breakwater show a bias up to -20% due to the numerical instability observed in front of the breakwater.
- The performance of MIKE 21bw is rather poor with a mean average percentage error of 17.4% in significant wave height based on the primary wave energy ($f > 0.3$ Hz). This large error is mainly caused by over-predictions at the wave gauges which lie in the shadow zone of the breakwater which are up to a bias of +78%.
- The performance of the numerical models in predicting the energy period based on the upper part of the spectra ($f > 0.3$ Hz) is good for both numerical models with mean average percentage errors of 8% and 6% in SWASH and MIKE 21bw, respectively, and lie within the ±15% deviation from the measurements. However, at the wave gauges 19 and 22 which lie at the end of the side basin, MIKE 21bw performs poor and shows an under-estimation of roughly 20% due to the unwanted resonant standing wave in the side basin.

From the comparison on prototype scale, the following conclusions are drawn:

- The performance of the numerical models is much better in prototype scale compared with the performance on physical model scale, in particular for MIKE 21bw. The observed numerical instabilities in physical model scale are not encountered in prototype scale. Therefore, the accuracy in predicting the wave parameters based on the primary wave energy ($f > 0.067$ Hz) has improved significantly, especially for MIKE 21bw. The accuracy of the wave parameters based on the low frequency energy ($f < 0.067$ Hz) and the long period oscillations are comparable with those of the simulations performed on physical model scale.
- Both models perform well in predicting the significant wave height based on the primary wave energy with mean average percentage errors of 8% and 7.8% in SWASH and MIKE 21bw, respectively.

- The significant wave height based on the low frequency energy is over-predicted by both numerical models and they show mean average percentage errors of 30% in SWASH and 21% in MIKE 21bw. This is because the (effective) reflection of the low frequency waves is higher than for high frequency waves given a (fixed) porosity value, leading to an over-estimation.
- The estimates of the energy periods based on the primary wave energy ($f > 0.067$ Hz) is good with mean average percentage errors of 4.8% in SWASH and 7% in MIKE 21bw. The energy periods based on the low frequency energy ($f < 0.067$ Hz) are also predicted well with mean average percentage errors of 5.9% and 8.1% in SWASH and MIKE 21bw, respectively.
- Both models predict the amplitude of the Helmholtz mode of the main basin reasonably well, with mean average percentage errors of 8.5% and 17.8% in SWASH and MIKE 21bw, respectively. Furthermore, the amplitude of the Helmholtz of the side basin is predicted relatively poor by both numerical models with a mean average percentage error of 29% in MIKE 21bw and 69% in SWASH.
- The estimates of the amplitude of the Helmholtz mode are very sensitive to the resolution of the spectrum. When the resolution of the spectrum obtained from the measurements and from the numerical model SWASH is identical, the Helmholtz mode of the side basin is over-estimated by a factor 2.5 in SWASH, which is smaller than the factor 4 reported by Van Mierlo (2014).
- The large over-estimation of the Helmholtz mode in SWASH is due to a reflection of the vertical wall which is almost 1 and is considered too high. Additional runs using higher porosity values, to take the friction of the vertical concrete walls into account, resulted in more accurate results.

8.2.2 Recommendations

Based on the conclusions of the physical experiment of the harbour presented in Section 8.2.1, the following recommendations are given:

- The simulations on physical model scale show multiple numerical instabilities (in SWASH a strange symmetrical pattern in front of the breakwater and in MIKE 21bw an unwanted resonant standing wave in the side basin). It is recommended to investigate these numerical instabilities further, to see what causes them and how they can be prevented.
- A possible explanation for the encountered numerical instabilities is that both models do not work with double precision and thus rounding errors may be important when working in small scales. This potentially leads to numerical instabilities. Therefore, it is recommended to see whether this is the reason for the numerical instabilities in physical model scale. However, using double precision would lead to a significant larger size of the output files. Thus, it is also recommended to investigate how much more accurate the numerical models become when using double precision and if it is worth saving the results in significant larger output files.

8.3 General conclusions and discussion

General conclusions about the differences between the numerical models are presented in this section. Moreover, the differences are described on different levels, i.e. on a conceptual level (the physics behind the model), the numeric (how are the differential equations solved) and the software part.

Physics

By looking at the physics behind the numerical models it can be concluded that the models are fundamentally different, i.e. based on different equations and assumptions. MIKE 21bw is based on the Boussinesq equations which eliminate the vertical coordinate while taking the non-hydrostatic pressure (partially) into account by higher order derivative terms. In other words, the vertical structure of the velocity is imposed and is not an exact solution of the equations. Therefore, a severe application limit is the deep water limit expressed as a maximum kd ratio, which is for the enhanced Boussinesq equations 3.1. When the maximum water depth is known throughout the computational domain, the application limit can then be expressed in a minimum wave period (or maximum frequency) the model can resolve. Thus, MIKE 21bw is only able to resolve the wave energy up to a maximum frequency.

SWASH on the other hand solves the Reynolds-Averaged Navies-Stokes equations (RANS) together with continuity and the vertical coordinate is not removed from the 3D differential equations. The application limit in terms of a *kd* ratio is dependent on the discretisation of the vertical, see also the next paragraph. By using two vertical layers, the maximum *kd* ratio is 7.7.

Numeric

MIKE 21bw and SWASH make use of different numerical schemes to solve the differential equations. In MIKE 21bw, four different numerical schemes are available for the space discretisation. Which scheme to choose depends on the required accuracy, numerical stability and the computational requirements. The most accurate scheme (central differencing) is also the least stable one, while the least accurate one (simple upwinding) is numerically most stable and has the minimum amount of computational requirements.

In SWASH, different schemes can also be chosen for the space discretisation of the horizontal advection terms which are also a trade-off between accuracy, numerical stability and computational requirements. The main difference with MIKE 21bw is that the vertical should be discretised as well because the vertical coordinate is not removed from the differential equations. By using more vertical layers, i.e. increasing the vertical resolution, the application limit in terms of a kd ratio can be increased. Though, this leads to higher computational requirements.

The numeric used throughout this thesis and used for the simulation of the two cases (approach channel and harbour) were chosen so that the computations were stable and the highest accuracy in predicting the significant wave height and energy period is obtained. Moreover, two vertical layers were applied in SWASH because the maximum kd ratio of the approach channel (Case 1) is 0.93 and for (Case 2) the harbour the ratio is 1.03. By comparing the computational efficiency based on the two cases, the following overall conclusions are drawn:

- The accuracy of SWASH is as good as MIKE 21bw and is for both models considered to be sufficient of ‘good’, based on the set accuracy limit of ±15% deviation of the measurements.
- The computational requirements are less for MIKE 21bw than for SWASH. The computation time needed for the simulations is by far less for MIKE 21bw than for SWASH. Though, the benefit of parallel computing is much higher in SWASH than for MIKE 21bw resulting in smaller differences in computation time when simulating on more processors. Therefore, the computations in SWASH require a great amount of computation power to make sure the computation time is within acceptable limits.

- SWASH is numerically more stable/robust than MIKE 21bw. MIKE 21bw requires more numerical 'tricks', such as placing extra porosity layers, in order to run stable computations. Furthermore, SWASH is able to run stable computations when including slopes in full detail and can resolve the total frequency spectra on the contrary to MIKE 21bw, which cannot resolve frequencies above a certain maximum frequency due to the kd limit.

It is important to note that the larger computational demands in SWASH are mainly caused by the fact that two vertical layers were used. When one vertical layer is applied, the computational requirements are identical to MIKE 21bw. However, this comes at the expense of the accuracy. For the two considered cases here, the prediction of the significant wave heights were about 5% worse when using one vertical layer instead of two. For most engineering applications and commercial projects, this loss of accuracy would not be a major restriction. However, the maximum kd ratios for the two cases considered are around one. When higher kd ratios are used, the loss of accuracy increases and the use of one layer would most likely not suffice anymore.

Software
SWASH is an open source code which is freely available online. This is a great benefit for researchers and developers. MIKE 21bw on the other hand is an operational tool, it provides costumer support which is a great advantage when numerical instabilities are encountered and need to be solved fast due to tight schedules of engineering projects.

8.3.1 General guidelines
Figure 8.1 presents a flow chart for the selection of MIKE 21bw or SWASH, solely for wave modelling purposes. Each step of the flow chart is described in more detail below.

Step 1
The first step considers the application range of both numerical models in terms of a maximum kd value. This value is determined by the maximum water depth in the area of interest and by the minimum wave period which needs to be resolved accurately. For practical applications, this can generally be the peak period.

When the maximum kd value is below 0.5, both numerical models can be used. In SWASH, one vertical layer would suffice and therefore the computational requirements in this case are identical. Because SWASH was found to be more robust than MIKE 21bw, SWASH is recommended for simulations with these low kd values. Further, for kd values higher than 3.1, MIKE 21bw cannot be used at all. In SWASH, at least two vertical layers are needed for kd values larger than 3.1 in order to have the highest accuracy.

Step 2
The second step is also based on the application range for both models in terms of wave processes which can be included. MIKE 21bw cannot take: wave-current interaction, wave damping by vegetation and wind driven flows into account. When one of these wave processes is important and needs to be included in the computations, SWASH needs to be used.

Step 3
When wave breaking needs to be included in the model runs, both models can in principle be used. However, SWASH is recommended because the computations are much more stable when wave

breaking is included. Moreover, MIKE 21bw requires many input parameters for wave breaking (amongst others: type of roller, roller celery factor, initial and final breaking angle) while SWASH only requires a value for the maximum steepness parameter.

Step 4
Step four focusses on the amount of detail required in the simulations. MIKE 21bw is not able to resolve the total wave spectra because it cannot resolve wave energy above a certain maximum frequency, which is dependent on the maximum water depth. Furthermore, a minimum water depth is required in MIKE 21bw to be able to run stable computations and therefore, sloping boundaries cannot be fully taken into account. When such detail is required, SWASH has to be used.

Step 5
Step five is important for commercial projects where time is limited and numerical instabilities which may occur need to be fixed quickly. MIKE 21bw is a commercial package and therefore it has costumer support, on the contrary to SWASH. Thus, when costumer support is desired, MIKE 21bw has to be used.

Step 6 and 7
Step six considers the computational requirements. When computational requirements are not a severe restriction, SWASH is recommended because it is numerically more stable.

When there are severe restrictions regarding the computational requirements and working in the application range of kd values between 0.5 and 3.1, two vertical layers are needed in SWASH to obtain most accurate results. Though, when two vertical layers are applied, the computational requirements in SWASH are higher (and probably too high) than in MIKE 21bw and therefore SWASH with two vertical layers is not recommended in this case.

However, SWASH can be used with one vertical layer. With one vertical layer, the computational requirements for SWASH and MIKE 21bw are identical. However, the accuracy in SWASH becomes less when one vertical layer is used and the maximum kd value is larger than 0.5. Therefore, MIKE 21bw should be used when a high accuracy is required in determining wave parameters. When a high accuracy is not necessary, SWASH can be used with one vertical layer. Though, it is not exactly known beforehand how less accurate SWASH becomes when using one vertical layer for kd values higher than 0.5, see also the recommendations in Section 8.3.2.

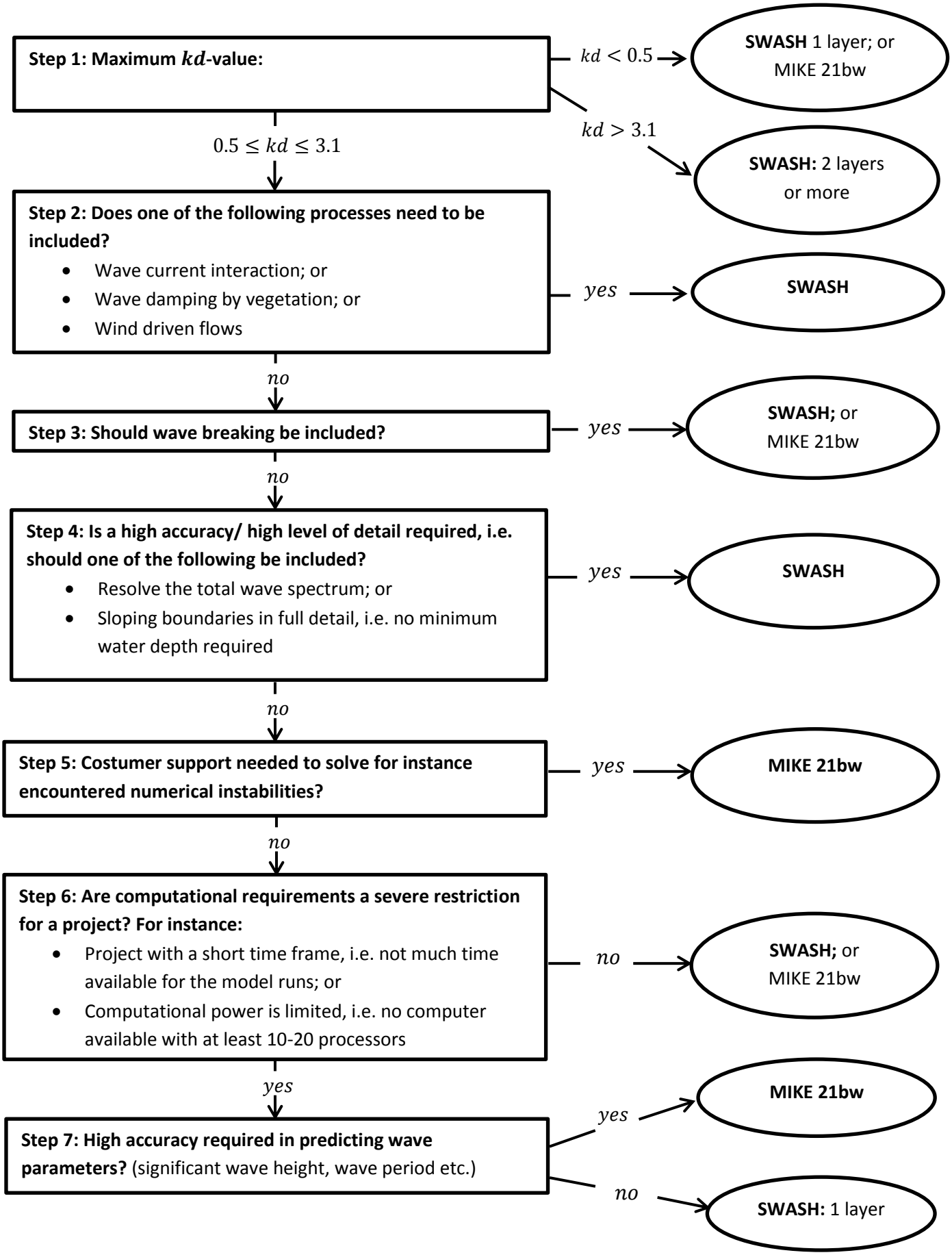

Figure 8.1. Flowchart for selecting the numerical model SWASH or MIKE 21bw for wave modelling purposes. Note that when SWASH and MIKE 21bw can both be used, the preferred model is written down in bold letters. For more details on each step, see Section 8.3.1.

8.3.2 Recommendations regarding SWASH

- The computational requirements are the main limitation in SWASH for commercial projects when two vertical layers are required and it is therefore recommended to reduce the calculation times when using more than one vertical layer.

  Further, SWASH has the option to assume a constant vertical pressure from the bottom up to a certain height and thereby eliminating the pressure from the set of equations in a vertical layer. This reduces the computational time considerably. Although the SWASH user manual already gives guidelines on the optimal distribution of the vertical layers when using a constant pressure at the bottom, it is recommended to extent/ add a more specific guideline in terms of the order of errors (in for instance significant wave height) that are made when assuming a vertical pressure (over a certain depth) as a function of the maximum water depth and peak period of the incoming waves. In other words, what the loss in accuracy is when assuming a constant pressure over a certain depth for a given maximum kd ratio.
- When using one vertical layer, the computational demands are similar in SWASH compared to MIKE 21bw. However, it is not exactly known a priori when one vertical layer would lead to an acceptable accuracy when the maximum kd value is larger than 0.5, i.e. what the order of the errors are. Therefore, it is recommended to add a guideline to the SWASH user manual with what the order of errors are, in terms of significant wave height as a function of maximum water depth and peak wave period of the incoming waves, when using one vertical layer. Such a guideline would be of benefit for commercial projects with a short time frame, to see if the loss of accuracy when using one vertical layer is acceptable.

References

Abbott, M., and Minns, A. (1998). *Computational hydraulics*. Aldershot: Ashgate.

Borsboom, M., Doorn, N., Groeneweg, J., and Gent, M. (2001) A Boussinesq-Type Wave Model That Conserves Both Mass and Momentum. *Coastal Engineering* 2000: pp. 148-161.

Bosboom, J., and Stive, M. (2015). *Coastal dynamics 1*. Delft: Delft Academic Press.

Casulli, V., and Stelling, G. (1998). Numerical Simulation of 3D Quasi-Hydrostatic, Free-Surface Flows. *Journal Of Hydraulic Engineering*, *124*(7), 678-686.

De Roo, S., Suzuki, T., Kolokythos, G., Zhao, G., and Verwaest, T. (2015). Numerical modelling of 2D wave transformation processes from nearshore to a shallow foreshore: comparison between the Mike21, swash and XBeach models. In *36th IAHR World Congress* (pp. 1-6).

DHI. (2007). *MIKE 21 bw User guide.*

DHI. (2015). *MIKE 21 Boussinesq Wave Module – short description*

Dingemans, M. (1997). *Water wave propagation over uneven bottoms*. River Edge, NJ: World Scientific Pub. (pp. 361-398)

Dusseljee, D. W., Kuiper, C., and Klopman, G. (2012). Wave modelling in navigation channels, Proc. 4th Int. Conf. of the Application of Physical Modelling to Port and Coastal Protection – Coastlab 12, Ghent, Belgium, 465-474.

Dusseljee, D., Klopman, G., Van Vledder, G., and Riezebos, H. (2014). Impact of harbor navigation channels on waves: a numerical modelling guideline. *Int. Conf. Coastal. Eng.*, *1*(34), 58.

Engelund,F. (1953). On the Laminar and Turbulent Flows of Ground water through Homogeneous Sands, Bulletin of the Technical University of Denmark, Copenhagen, No.4.

Frostick, L., McLelland, S., and Mercer, T. (2011). *Users guide to physical modelling and experimentation*. Boca Raton: CRC Press/Balkema Book.

Groeneweg, J., Van Nieuwkoop, J., and Toledo, Y. (2014). On the modelling of swell wave penetration into tidal inlet systems. *Int. Conf. Coastal. Eng.*, *1*(34), 10.

Groeneweg, J., van Gent, M., van Nieuwkoop, J., and Toledo, Y. (2015). Wave Propagation into Complex Coastal Systems and the Role of Nonlinear Interactions. *J. Waterway, Port, Coastal,Ocean Eng.*, *141*(5), 04015003.

Holthuijsen, L. (2007). *Waves in oceanic and coastal waters*. Cambridge: Cambridge University Press.

Kirby, J. T., and Dalrymple, R. A. (1983). Propagation of obliquely incident water waves over a trench. *Journal of Fluid Mechanics*, *133*, 47–63.

Kofoed-Hansen, H., Kerper, D.R., Sørensen, O. R., and Krikegaard, J. (2005). Simulation of long wave agitation in ports and harbours using a time-domain Boussinesq model. *Proceedings of Fifth Internationa Symposium on Ocean Wave Measurement and Analysis-Waves. Madrid, Spain*.

Kofoed-Hansen, H., Sloth, P., Sørensen, O. R., and Fuchs, J. (2000). Combined numerical and physical modelling of seiching in exposed new marina. *Coastal Engineering*, 3600-3614.

Kuik, A., van Vledder, G., Holthyijsen, L. (1988). A Method for the Routine Analysis of Pitch-and-Roll Buoy Wave Data. *J. Phys. Oceanogr., 18(7), 1020-1034.*

Larsen, J., and Dancy, H. (1983). Open boundaries in short wave simulations — A new approach. *Coastal Engineering*, *7*(3), 285-297.

Madsen, P. (1983). Wave reflection from a vertical permeable wave absorber. *Coastal Engineering*, *7*(4), 381-396.

Madsen, P., Murray, R., and Sørensen, O. (1991). A new form of the Boussinesq equations with improved linear dispersion characteristics. *Coastal Engineering*, *15*(4), 371-388.

Madsen, P., and Sørensen, O. (1992). A new form of the Boussinesq equations with improved linear dispersion characteristics. Part 2. A slowly-varying bathymetry. *Coastal Engineering*, *18*(3-4), 183-204.

Madsen, P., and Sørensen, O. (1993). Bound waves and triad interactions in shallow water. *Ocean Engineering*, *20*(4), 359-388.

Madsen, P., Sørensen, O., and Schäffer, H. (1997a). Surf zone dynamics simulated by a Boussinesq type model. Part I. Model description and cross-shore motion of regular waves. *Coastal Engineering*, *32*(4), 255-287.

Madsen, P., Sørensen, O., and Schäffer, H. (1997b). Surf zone dynamics simulated by a Boussinesq type model. Part II: surf beat and swash oscillations for wave groups and irregular waves. *Coastal Engineering*, *32*(4), 289-319.

Madsen, P., and Warren, I. (1984). Performance of a numerical short-wave model. *Coastal Engineering*, *8*(1), 73-93.

Magne, R., Belibassakis, K., Herbers, T. H. C., Ardhuin, F., O'Reilly, W. C., and Rey, V. (2007). Evolution of surface gravity waves over a submarine canyon. *Journal of Geophysical Research*, *112*(C1), 1–12.

Mei, C., Rosales,R., and Akylas., T. (2006). Wave propagation. (Massachusetts Institute of Technology: MIT OpenCourseWare). Retrieved 12 February 2016 from, http://ocw.mit.edu

Peregrine, D. (1967). Long waves on a beach. *J. Fluid Mech.*, *27*(04), 815.

Rabinovich, A. B. (2009). Seiches and Harbour Oscillations. *Handbook of Coastal and Ocean Engineering*, 193–236.

Riezebos, H. (2014). *Validation of SWASH for wave-channel interactions* (Additional Master thesis). TU Delft.

Schäffer, H., Madsen, P., and Deigaard, R. (1993). A Boussinesq model for waves breaking in shallow water. *Coastal Engineering*, *20*(3-4), 185-202.

Smit, P., Zijlema, M., and Stelling, G. (2013). Depth-induced wave breaking in a non-hydrostatic, near-shore wave model. *Coastal Engineering*, *76*, 1-16.

Stansby, P., and Zhou, J. (1998). Shallow-water flow solver with non-hydrostatic pressure: 2D vertical plane problems. *International Journal For Numerical Methods In Fluids*, *28*(3), 541-563.

Stelling, G., and Duinmeijer, S. (2003). A staggered conservative scheme for every Froude number in rapidly varied shallow water flows. *International Journal For Numerical Methods In Fluids*, *43*(12), 1329-1354.

Stelling, G., and Zijlema, M. (2003). An accurate and efficient finite-difference algorithm for non-hydrostatic free-surface flow with application to wave propagation. *International Journal For Numerical Methods In Fluids*, *43*(1), 1-23.

Suzuki, T., Gruwez, V., Bolle, A., and Verwaest, T. (2012). Wave penetration into a shallow marina-case study for Blankenberge in Belgium. In *Book of abstracts of the 4th International Conference on the Application of Physical Modelling to Port and Coastal Protection-Coastlab12* (pp. 17-20).

Sutherland, J., Peet, A. and Soulsby, R. (2004) Evaluating the performance morphological models. *Coastal Engineering*, 51(8-9), pp. 917-939.

Sørensen, O., Schäffer, H., and Madsen, P. (1998). Surf zone dynamics simulated by a Boussinesq type model. Part III. Wave-induced horizontal nearshore circulations. *Coastal Engineering*, *33*(2-3), 155-176.

Sørensen, O., Schäffer, H., and Sørensen, L. (2004). Boussinesq-type modelling using an unstructured finite element technique. *Coastal Engineering*, *50*(4), 181-198.

The SWASH Team (2016). *SWASH User Manual – SWASH version 3.14*. Retrieved 15 April 2016, from http://swash.sourceforge.net

Thompson, E., Chen, H.,and Hadley, L. (1996). Validation of Numerical Model for Wind Waves and Swell in Harbors. *J. Waterway, Port, Coastal, Ocean Eng.*, *122*(5), 245-257.

Toledo, Y. (2013). The oblique parabolic equation model for linear and nonlinear wave shoaling. *J. Fluid Mech.*, *715*, 103-133.

Van den Bos, J., Verhagen, H., Zijlema, M., and Mellink, B. (2014).Towards a practical application of numercial models to predict wave-structure interaction: an initial validation.*Int. Conf. Coastal. Eng.*, *1*(34), 50.

Van der Ven, P. (2016). *Benchmark test of wave penetration in harbours: measurement report (Draft)*. Deltares.

Van Dongeren, A., Klopman, G., Reniers, A., Petis, H.(2002). High-quality laboratory wave generation for flumes and basins. *Proc. Of Waves.* San Francisco, California: ASCE, 2001. 1190-1199.

Van Mierlo, F. (2014). *Numerical modelling of wave penetration in ports*. Master thesis. TU Delft.

Van Vledder, G., and Zijlema, M. (2014). Non-hydrostatic wave modelling in partly sheltered harbour basins . *Int. Conf. Coastal. Eng.*, *1*(34), 11.

WAFO group. (2011). *WAFO- A MATLAB Toolbox for Analyses of Random Waves and Loads – Tutorial for version 2.5.* Lund, Sweden. Center for Math. Sci. Lund Univ.

Zijlema, M., and Stelling, G. (2005). Further experiences with computing non-hydrostatic free-surfa flows involving water waves. *International Journal For Numerical Methods In Fluids*, *48*(2), 169-197.

Zijlema, M., and Stelling, G. (2008). Efficient computation of surf zone waves using the nonlinear shallow water equations with non-hydrostatic pressure. *Coastal Engineering*, *55*(10), 780-790.

Zijlema, M., and Stelling, G., and Smit, P. (2011). SWASH: An operational public domain code for simulating wave fields and rapidly varied flows in coastal waters. *Coastal Engineering*, *58*(10), 992-1012.

Zwamborn, J. A., and Grieve, G. (1974). Wave attenuation and concentration associated with harbours. 14th ICCE, Copenhagen

Appendix A WAFO toolbox

The output of the numerical models SWASH and MIKE 21bw are exported as time series of water level elevations and are post processed with the WAFO-toolbox. '*WAFO (Wave Analysis for Fatigue and Oceanography) is a toolbox of MATLAB routines for statistical analysis and simulation of random waves and random loads'* (WAFO-group, 2011).

Three different MATLAB scripts were used from this toolbox for the post processing of data and are:

- *Dat2spec*: it estimates the spectral density from the data.
- *Spec2char*: evaluates spectral characteristics (Hm0, Tm-1,0 etc.) from spectral density.
- *Plotspec*: plots a spectrum from the spectral density.

A1 - Sensitivity smoothing function

The MATLAB script 'dat2spec' calculates the spectral density from the water level elevations. An input parameter is the so called 'lag size of the window function' (L). This parameter determines the smoothing of the wave spectra and for a smaller lag size (L) the estimate becomes smoother (WAFO-group, 2011).

In Figure A1-A3 wave spectra are plotted for different values of the lag size for different frequency ranges. It can clearly be seen that the smaller the value (L), the smoother the frequency spectra. Furthermore, the computed significant wave height from the spectral density is (almost) independent on the choice of (L) when the significant wave height is based on the integration of a large enough frequency range. However, if the significant wave height is based on a small frequency range as is the case for the Helmholtz modes, the computed significant wave height is very sensitive to the value of the lag size. From Figure A3 is follows that the significant wave height based on a small frequency range doubles for lag size values of 50,000 compared to 3,000.

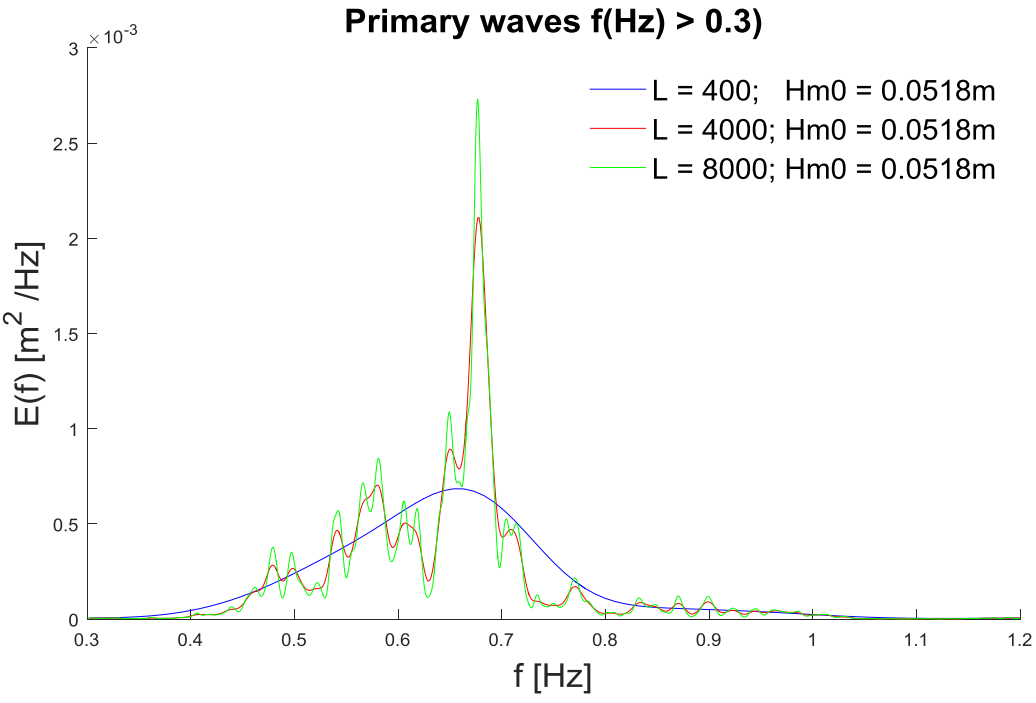

Figure A1. Frequency spectra of the primary wave energy for the harbour case, scenario T079 at wave gauge 22. The spectra are plotted for different lag sizes of the window function (L). Note that the Hm0 presented is based on frequencies larger than 0.3 Hz.

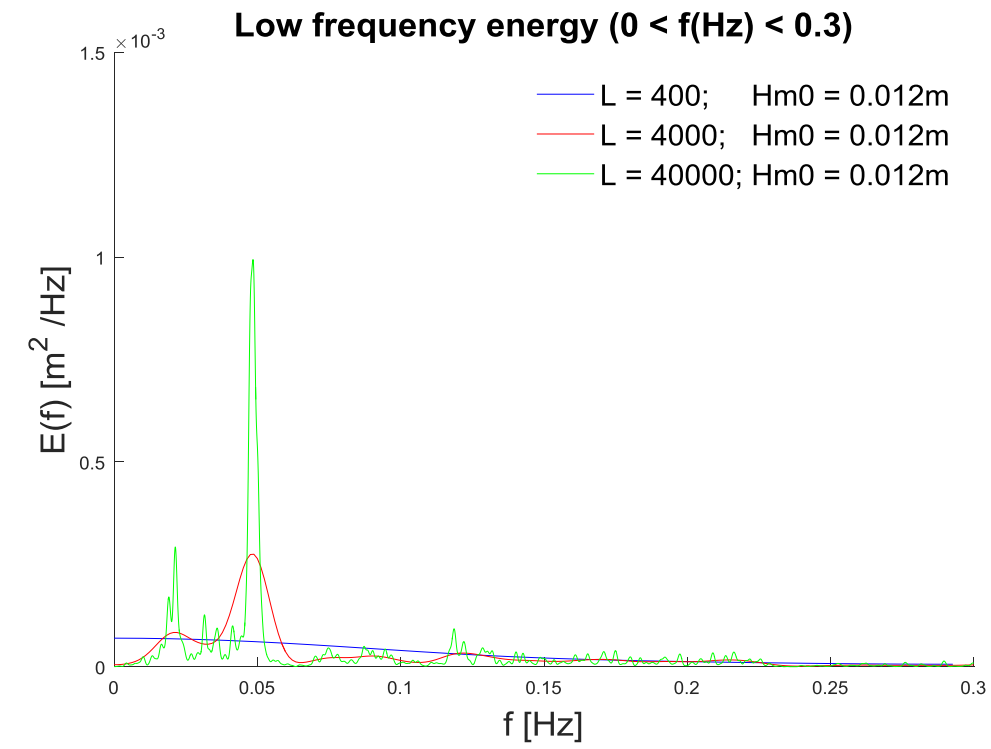

Figure A2. Frequency spectra of the low frequency energy for the harbour case, scenario T079 at wave gauge 22. The spectra is plotted for different lag sizes of the window function L. Note that the Hm0 presented is based on the frequency range between 0 Hz and 0.3 Hz.

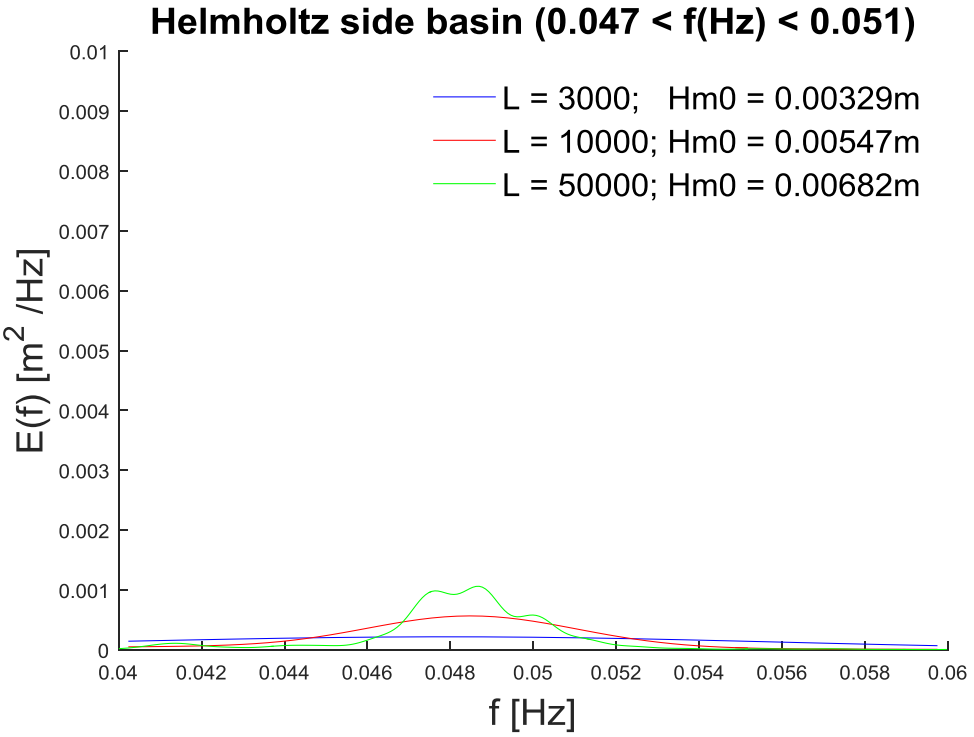

Figure A3. Frequency spectra for the frequency range between 0.04 Hz and 0.06 Hz for the harbour case, scenario T079 at wave gauge 22. The spectra are plotted for different lag sizes of the window function (L). Note that the Hm0 presented is based on the frequencies between 0.047 Hz and 0.051 Hz.

Appendix B Numerical simulations Case 1: Approach channel

B1 – Setup numerical model MIKE 21bw

Model layout and bathymetry

The layout of the physical model as presented in Section 5.2 was reconstructed and the bathymetry is included as much as possible. The navigation channel has the same slopes as in the physical model. However, the slopes of the breakwaters are not included in the bathymetry in order to run stable computations. Instead, the breakwaters were modelled as vertical (impermeable) walls (see also Section 3.1.2) with fifteen porosity layers placed in front of it. A porosity value of 0.83 was applied, leading to a reflection coefficient of 0.4.

In Figure B1 a 3D plot of the bathymetry is given. The vertical walls which represent the breakwater can clearly be seen. Note that the porosity and sponge layers are not included in the figure.

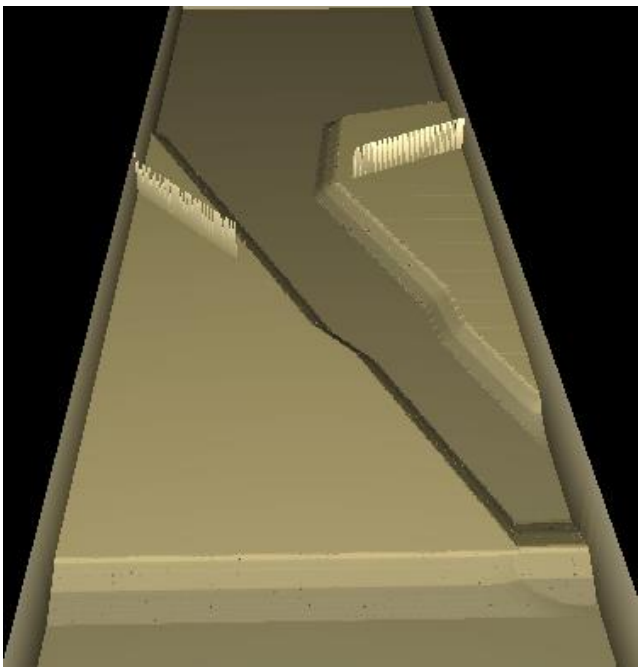

Figure B1. Bathymetry of the approach channel used in MIKE 21bw.

Wave generation

The waves are generated at the bottom of Figure B1 by means of an internal wave generation line. This line is placed just in front of a sponge layer so that waves only propagate into the domain of interest and reflected waves are dissipated by the sponge layer. Two different wave conditions were used and are given in Table 5.3. Moreover, the wave spectra imposed are identical to the spectra imposed during the physical experiment and can be seen in Figure B2 for scenario C1 and C2. Because of the kd limit in MIKE 21bw there is a minimum wave period the model resolves (for scenario C1 and C2: T_{min} = 5.32 s; f_{max}= 0.187 Hz). Therefore, the imposed wave spectra are truncated (Figure B2 in red) and a bias of -14% and -9% in significant wave height is already induced at the wave generation line for scenario C1 and C2, respectively. The mean wave direction of the incident waves has an orientation of 0° normal to the wave board. Further, a normal distributed directional spreading with 20° standard deviation was applied.

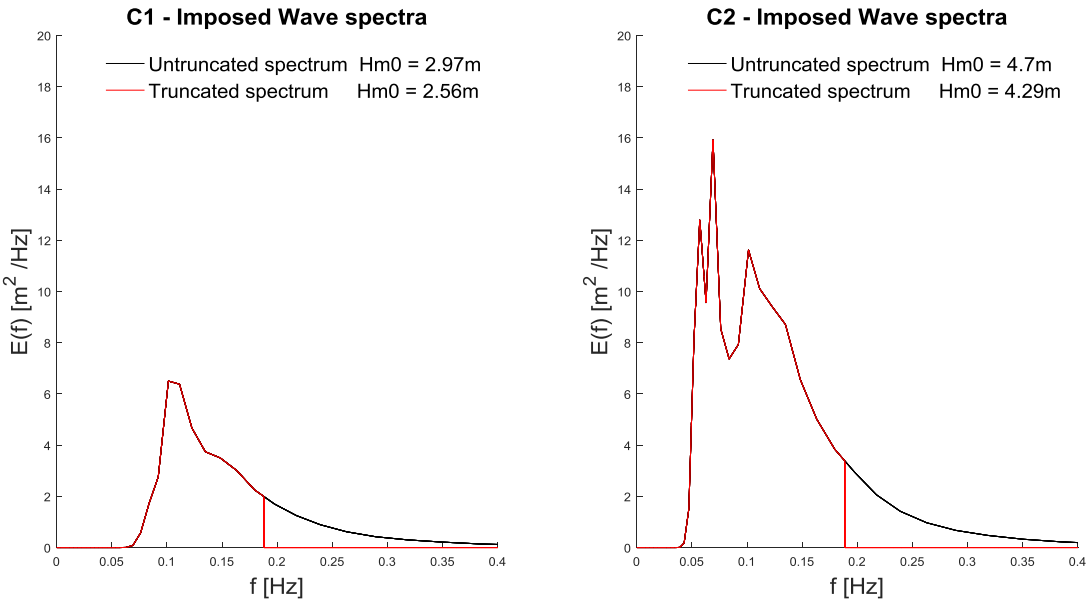

Figure B2. Imposed wave spectra during the physical experiment in black and the truncated spectra imposed in MIKE 21bw in red.

Wave breaking

For scenario C2 wave breaking has been switched on by including the dissipation term in the momentum equations with the concept of surface rollers (see Section 3.1.1). Further, all the default breaker parameters are used in the calculations and are:

- Roller form factor of 1.5
- Type of roller celerity: 3
- Roller celerity factor of 1.3
- Initial breaking angle: 20°
- Final breaking angle: 10°
- Half-time for cut-off roller
- Wave direction: 270°

Boundaries

The wave guiding walls at the side of the domain were modelled as land and the boundaries are therefore closed. Sponge layers are placed at the bottom and at the top of the computational domain and have a width of 300 m, corresponding to almost twice the deep water wave length.

Physical parameters

Bottom friction is included and is constant over the entire domain. The friction is specified by means of a Manning number of 0.019 ($m^{-(1/3)}\ s$).

Numerical parameters

For the computations use was made of the enhanced Boussinesq equations. Furthermore, the space discretisation of the convective terms was done by means of central differencing with simple upwinding at steep gradients and near land. This scheme was chosen to get stable computations, while minimizing the amount of numerical damping. A grid size of 3 m was used in x- and y-direction together with a time step of 0.05 s. With these values, the stability criteria needed were met (maximum Courant number of 0.5 and at least 35 time steps per wave period).

B2 – Setup numerical model SWASH

Model layout and bathymetry

The physical model layout had been reconstructed in SWASH and the bathymetry implemented is exactly the one used in the physical model. Further, the bathymetry has a resolution of 5 m x 5 m and SWASH subsequently interpolates so that the bathymetry has the same resolution as the computational grid.

The two breakwaters are modelled as porous structures with a porosity value of 0.45. The height of the structure and the stone size vary along the cross section of the breakwater. Therefore, the slopes of the breakwater are included, on the contrary to MIKE 21bw. The stone size is 0.65 m at the beginning of the slope and gradually decreases towards 0.2 m located at the crest of the breakwater.

Wave generation

Waves are generated by means of the same wave spectra as used in the physical model test. The imposed wave spectra for scenario C1 and C2 are plotted in Figure of B2 in black. The mean wave direction of the incident waves has an orientation of 0° normal to the wave board. Further, a normal distributed directional spreading with 20° standard deviation was applied.

Wave breaking

Although wave breaking is always included in the SWASH calculations, the breaking option was turned on to use the hydrostatic front approach as described in Section 3.2.1. This was done because the vertical resolution was low (2 vertical layers) and without this option wave breaking would be under-estimated.

Boundaries

A sponge layer with a width of 1500 m is placed at the North side of the domain in order to limit wave reflection as much as possible. At the wave guiding walls (East and West side), nothing was specified which means that SWASH models these boundaries as fully reflective.

Physical parameters

Bottom friction is included and is constant over the entire domain. The friction is specified by means of a Manning number of 0.019 ($m^{-(1/3)}\ s$) and is identical to the value used in MIKE 21bw.

Numerical parameters

A rectangular uniform computational grid in a Cartesian coordinate system was implemented with a horizontal resolution of 3 m x 3 m which leads to 46 grid points per deep water wave length. Two vertical layers were used which leads, according to the SWASH user manual, to a maximum kd ratio of 7.7. The resolution was the same as used by Dusseljee et al. (2014) and is a compromise between accuracy and computational time.

A maximum courant number of 0.7 was applied which resulted in a time step of 0.025 s. Further, the Keller box scheme is applied because the vertical resolution is low together with a momentum conservative scheme which is recommended by the SWASH user manual in case of simulating breaking waves.

B3 – Results

In this section the results are presented for scenario C1 and C2 at all the wave gauges. Figure B3 shows the spatially variation of the significant wave height together with the locations of the GRSM and the WHM gauges. In Figure B4 the computed significant wave height and energy period are presented computed at all the wave gauges based on the cut-off and total spectra. Furthermore, all the frequency spectra are presented in Figure B5 and B6 for scenario C1 and C2, respectively.

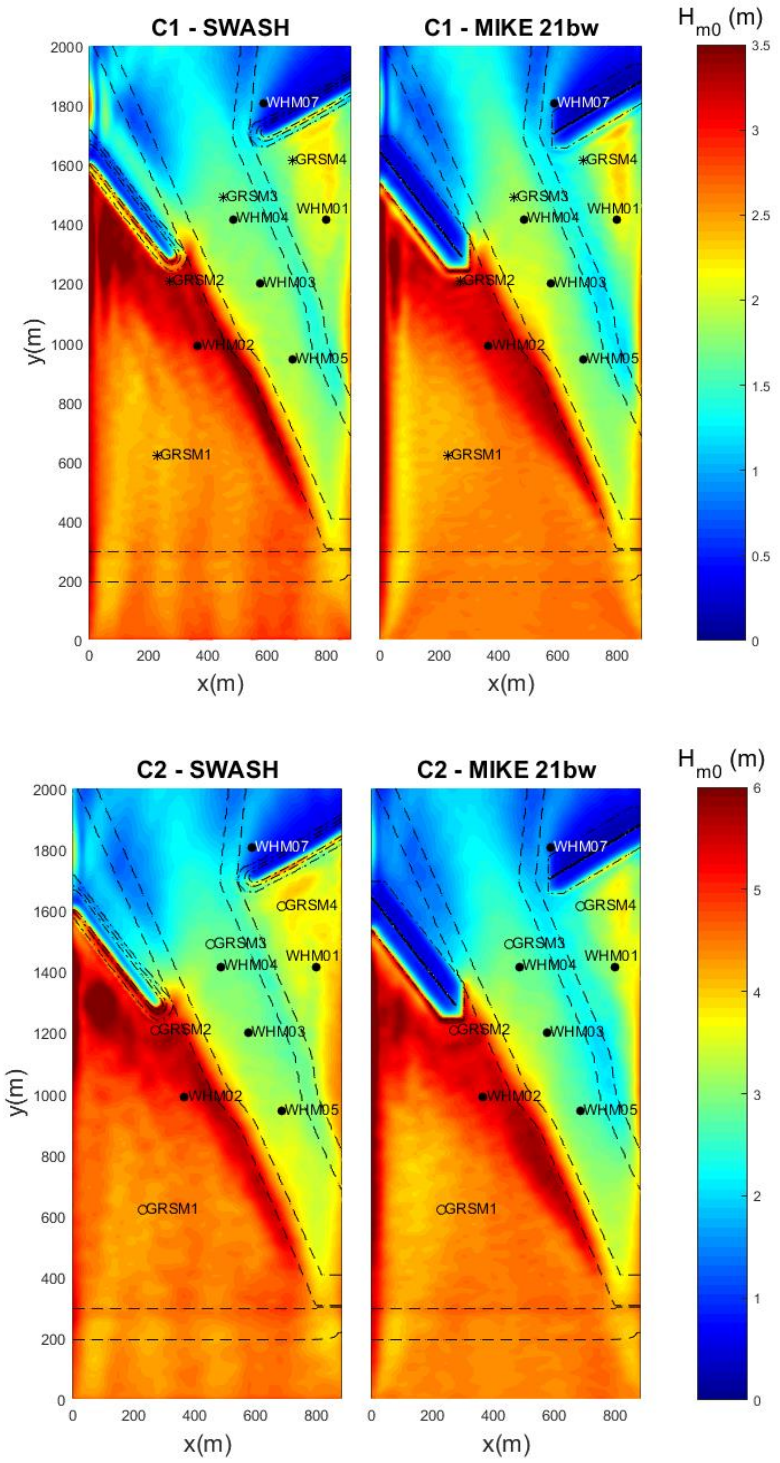

Figure B3. Computed significant wave height by SWASH (left) and MIKE 21bw (right) over the computational domain for scenario C1 (top figures) and scenario C2 (bottom figures).

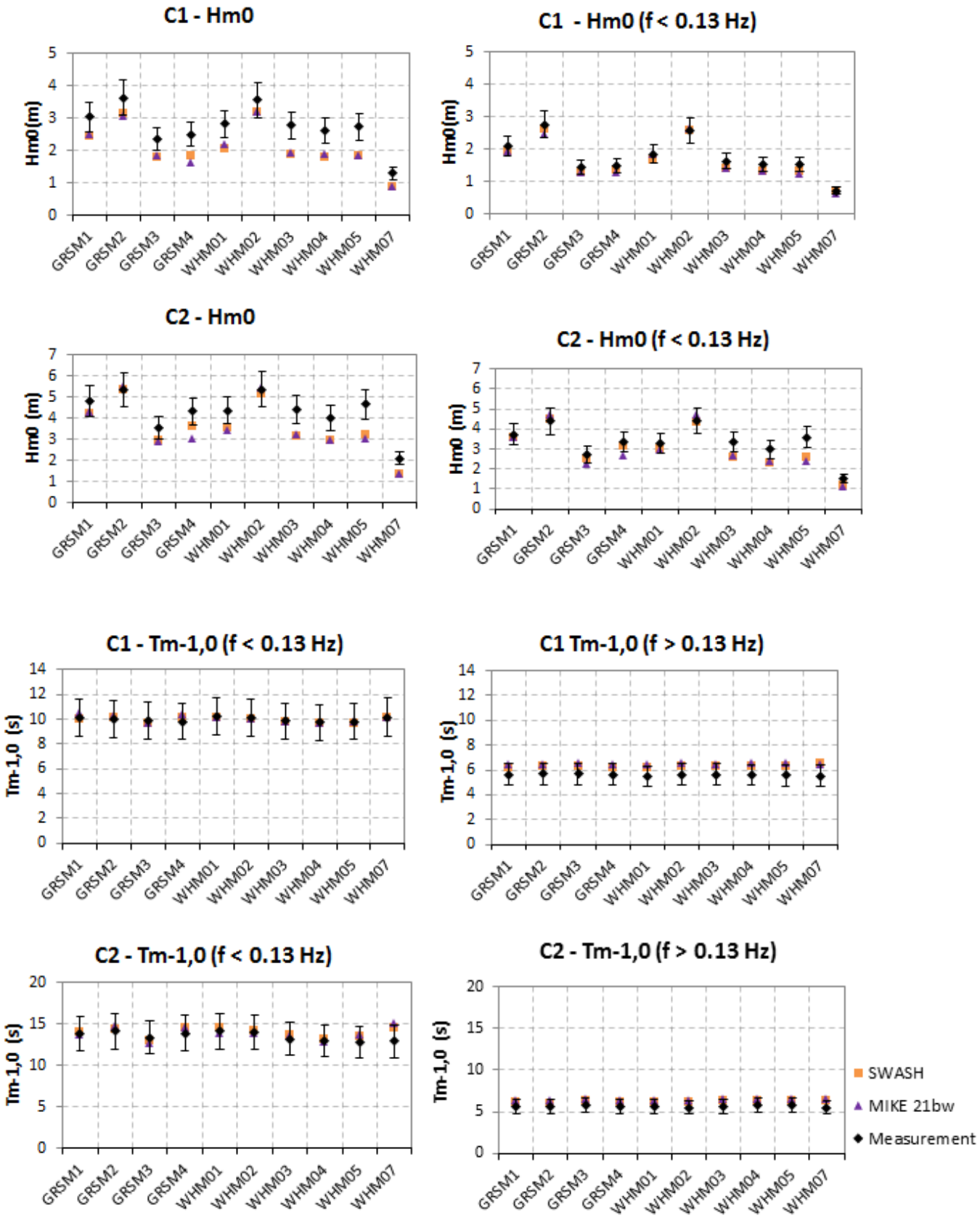

Figure B4. Computed significant wave height and energy period based on the total and cut-off spectra at all the wave gauges for scenario C1 and C2. Note that the bars indicate a (fixed) measurement deviation of ±15%.

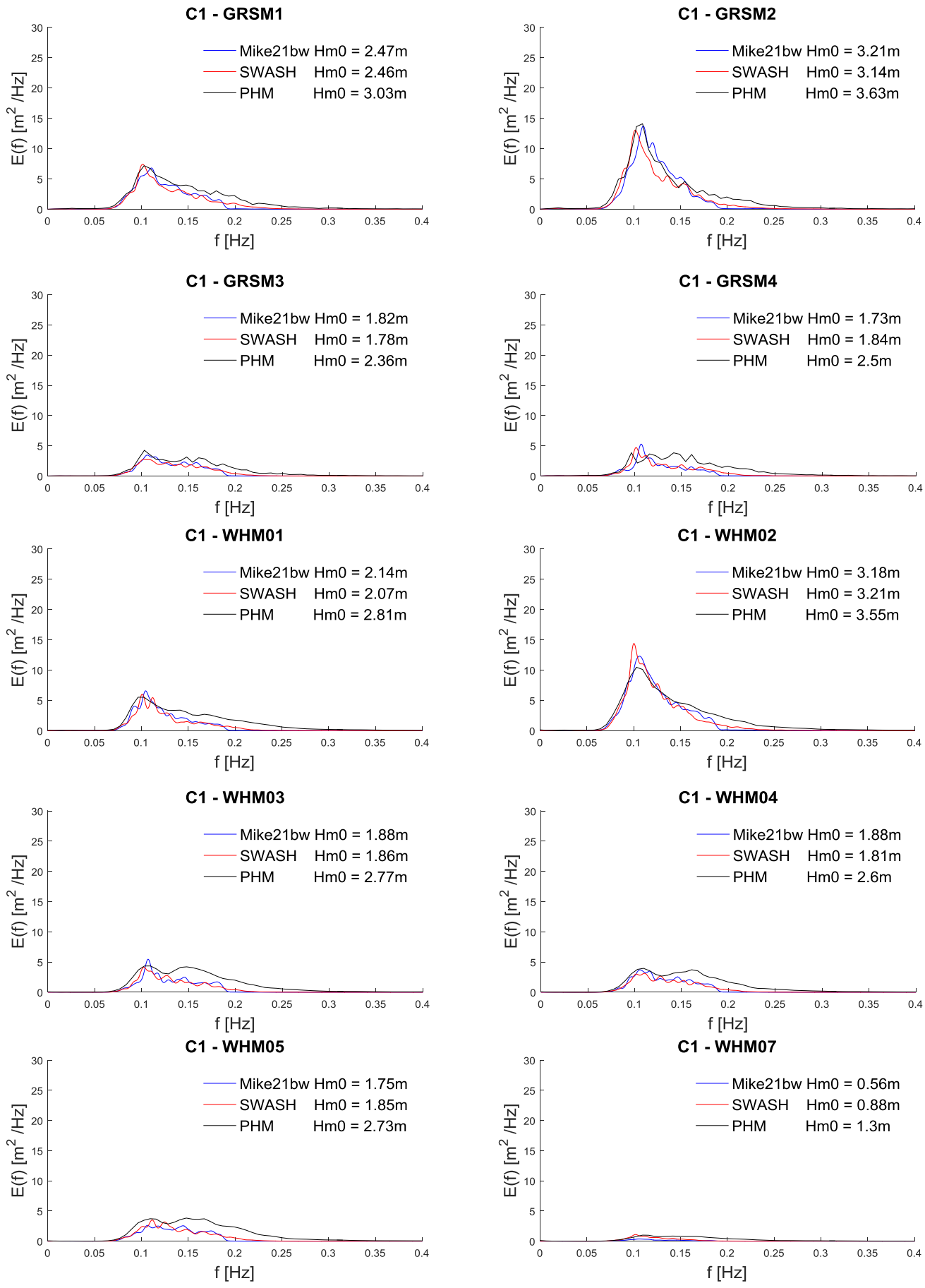

Figure B5. Scenario C1: frequency spectra at the GRSM and WHM wave gauges.

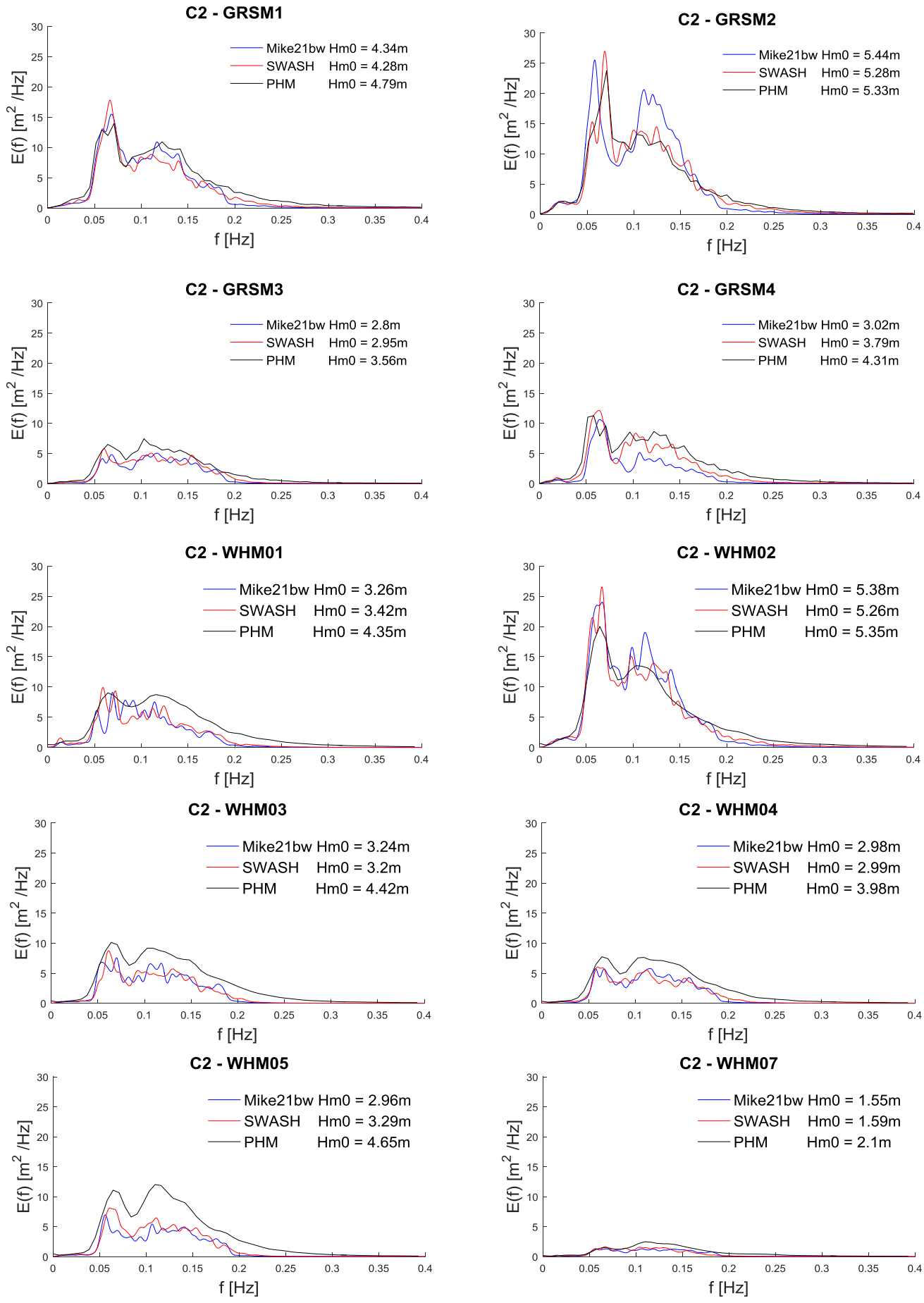

Figure B6. Scenario C2: frequency spectra at the GRSM and WHM wave gauges.

Appendix C Numerical simulations Case 2: Harbour

C1 – Setup numerical model MIKE 21bw

Model layout and bathymetry

The layout of the physical model was reconstructed as much as possible in MIKE 21bw. All the slopes however are not included in the bathymetry in order to run stable computations. In Figure C1 the original bathymetry used in the physical experiment can be seen together with the bathymetry used in MIKE 21bw for scenario T079. Scenario T035 used the same bathymetry but without the breakwater. From this figure the differences in schematisation due to the fact that slopes cannot be fully included in MIKE 21bw can clearly be seen, in particular for the breakwater. Runs including part of the slope of the breakwater were attempted, but due to numerical instabilities this was not considered any further.

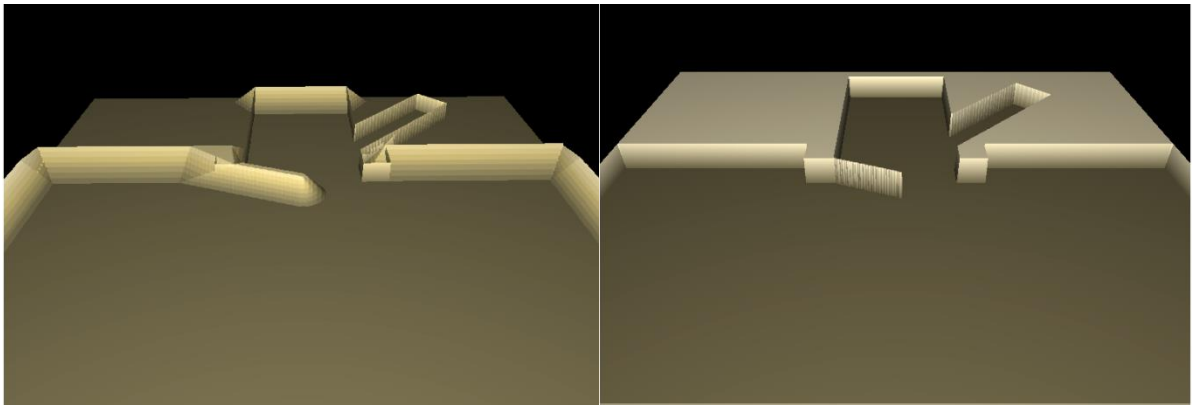

Figure C1. Left figure shows a 3D plot of the original bathymetry used in the physical experiment (and SWASH). The right figure presents the bathymetry as used in MIKE 21bw. Both figures are for scenario T079.

Scale

Simulations were carried out on physical model scale which is identical to the scale used in the physical experiment and on a prototype scale, which is Froude scaled at scale of 1:20.

Wave generation

The incoming waves are generated by imposing time series of water level elevation of the incoming waves at the wave generation line. These time series were provided and were calculated from the motion of the wave board. In this manner the realisation of the JONSWAP spectrum is the same in the physical and numerical model.

Wave breaking

No wave breaking is included in the simulations because for the considered scenarios wave breaking was not significant and excluding wave breaking enhances stability.

Boundaries

The boundaries follow from the bathymetry and are all closed. The reflection coefficients assigned are identical to the ones determined by Van Mierlo (2014) and are:

- Breakwater: 0.3
- Gravel slopes: 0.2
- Vertical walls: 1

The simulations in physical model scale resulted in numerical instabilities when using a reflection coefficient of 1 for the vertical walls. Therefore, a reflection coefficient of 0.9 was used.

Using the MIKE 21bw toolbox, the porosity values needed to give the desired reflection coefficients were calculated. In Figure C2 the porosity map is shown for scenario T079 for the simulation on physical model scale and Figure C3 for prototype scale. The main difference is that multiple porosity layers are specified before the concrete walls in physical model scale, on the contrary to prototype scale. Further, slightly different porosity values were needed at the gravel slopes and the breakwater in order to get the same reflection coefficient.

Sponge layer

The computational domain was extended by 50 grid cells at the wave generation line which is the width of the sponge layer applied. This width corresponds to almost two times the wave length in physical model and prototype scale.

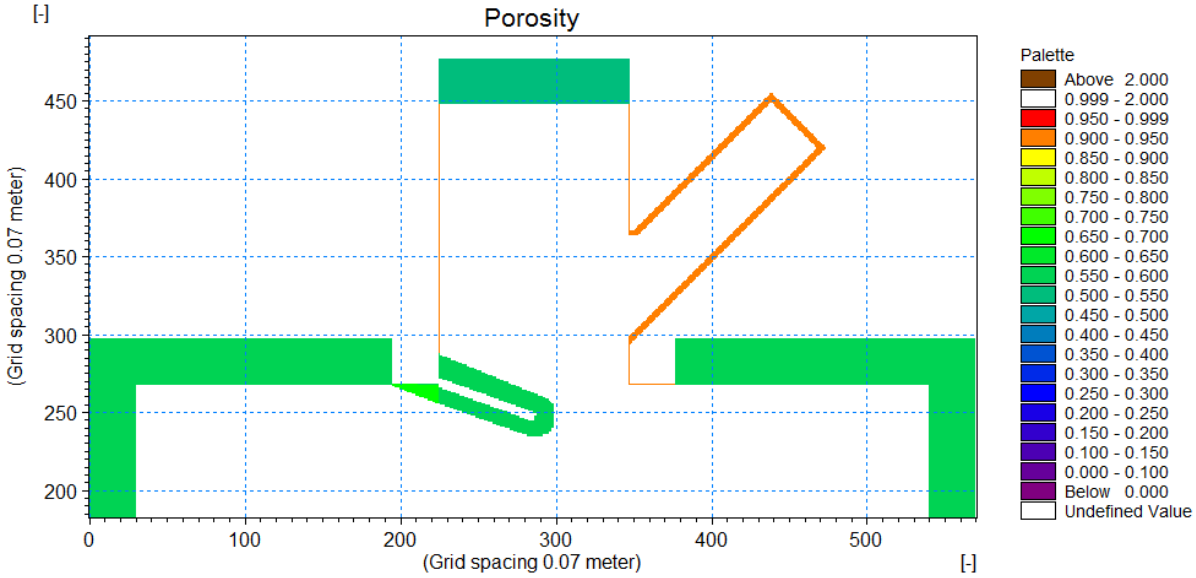

Figure C2. Porosity map for scenario T079 in physical model scale.

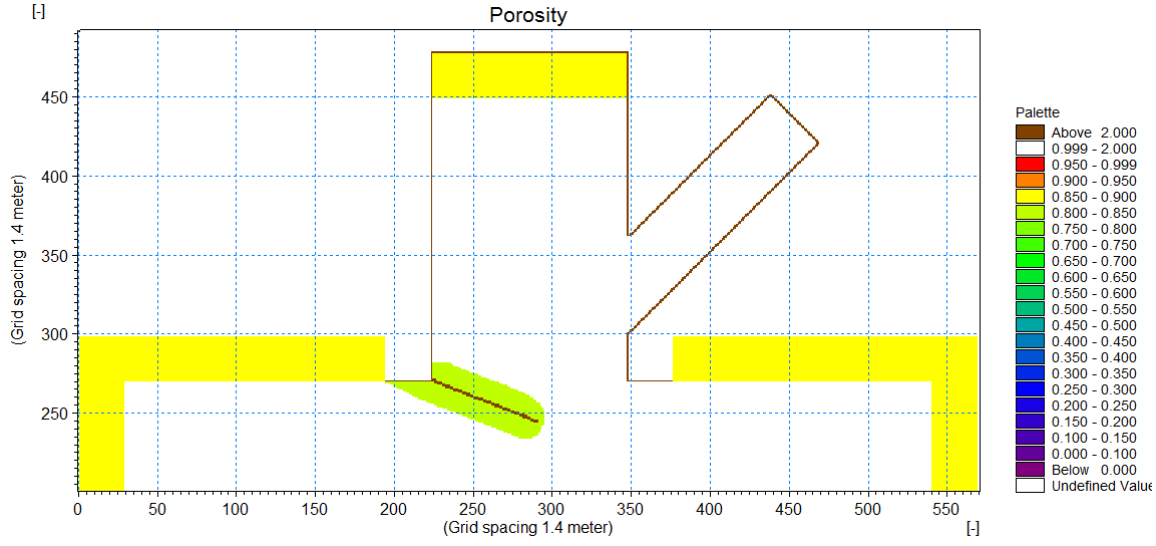

Figure C3. Porosity map for scenario T079 in prototype scale.

Physical parameters
No bottom friction is included, because the distance over which the waves travel is relatively small, therefore the effect of bottom friction is very small.

Numerical parameters
For the computations use was made of the enhanced Boussinesq equations. Furthermore, the space discretisation of the convective terms was done by means of central differencing with simple upwinding at steep gradients and near land. This scheme was chosen to get stable computations while minimizing the amount of numerical damping.

A resolution of 0.07 m was used in x- and y- direction in physical model scale. For the prototype scale, a resolution of 1.4 m was used. However, it is important to note that the amount of grid points in both scales are the same. In addition, the amount of grid points per wave length are also identical, see Table C1.

A time step of 0.005 s and 0.02 s were chosen for the simulations in physical model and prototype scale, respectively. With these time steps the stability criteria were met (maximum Courant number of 0.5 and at least 35 time steps per wave period).

Table C1. Parameters in physical model and prototype scale for scenario T079.

	Physical model scale	**Prototype scale**
Peak period (s)	1.49	6.663482573
Frequency (Hz)	0.67114094	0.150071676
Angular frequency (radian/s)	4.216778523	0.942900342
Water depth (m)	0.44	8.8
Wave number (radian/m)	2.3425	0.1171
Wave length (m)	2.682177161	53.65499573
Grid size (m)	0.07	1.4
Grid points per wave length	38.31681659	38.32499695

C2 – Setup numerical model SWASH

Model layout and bathymetry
The bathymetry of the physical model was reconstructed in SWASH and is shown in Figure C1 (left panel). The breakwater and the gravel slopes are modelled as porous structures and on the contrary to MIKE 21bw, the slopes are included and have the correct steepness. A stone size of 150 mm was used for the gravel slopes and 30 mm for the breakwater. Moreover, a porosity value of 0.4 was applied at the gravel slopes and the breakwater. The vertical concrete walls were also schematised as porous structures and have a stone diameter of 1 mm and a porosity of 0.001.

Scale
Simulations were carried out on physical model scale which is identical to the scale used in the physical experiment and on a prototype scale, which is Froude scaled with a scale of 1:20.

Wave generation
The incoming waves are generated by imposing time series of water level elevation of the incoming waves at the wave generation line. These time series were provided and were calculated from the motion of the wave board. In this manner the realisation of the JONSWAP spectrum is the same in the physical and numerical model.

Wave breaking
The hydrostatic front approach to model wave breaking in case of a coarse vertical resolution was not used for the simulations because no significant wave breaking occurred, i.e. the waves are far away from their breaker limit.

Boundaries
The outer boundaries are modelled as closed and the internal boundaries follow from the bathymetry.

Physical parameters
No bottom friction is included, because the distance over which the waves travel is relatively small, therefore the effect of bottom friction is very small.

Numerical parameters
A rectangular uniform computational grid in a Cartesian coordinate system had been implemented with a horizontal resolution of 0.07 m x 0.07 m in physical model scale and 1.4 m x 1.4 m in prototype scale. This leads to 37 grid points per wave length for both scales. Note that the amount of grid points in physical model and prototype scale are identical. Furthermore, two vertical layers with equal thickness were used which leads, according to the SWASH user manual, to a maximum kd ratio of 7.7.

A maximum courant number of 0.5 was applied which led to a time step of 0.005 s and 0.02 s in physical model and prototype scale, respectively. In addition, the default momentum conservative schemes were applied which are a central differencing scheme for the horizontal advection terms and an upwind scheme for the vertical advection terms.

C3 – Schematisation breakwater MIKE 21bw

Length breakwater

Because MIKE 21bw needs a minimum water depth in order to run stable computations, the slopes of the breakwaters could not be included in the bathymetry, see also Chapter 3.1.2. Therefore, the breakwater was modelled as a vertical wall with porosity layers in front. Because the slopes at the head of the breakwater are not modelled, it is not arbitrary what length the breakwater should have.

Two different lengths of the breakwater were tested which can be seen in Figure C4. One schematisation is where the vertical wall ends at the beginning of the slope above the still water level (length 1). The second length was longer and the vertical wall ends where the slope crosses the still water level (length 2).

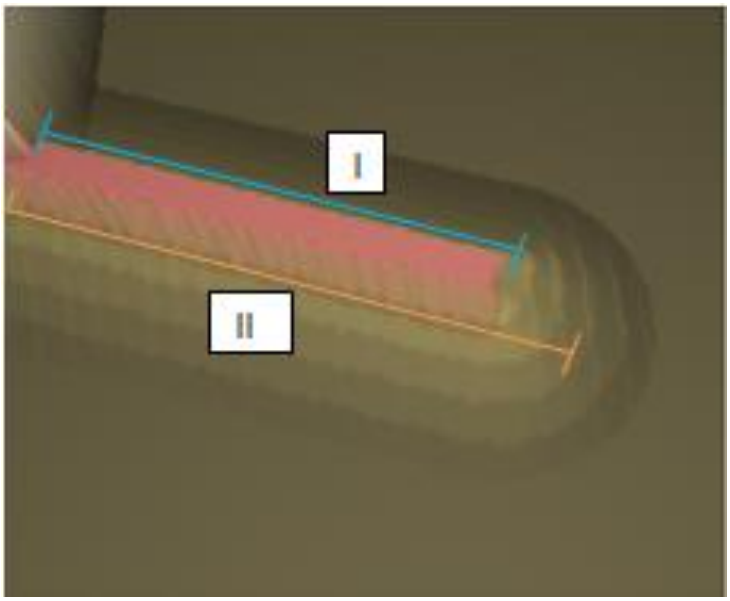

Figure C4. Screenshot of the breakwater including the slopes and the schematisation in MIKE 21bw in pink. The two different lengths used in the test runs are given in blue (1) and orange (2).

The results are presented in Figure C5 by means of a spatially varying significant wave height over the computational domain. The main difference between the two breakwater lengths is observed at the wave gauges 26, 11, 27 and 12.

A steep gradient in significant wave height can be observed directly behind the tip of the breakwater towards the end of the main basin. This line moves a bit to the right or left, depending on the length of the breakwater. Therefore, the wave gauges mentioned above are affected most. The influence on the other wave gauges was almost negligible.

Length 1 resulted in a large over-estimation at the wave gauges 26, 11, 27 and 12, indicating that the length of the breakwater was taken to short. The results of length two were much better and therefore this length was used in the model runs.

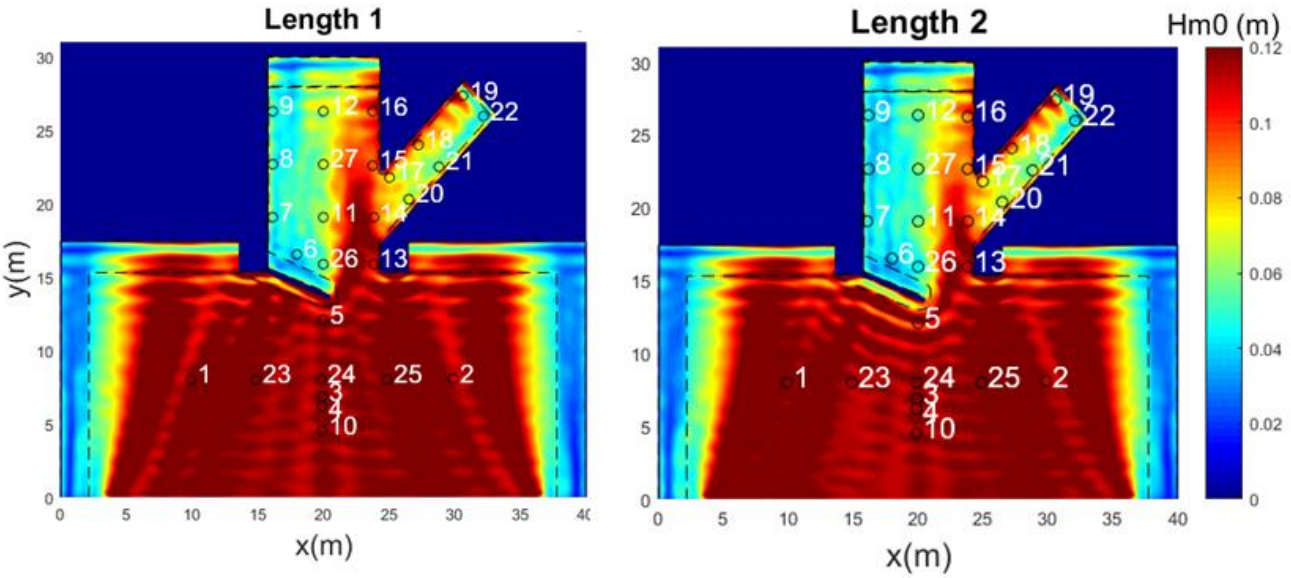

Figure C5. Spatial variation of the significant wave height for two different breakwater lengths. The different lengths can be seen in figure C4

Transmission breakwater

The breakwater was modelled as an impermeable structure without any transmission. However, in the physical experiment there was some transmission, although the actual amount is unknown.

Multiple runs were performed where the breakwater was schematised as a permeable structure. With the MIKE 21bw toolbox, a graph was calculated which shows the transmission coefficient as a function of the porosity, for 48 porosity layers, corresponding to a width of 3.36 meter. A transmission coefficient of 10% was assumed for the breakwater and from the computed graph it followed that a porosity value of 0.52 should be applied. The model runs resulted in a large over-estimation of the significant wave height inside the main basin of the harbour and it seemed that the actual transmission through the breakwater was larger than the 10% predicted from by the MIKE 21bw toolbox.

In order to test the actual transmission of the breakwater with the estimated transmission from the MIKE 21bw toolbox, a simple model was setup with an uniform constant water depth over the domain without any structures. Porosity layers are placed in the middle of the domain with a width corresponding to the width of the breakwater (48 layers). Further, at the bottom and at the top sponge layers were applied, see Figure C6.

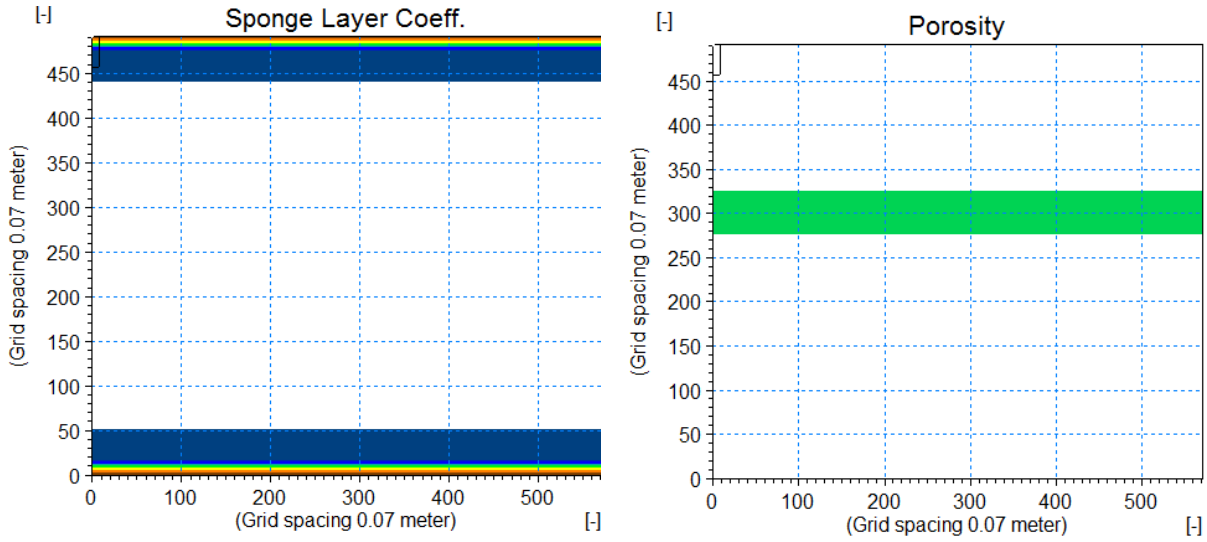

Figure C6. Setup of the numerical model to test the transmission of the breakwater. The left figure shows the applied sponge layers, while the right figure presents the used porosity layers.

Different porosity values were applied for the porosity layers and the results are presented in Table C2. It was found that the actual transmission is a factor 2-14 higher than the computed graph than the MIKE 21bw toolbox predicts. This is because the transmission coefficient calculated by the toolbox is based on one significant wave height and wave period, while in the actual simulations a wide range of wave heights and periods are present.

Because of the high over-estimation when including transmission of the breakwater, the breakwater was schematised as an impermeable structure, excluding transmission. This is not thought of as a major limitiation, because the actual transmission of the breakwater in the physical experiment was most likely small.

Table C2. Estimated and observed transmission coefficient for different porosity values.

Porosity value	Estimated transmission graph (Mike 21bw toolbox)	Observed transmission test
0.29	0.004	0.111
0.35	0.011	0.151
0.45	0.047	0.232
0.47	0.061	0.264
0.5	0.086	0.301
0.52	0.107	0.315
0.575	0.187	0.368

C4 – Results T035 physical model scale

In this section the results are presented for scenario T035 in physical model scale which is identical to the scale of the physical experiment. Furthermore, the breakwater in front of the harbour is not present in this scenario. In Figure C7 the spatial variation of the significant wave height is presented, followed by the comparison of the significant wave height and energy period based on different frequency ranges in Figures C8 and C9. In Figures C10 and C11 the frequency spectra at all the wave gauges are presented for the low frequency energy (f < 0.3 Hz) and for the primary wave energy (f > 0.3 Hz), respectively.

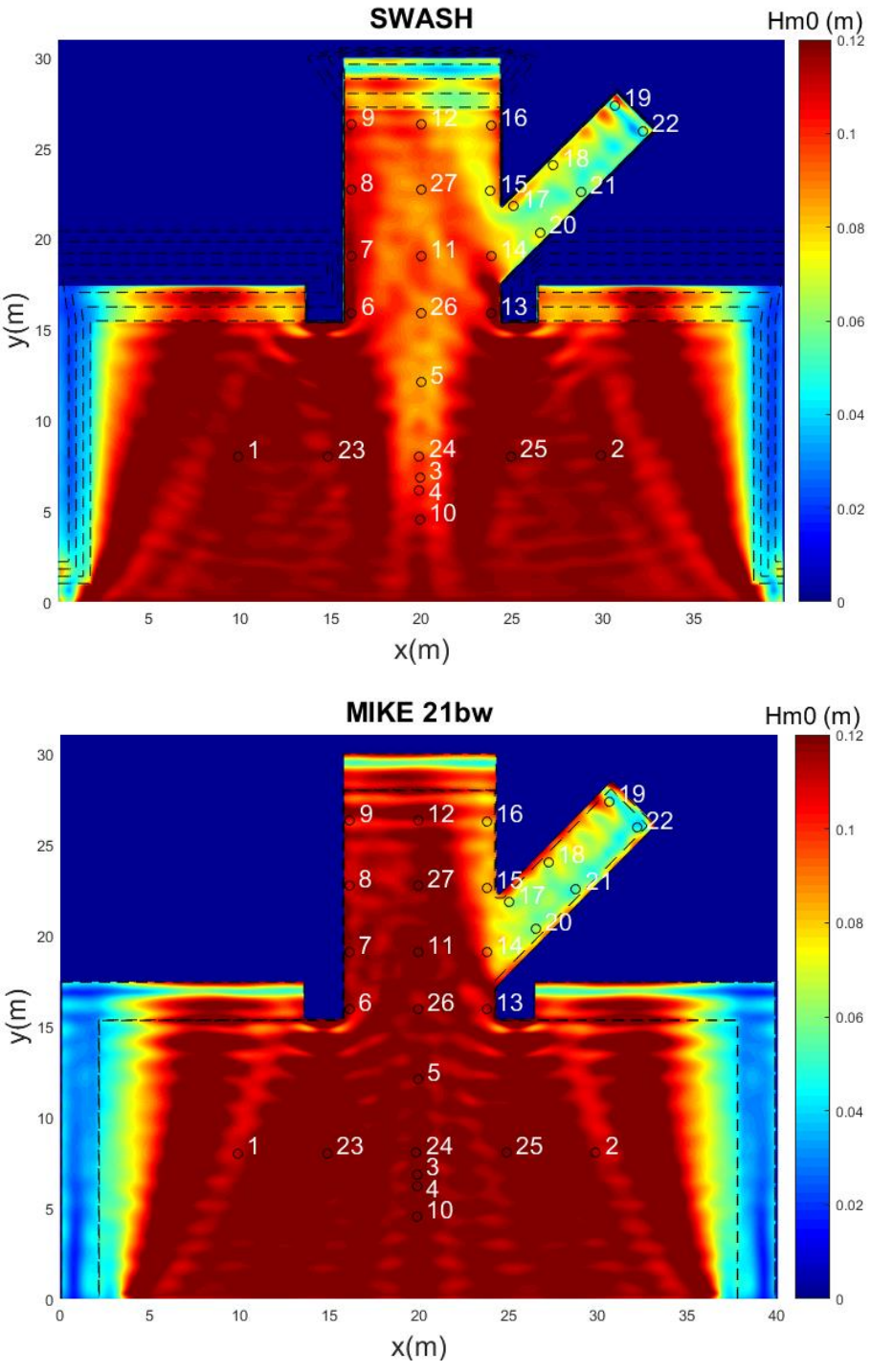

Figure C7. Spatial variation of the significant wave height (Hm0) for scenario T035 in physical model scale.

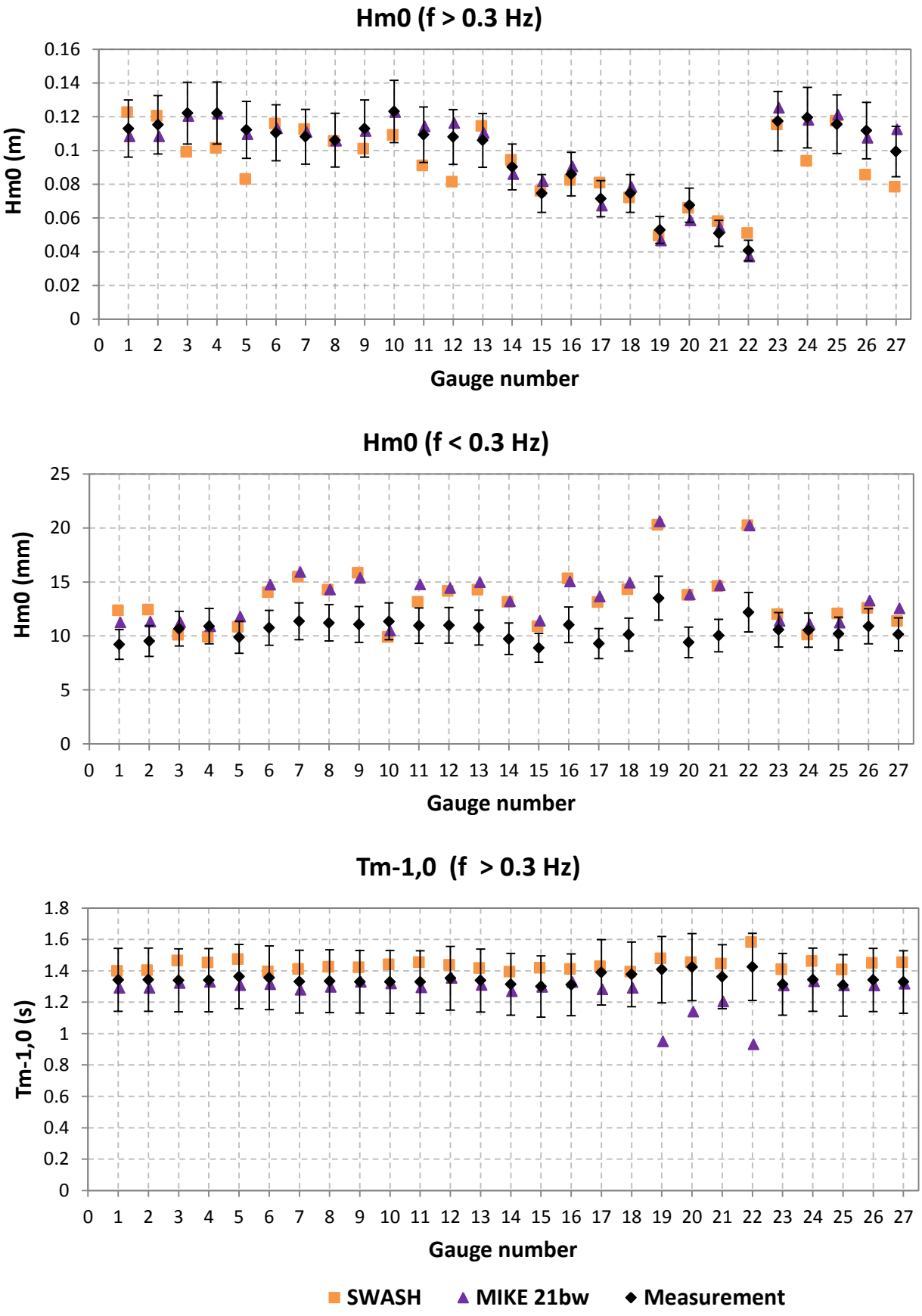

Figure C8. Comparison of the significant wave height (Hm0) and energy period (Tm-1,0) based on different frequency ranges. Note that the bars indicate a (fixed) measurement deviation of ±15%.

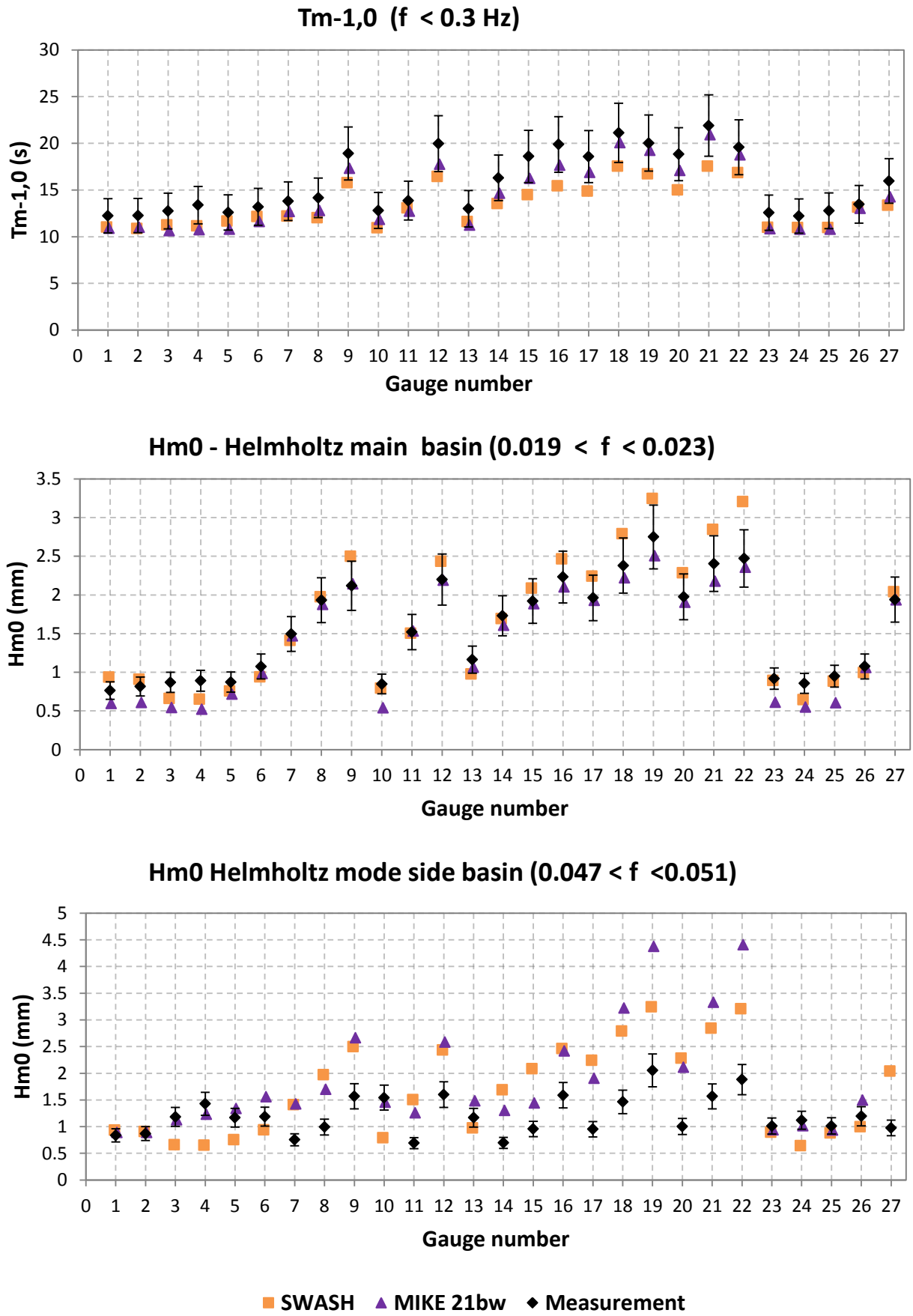

Figure C9. Comparison of the significant wave height (Hm0) and energy period (Tm-1,0) based on different frequency ranges. Note that the bars indicate a (fixed) measurement deviation of ±15%.

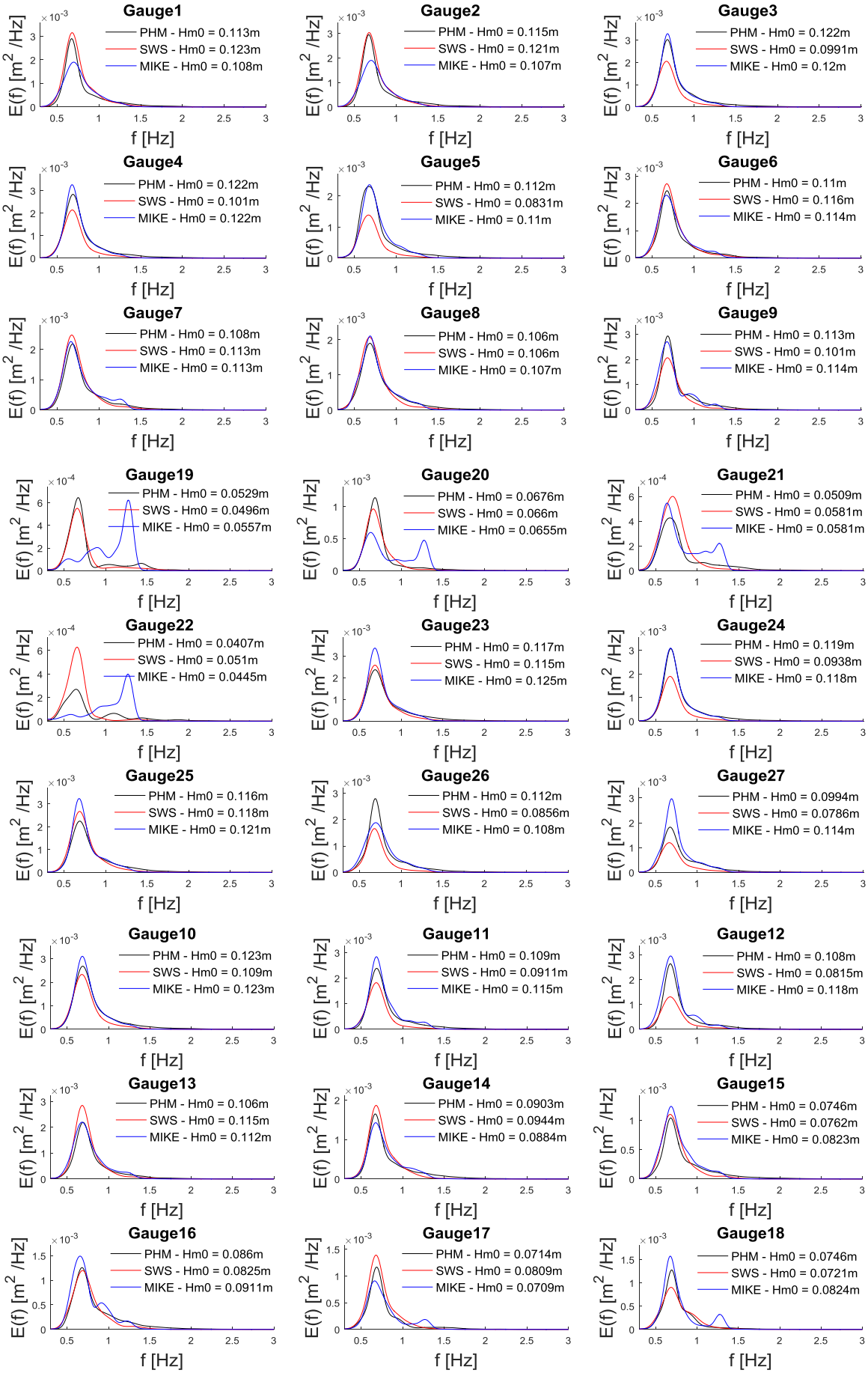

Figure C10. Frequency spectra for the primary wave energy. Note that the significant wave height (Hm0) is based on frequencies larger than 0.3 Hz.

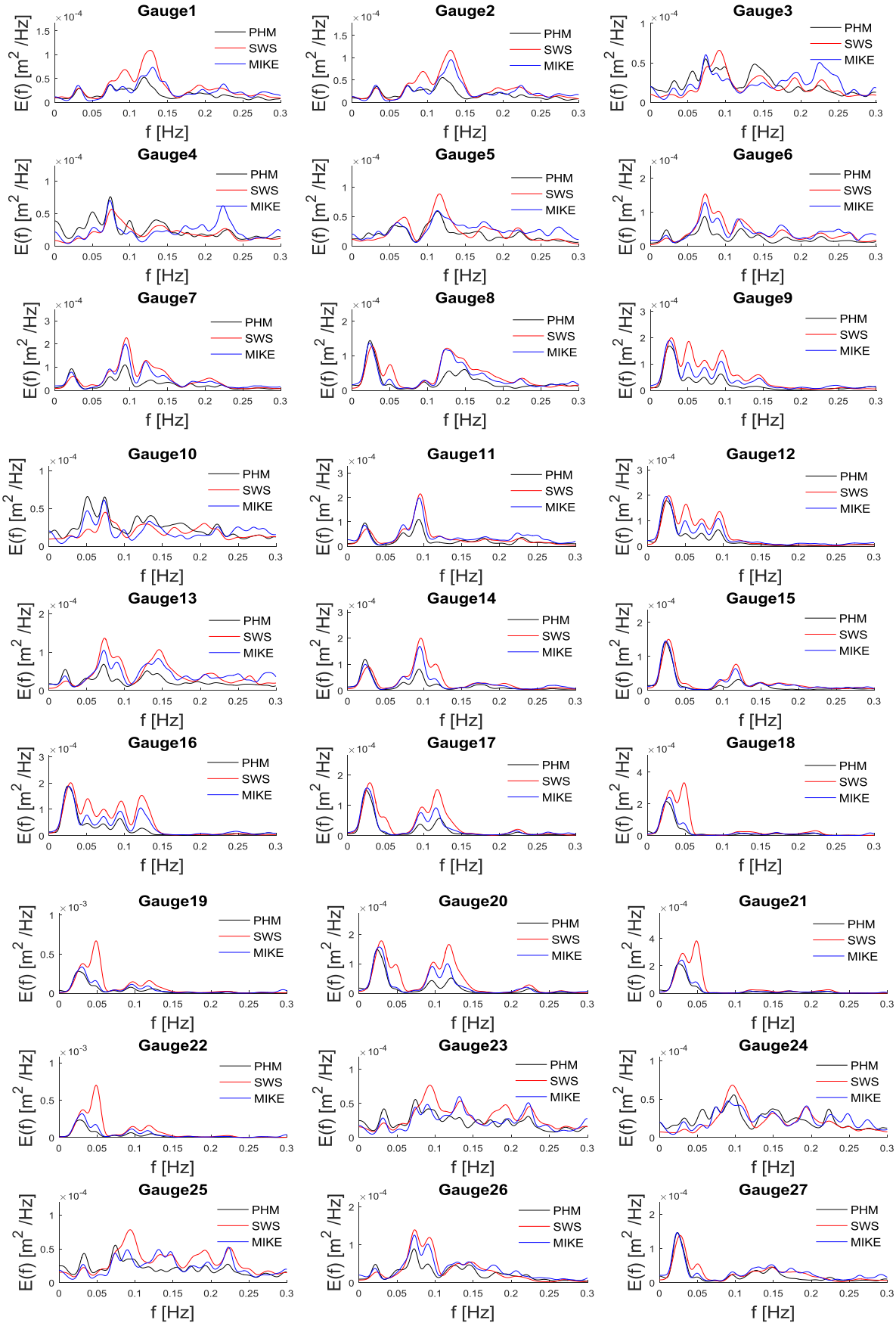

Figure C11. Frequency spectra of the low frequency energy (f < 0.3 Hz).

C5 – Results T079 physical model scale

The results for scenario T079 which includes the breakwater is presented in this section. Further, the scale is identical to the one of the physical model test. In Figure C12 the spatial variation of the significant wave height is presented, followed by the comparison of the significant wave height and energy period based on different frequency ranges in Figures C13 and C14. Finally, in Figures C15 and C16 the frequency spectra at all the wave gauges are shown for the primary wave energy (f > 0.3 Hz) and low frequency energy (f < 0.3 Hz).

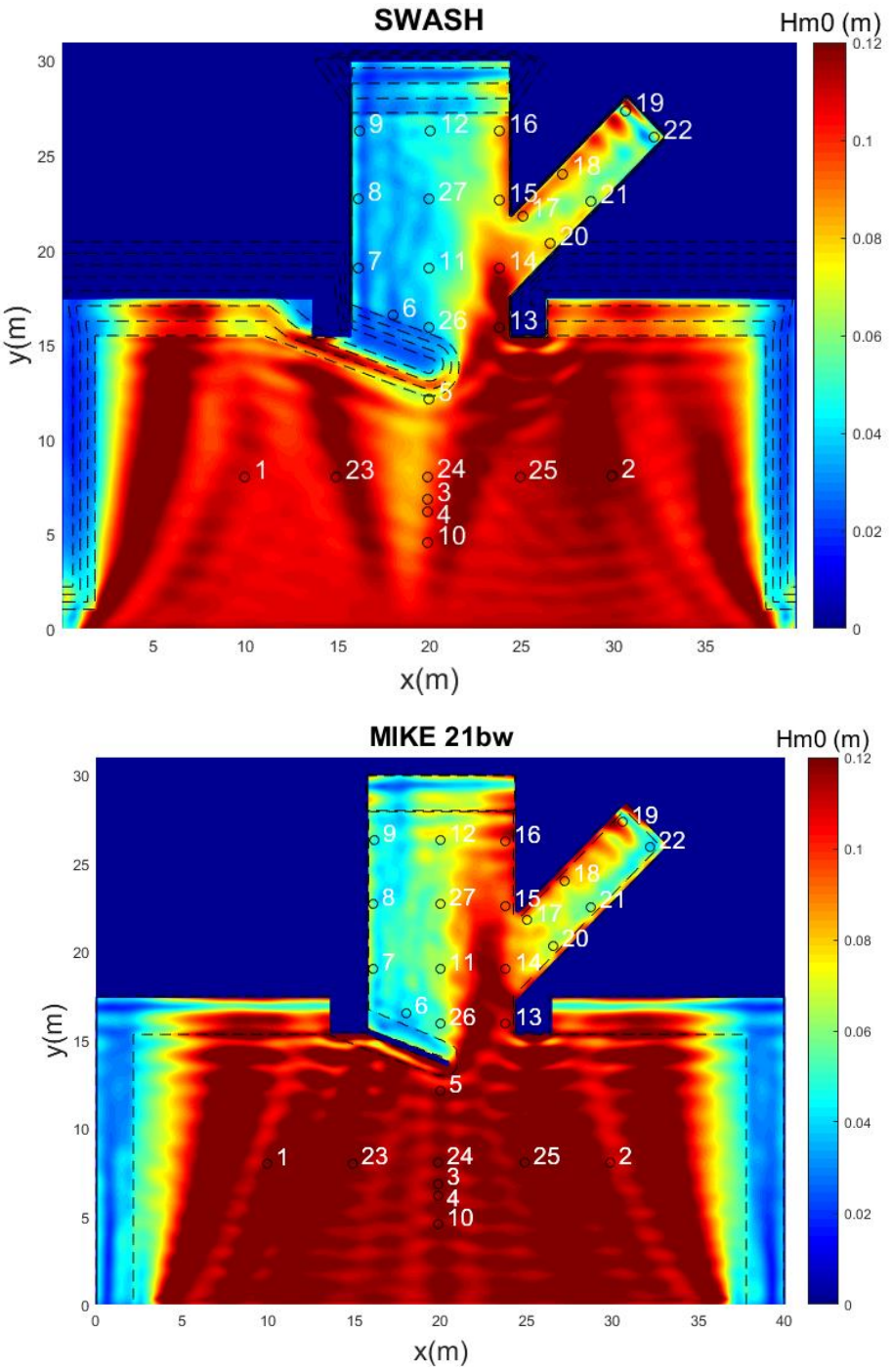

Figure C12. Spatial variation of the significant wave height (Hm0) for scenario T079 in physical model scale.

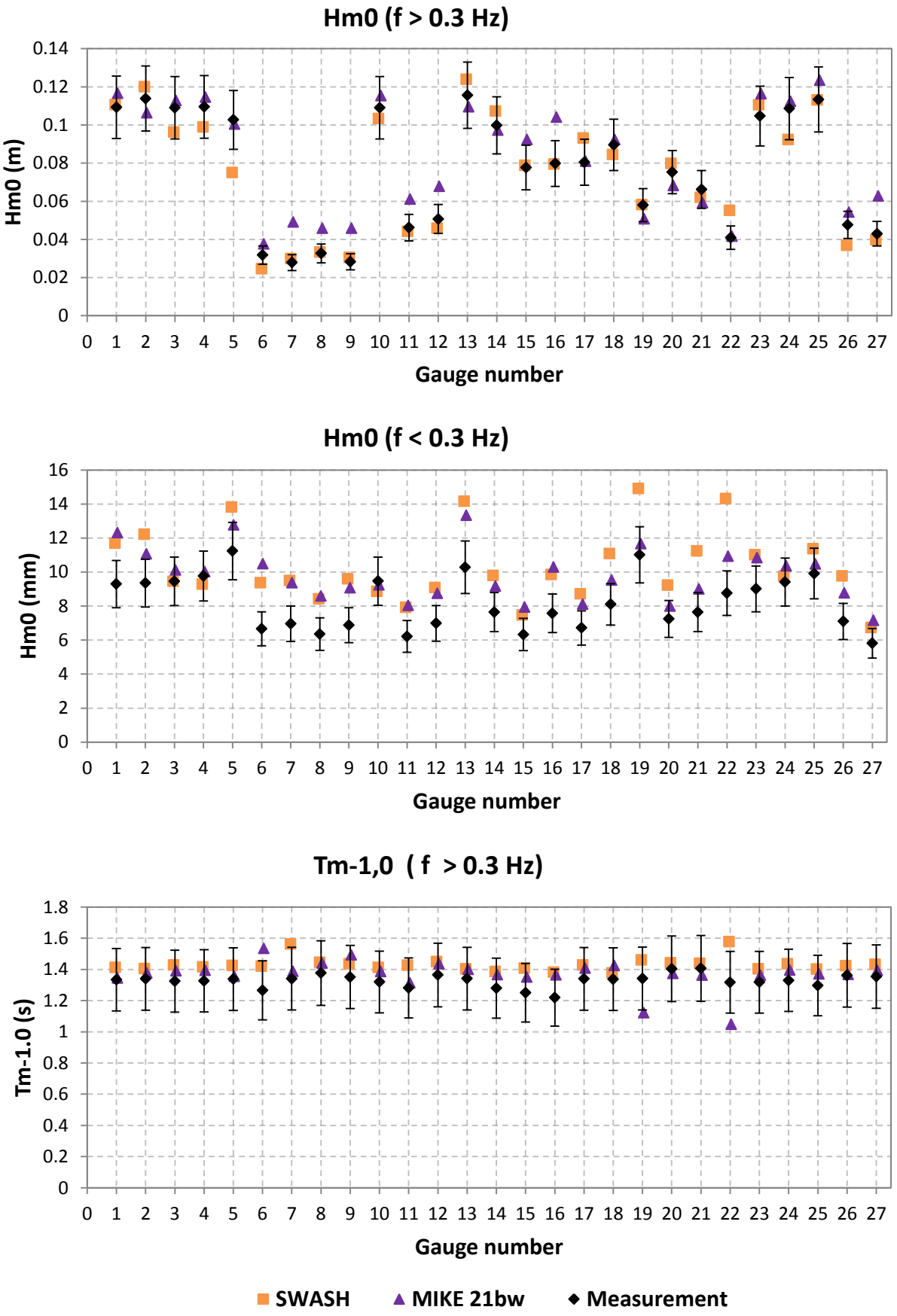

Figure C13. Comparison of the significant wave height (Hm0) and energy period (Tm-1,0) based on different frequency ranges. Note that the bars indicate a (fixed) measurement deviation of ±15%.

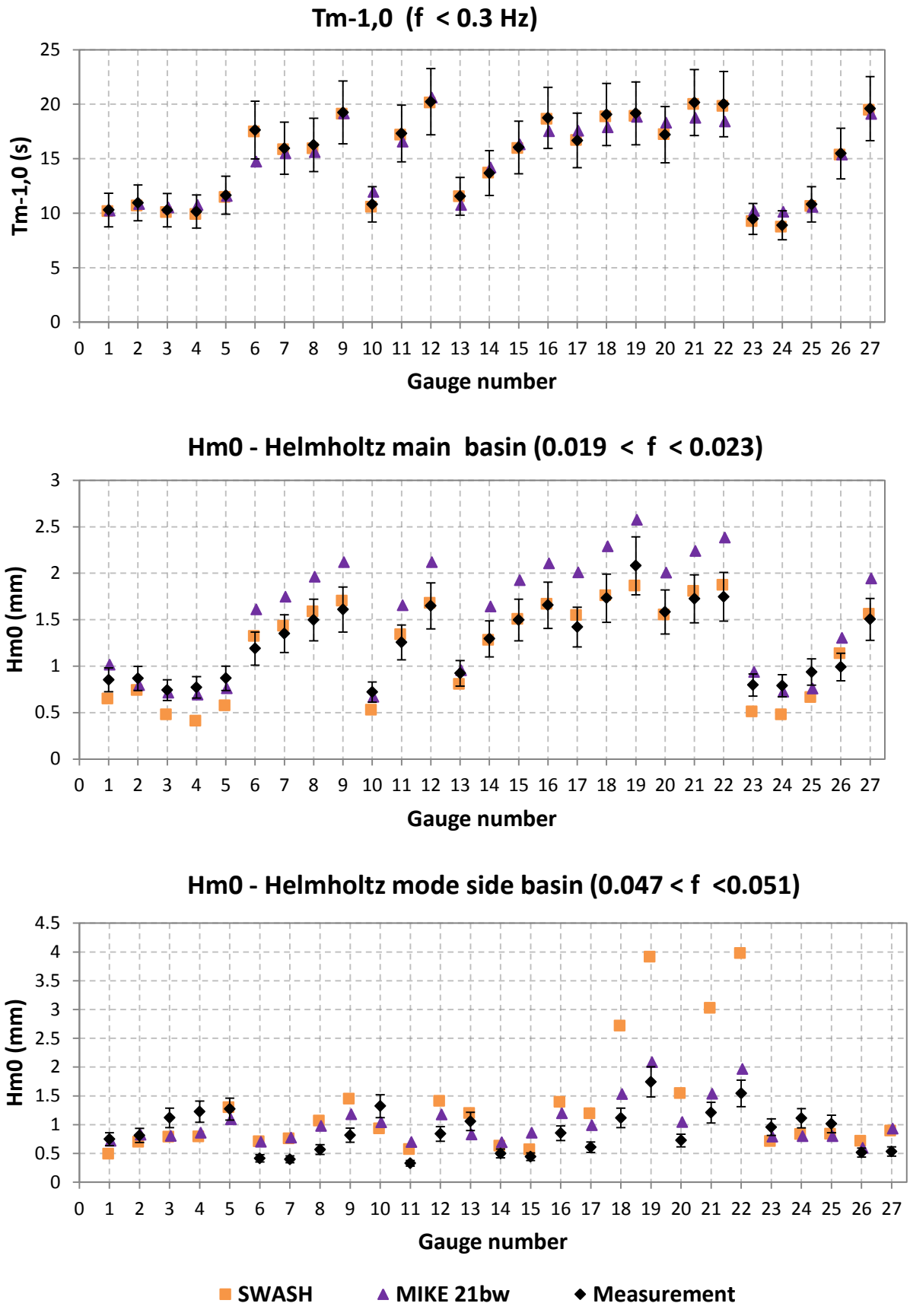

Figure C14. Comparison of the significant wave height (Hm0) and energy period (Tm-1,0) based on different frequency ranges. Note that the bars indicate a (fixed) measurement deviation of ±15%.

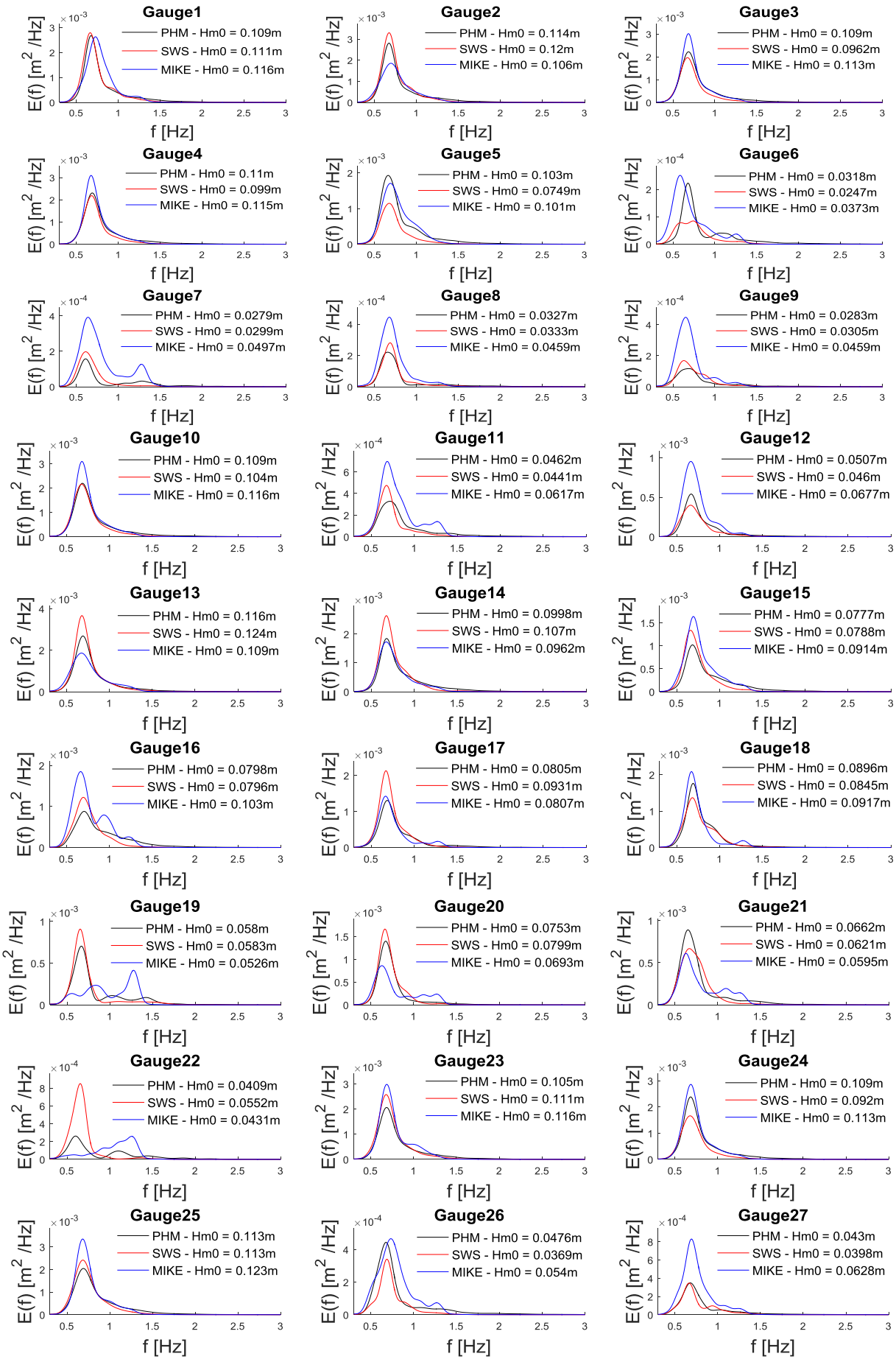

Figure C15. Frequency spectra for the primary wave energy. The provided significant wave height (Hm0) is based on frequencies larger than 0.3 Hz.

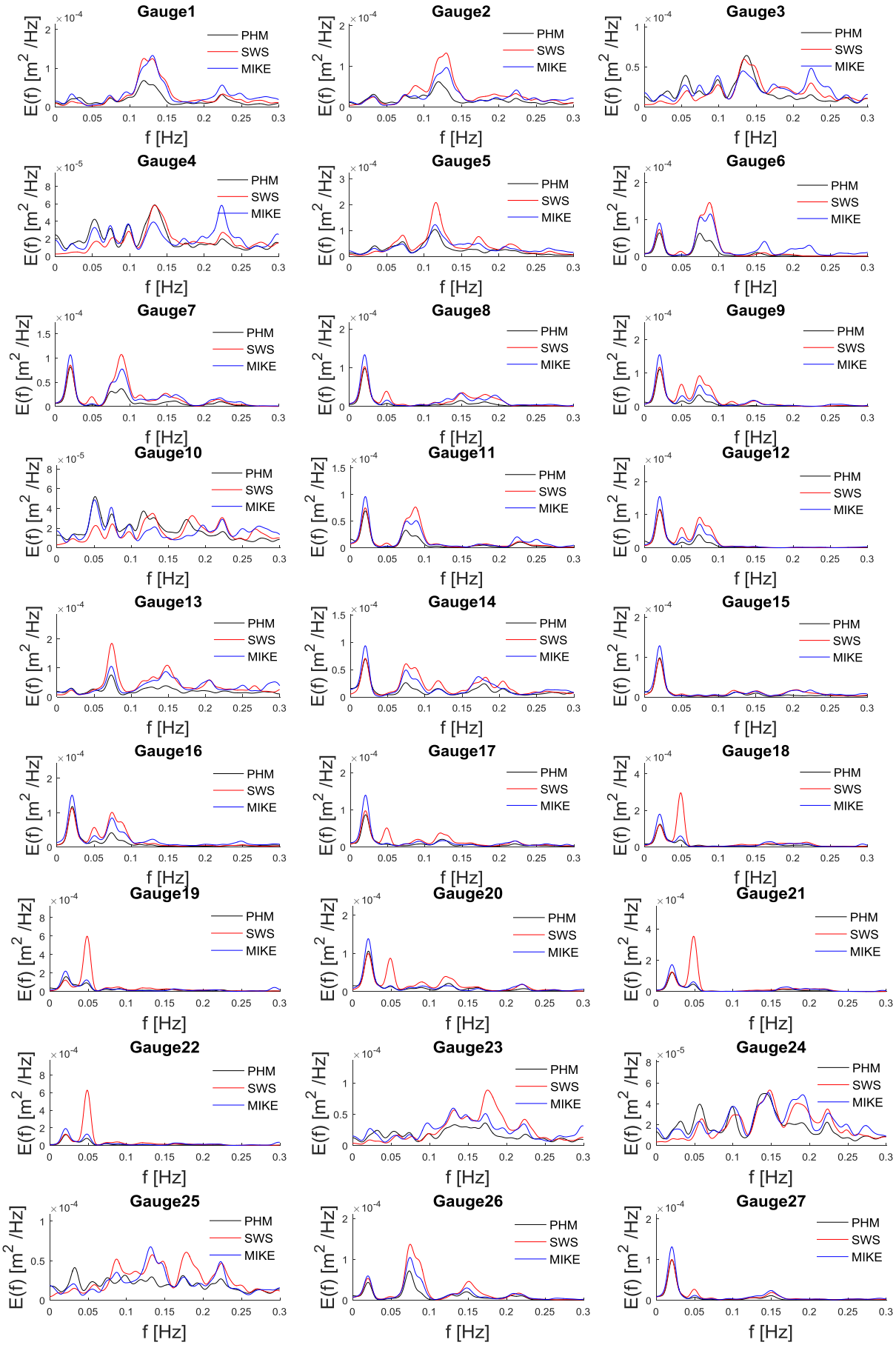

Figure C16. Frequency spectra of the low frequency energy (f < 0.3 Hz).

C6 – Results T079 prototype scale

This section presents the results of scenario T079 in prototype scale using a scale of 1:20. The spatial variation of the significant wave height is presented in Figure C17. Figures C18 and C19 present the comparison of the significant wave height and energy period based on different frequency ranges. Figures C20 and C21 present the frequency spectra at all the wave gauges for the low frequency energy (f < 0.067 Hz) and the primary wave energy (f > 0.067 Hz).

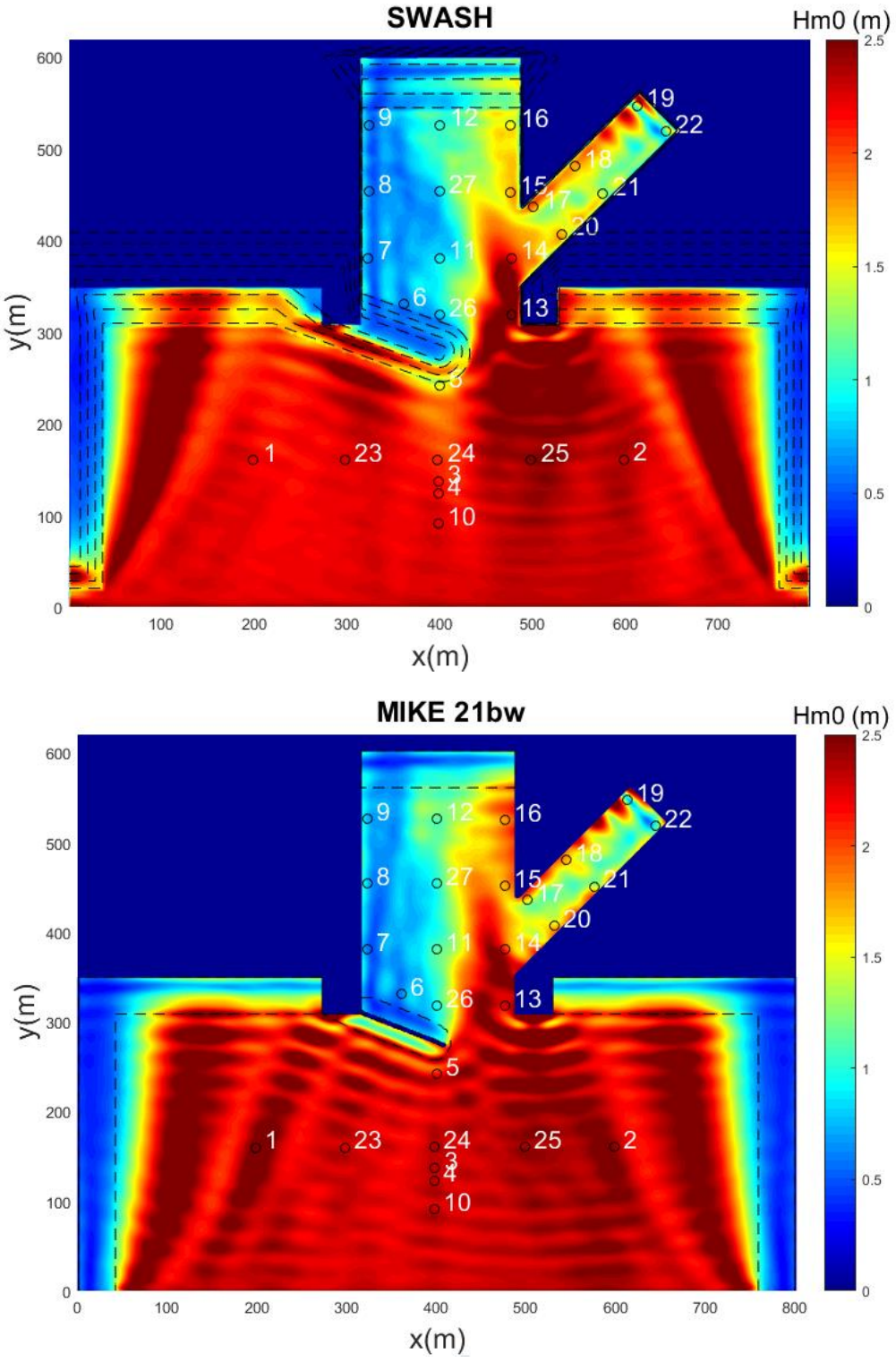

Figure C17. Spatial variation of the significant wave height (Hm0) for scenario T079 in prototype scale.

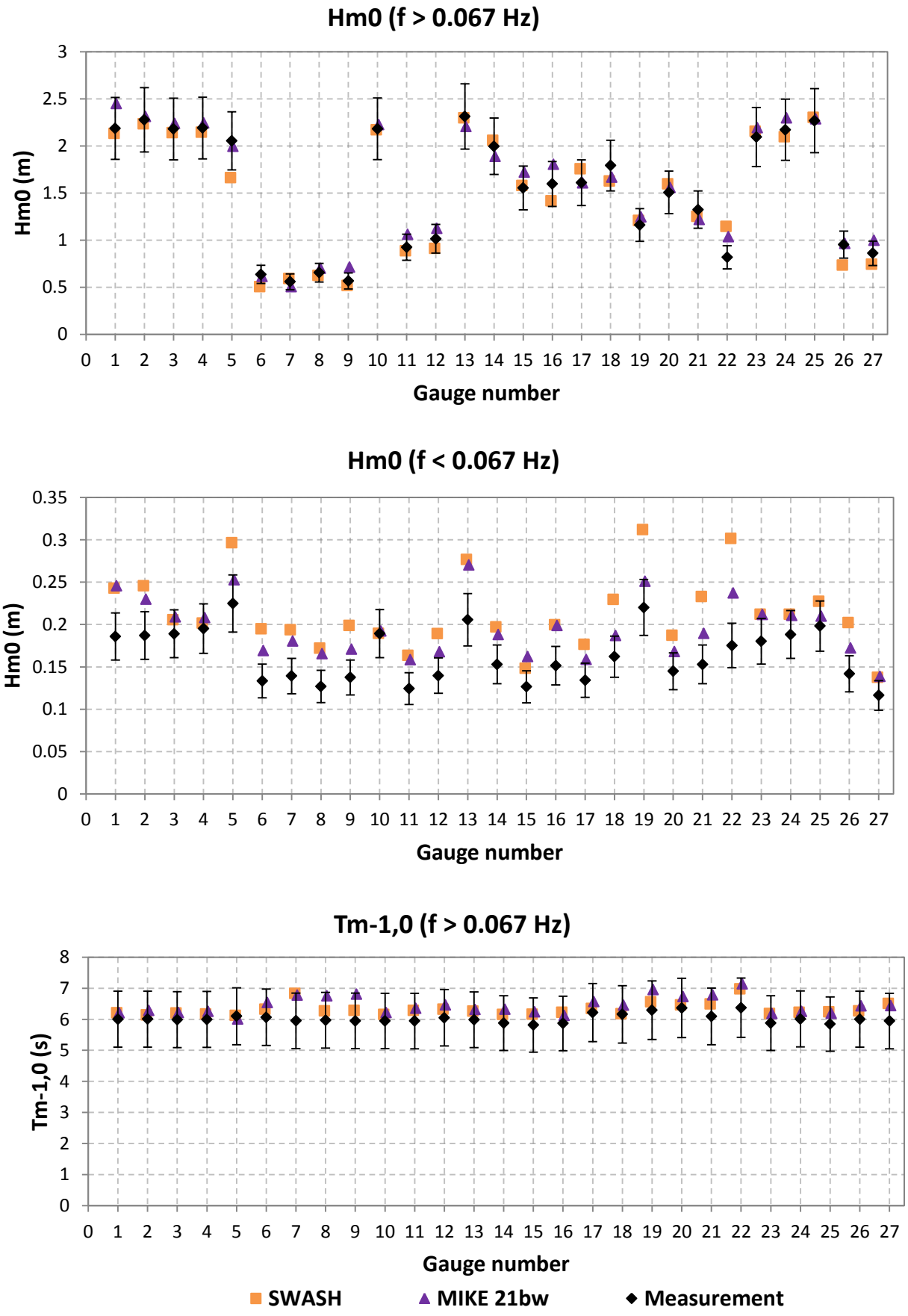

Figure C18. Comparison of significant wave height (Hm0) and energy period (Tm-1,0) based on different frequency ranges. Note that the bars indicate a (fixed) measurement deviation of ±15%.

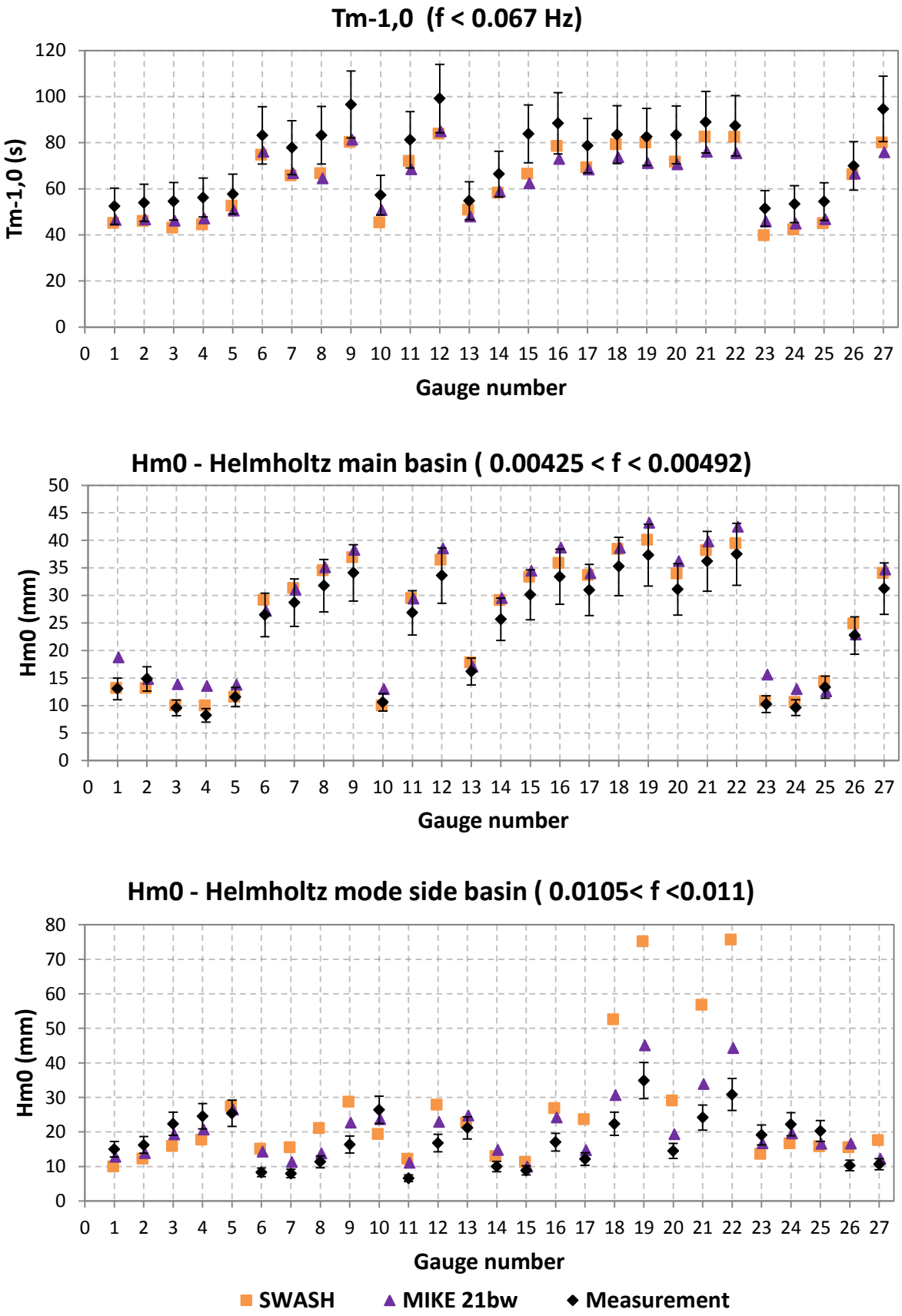

Figure C19. Comparison of significant wave height (Hm0) and energy period (Tm-1,0) based on different frequency ranges. Note that the bars indicate a (fixed) measurement deviation of ±15%.

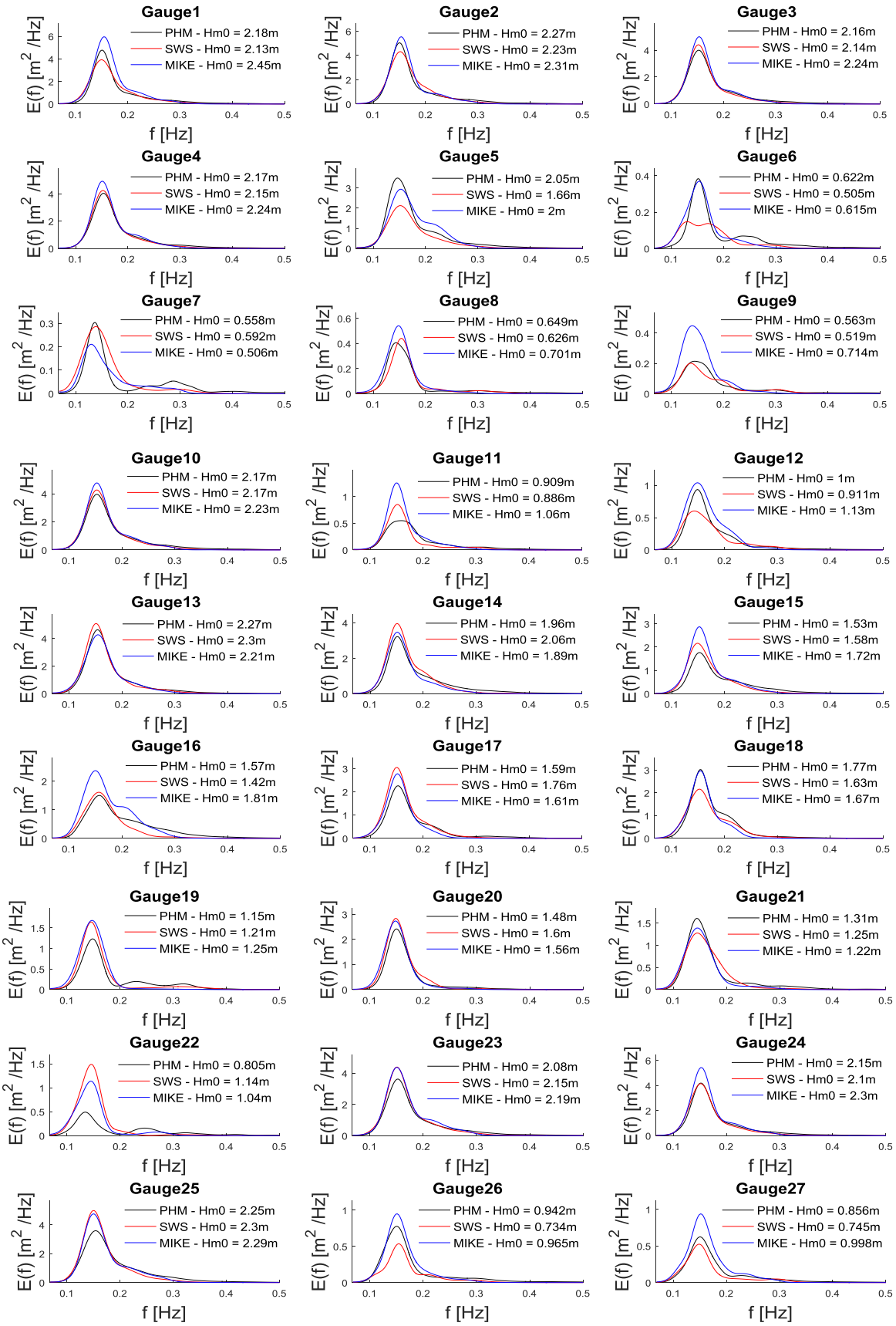

Figure C20. Frequency spectra for the primary wave energy. The significant wave height (Hm0) is based on frequencies larger than 0.067 Hz.

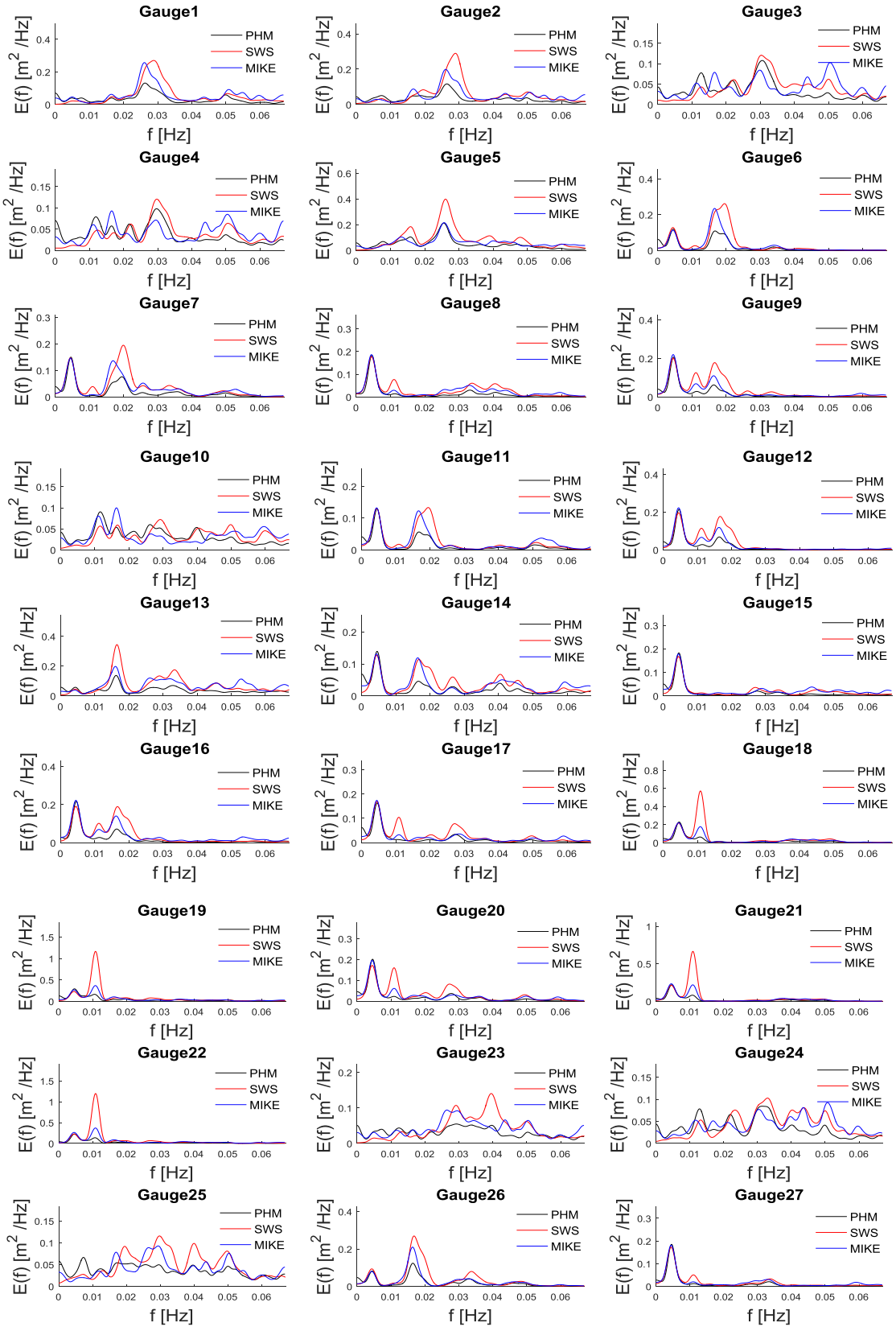

Figure C21. Frequency spectra for the low frequency energy (f < 0.067 Hz).